UNIVERSITY OF CALIFORNIA
RIVERSIDE

Nucleation and Cross-slip of Partial Dislocations in FCC Metals

A Dissertation submitted in partial satisfaction
of the requirements for the degree of

Doctor of Philosophy

in

Mechanical Engineering

by

Gang Liu

December 2009

Dissertation Committee:

Dr. Guanshui Xu, Chairperson
Dr. Javier Garay
Dr. Jianlin Liu

The Dissertation of Gang Liu is approved:

_____

_____

_____

Committee Chairperson

University of California, Riverside

Acknowledgements

I would like to gratefully and sincerely thank Dr. Xu, Guasnshui for his guidance, understanding, patience during my graduate studies at University of California, Riverside. His mentorship was paramount in providing a well rounded experience consistent my long-term career goals. I would like to thank my committee members Dr. Jinlin Liu and Dr. Javier Garay for their guidance and valuable discussions. I would also like to thank all of the members of the Dr. Xu's research group: Zijun Fang, Chengzhi Li, Gongbo Long and Wenlu Shi for their supporting and help for my research work. This is a great opportunity to express my respect to Dr. Darwin Segall for his assistance and guidance in getting start for the atomistic simulation. Thanks the financial support provided by the National Science Foundation through the CAREER (0103257) award.

I am very grateful for the friendship of all of the graduate students in the department of Mechanical Engineering at UCR. Ting Hu, Xin Xue, Bo Liu, Qiguo Jing, Hansheng Pan, etc: you guys are all my best friends.

Finally, my very special thanks to my mother Qinying Yang and my father Zhengqun Liu. I still remember the courage from my father for the science study when I was young although he has left us for 15 years.

December 2009

ABSTRACT OF THE DISSERTATION

Nucleation and Cross-slip of Partial Dislocations in FCC Metals

by

Gang Liu

Doctor of Philosophy, Graduate Program in Mechanical Engineering
University of California, Riverside, December 2009
Dr. Guanshui Xu, Chairperson

Nucleation of partial dislocations at a crack and cross-slip of partial dislocations under general loading in FCC metals are analyzed based on a multiscale model which incorporates atomic information into continuum-mechanics approach. In both analyses, the crack and the slip planes are modeled as surfaces of displacement discontinuities embedded in elastic media. The atomic potentials between the adjacent atomic layers along the slip planes are assumed to be the generalized stacking fault energies, which are obtained based on atomic calculations. The relative displacements along the slip planes, corresponding to the configurations of partial dislocations and stacking faults, are solved through the variational boundary integral method. The energetics of partial dislocation nucleation at the crack and cross-slip in FCC metals Al and Cu are comparatively studied for their distinctive difference in the intrinsic stacking fault energy.

For the analysis of nucleation of partial dislocations at a crack, several new features have emerged compared with nucleation of perfect dislocations in previous studies. Among them, the critical stress and activation energy for nucleation of partial dislocations are markedly lowered. Depending on the value of stacking fault energy and crack configuration, the saddle-point configurations of partial dislocations can be vastly

different in terms of the nucleation sequence and the size of the stacking fault. The implications of these new findings on mechanical behavior of nanostructured crystalline materials are elaborated.

For the analysis of cross-slip of partial dislocations, the conclusion from previous studies that cross-slip in FCC metals can be influenced by intrinsic stacking fault energy is confirmed. Furthermore, it is found that in Al, the preference of the gliding plane depends on the competition between the two resolved shear stresses on the slip planes. In Cu, the most preferred loading condition for cross-slip is that a lager compressing Escaig shear stress on the primary slip plane is accompanied with stretching Escaig shear stress on the cross-slip plane. The analysis of activation energy indicates that thermal motion plays an important role in cross-slip in FCC metals.

Table of Contents

List of Figures

List of Tables

Chapter 1 Introduction

1.1 Introduction to Dislocations

Dislocations in crystals are linear defects around which some of the atoms of the crystal lattice are misaligned. Fig. 1-1 shows a typical edge type dislocation which can be visualized as being caused by the termination of a plane of atoms in the middle of a crystal. The edge dislocation was proposed by Orowan, Polany, and Taylor in 1934 to explain the discrepancy between the theoretical shear stress and the experimental yield stress. In 1939 Burgers advanced the description of the screw dislocation. It was not until the 1950s, however, that the existence of dislocations was established by direct observation with experimental techniques such as electron microscopes (Dash, 1957; Schoeck and Puschl, 1991). It is well recognized that dislocations play a central role in plastic deformation in crystalline solids and are largely responsible for the internal stresses caused by plastic deformation.

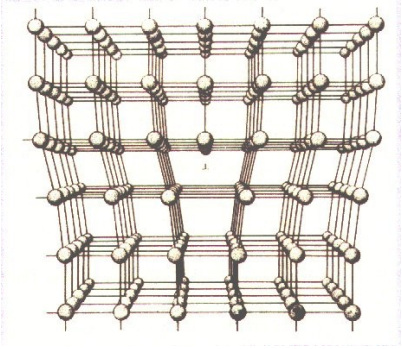

Figure 1-1. An edge dislocation in a simple cubic crystal.

In most previous analysis of dislocation nucleation problems (e.g. Xu and Argon, 2000; Xu and Zhang, 2003; Li and Xu, 2006), the dislocations are regarded as perfect dislocations. However, in FCC metals, due to the existence of the intrinsic stacking fault which is related to a closed-packed layer distortion from the stable "ABCABC" configuration to the metastable "ABC|BCA" configuration, the perfect dislocation tend to dissociate into partial dislocations with each partial connecting a perfect crystal lattice at one side and an intrinsic stacking fault at the other side. Fig. 1-2. shows the dissociation of a perfect dislocation into two Shockley partials (Heidenreich and Shockley, 1948) with relative slip vector of 1/6<112> on the {111} slip plane because the dissociated configuration reduces the elastic strain energy according to Frank criterion (Hirth and Lothe, 1982; Frank, 1949). Therefore, the partial dislocations are more common in the

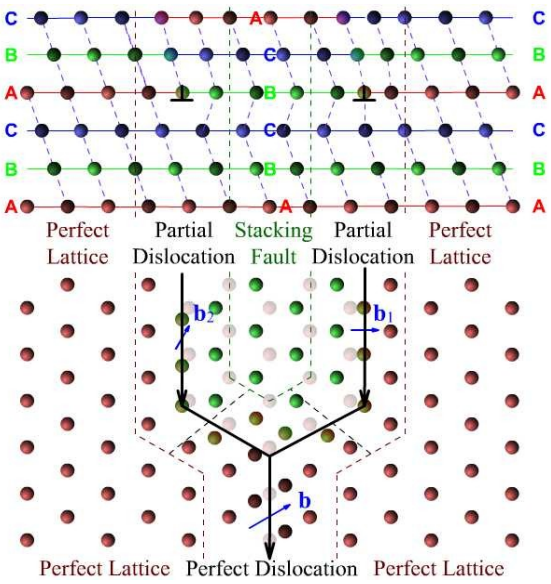

Figure 1-2. Illustration of dissociation of a perfect dislocation into Shockley partials.

FCC metals. In additional to providing the regular mechanism for plastic deformation as the perfect dislocation, the partial dislocations play special and unique roles in twinning reactions, in phase transformations, and in the formation of dislocation barriers by intersecting dislocations (Hirth and Lothe, 1982). The intrinsic stacking faults, always companied with the partial dislocations, are also important barriers to dislocation motion. For example, the fatigue properties of microcrystalline metals can be influenced by the possibility of restricted cross-slip of dissociated screw dislocations which have large intrinsic stacking fault areas (Kumar, *et al*., 2003; Feltner and Laird, 1967). Among these phenomena related to the partial dislocations, two interesting ones are selected to analyze: nucleation of partial dislocations at a crack and cross-slip of dislocations in FACC metals.

Dislocation nucleation at cracks has significant implications on brittle versus ductile behavior of crystalline materials (Rice and Thomson, 1974; Argon, 1987; Schoeck and Puschl, 1991; Rice, 1992; Rice and Beltz, 1994; Xu, *et al*., 1995, 1997; Kysar, 2003; Zhu, *et al*., 2004). When an atomically sharp crack in a perfect crystal is subjected to an increasing loading, the stress concentration at the crack tip can eventually initiate either Griffith cleavage fracture between atomic layers or dislocation nucleation induced plastic deformation. The competition between these two deformation modes plays an important role in determining whether the crystal is intrinsically ductile or brittle. In another aspect, many recent studies of nanostructured metals appear to indicate that certain mechanical behavior of nanostructured metals such as the limit strength and the strong strain rate sensitivity may be controlled by nucleation of partial dislocations at stress concentration sites on grain boundaries and their subsequent generation of stacking faults across nano-

sized grains (Asaro and Suresh, 2005). The crack configuration can be chosen to characterize stress concentration. It needs to be emphasized that the nucleation of partial dislocation has its particularity when compared to the nucleation of perfect dislocation. For the nucleation of partials, the leading partial is nucleated first and leaves an intrinsic stacking fault. The critical condition for nucleation of the trailing partial is then influenced by the stacking fault and the position of the leading partial. In either case, the energetics of dislocation nucleation at cracks is of great importance for understanding the source of dislocations and its influences on mechanical behavior of crystalline materials.

Dislocation cross-slip is as an essential mechanism in plastic deformation with implications for strain rate, dynamic recovery, hardening, and pattern formation. In FCC metals, the dislocation cross-slip is accomplished through dislocation dissociation and cross-slip of partial dislocations. The stress-strain diagram of a typical FCC metal oriented for single slip (Fig. 1-3) is a classical example of the role of cross-slip in plastic deformation (Puschl, 2002). When the critical resolved shear stress has been reached, macroscopic plastic deformation in the most favorable slip system begins. At first the motion of dislocations is nearly not obstructed, represented as the “easy glide” stage I in the stress-strain diagram. When more dislocations are nucleated, they begin to pile up at obstacles. Along with the internal stress accumulating, eventually secondary slip systems are triggered. The interaction of the primary and secondary slip systems with themselves and with one another requires larger the stress to produce additional plastic deformation. So at this stage II, hardening effects show up. Finally, internal stress levels become high enough so that the cross-slip occurs. By cross-slip, dislocations can escape from their

locked positions behind various obstacles and screw dislocations of opposite sign meet and annihilate, reducing dislocation density and relaxing internal stress. The hardening effect is therefore counteracted, and the slope of the stress–strain diagram is progressively reduced. Dynamic recovery by cross-slip is the characterization of stage III. Although cross-slip is usually thought to work as an important recovery and softening mechanism in stage III (Berner, 1960; Haasen, 1967), it has been observed to occur also in stages I and II, in which situation cross-slip can increase the dislocation density and therefore it acts as an indirect hardening mechanism. Therefore, the critical conditions for the occurrence of dislocation cross-slip are important to determine its role either as softening mechanism or hardening mechanism.

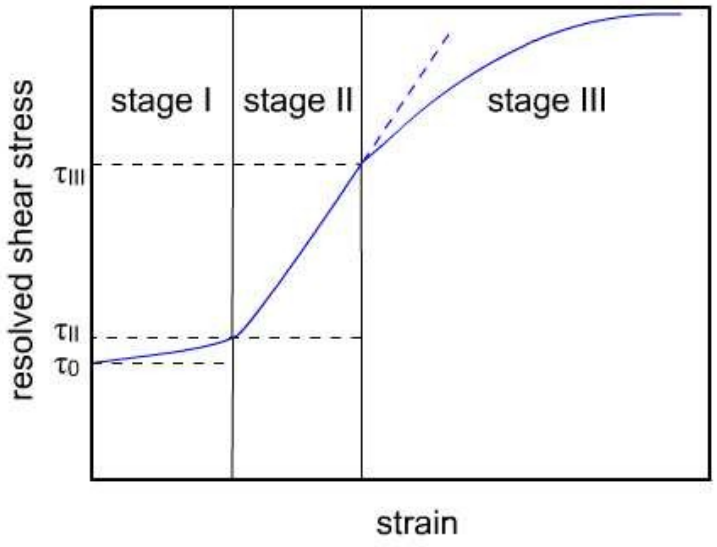

Figure 1-3. Schematic stress-strain diagram in FCC metals deformed in a tensile test oriented for single glide. Resolved shear stress is plotted as a function of strain. Stage I: easy glide; stage II: linear hardening; stage III: dynamic recovery.

1.2 Present Stage of Knowledge and Objectives

In general, two conditions are of particular interest for understanding both nucleation and cross-slip behaviors of dislocations. One is the critical stress for athermal triggering the nucleation or cross-slip, which occurs instantaneously at absolute zero temperature. The other is the activation energy required for thermally assisted nucleation or cross-slip at a stress level below the critical stress for athermal triggering. The activation energy is essential for the study because both of dislocation nucleation and cross-slip are rate-controlling processes (Bonneville, *et al*., 1988; Asaro and Suresh, 2005) and temperature can influence nucleation and cross-slip behavior. These two critical conditions can be effectively studied by the Peierls-Nabarro dislocation model (Peierls, 1941; Nabarro, 1947; Hirth and Lothe, 1982), in which a dislocation is represented as the relative displacement between two adjacent atomic layers along the slip plane and the surrounding crystals as the linear elastic continuum. Because this model allows for incorporation of atomic information into continuum mechanics based method, it has the advantage to not only treat well with the elastic singularity core which is be excluded from considerations by an internal cut-off radius r_0 in the continuum elastic model, but also incorporate the precise elastic far field and loading conditions which is difficult to be done in atomistic simulations.

The critical conditions for nucleation of perfect dislocations in various configurations, including cracks, have been extensively studied based on the Peierls-Nabarro dislocation model (e.g., Schoeck and Puschl, 1991; Rice, 1992; Rice and Beltz,

1994; Xu, *et al*., 1997; Xu and Argon, 2000; Xu and Zhang, 2003; Li and Xu, 2006). These analyses generally adopted the constrained path assumption, i.e., the slip between the adjacent atomic layers is assumed to be always constrained in the Burgers vector direction, so in these analyses the interlayer atomistic interaction can be simplified as a function of only one slip component. However, when complex configurations including the partial dislocations and stacking faults are proposed, the constrained path is not suitable anymore, because it may cause significant errors especially for a pair of curved partial dislocation configurations when significant slip involved in the configuration does not strictly follow the partial Burgers vector direction. The elimination of the constrained path assumption needs the extension of the one dimensional interlayer atomistic interaction into the generalized stacking faults energy, or so called γ-sruface (Vitek, 1968), in which general slip vector is represented by two components. Therefore, one objective of this research is to calculate the generalized stacking faults energy for various metals by atomistic simulation such as embedded atom method (Daw, 1983; 1984). The incorporation of the generalized stacking faults energy effectively removes constrained path assumption, therefore allowing for the study partial dislocation configurations.

Also using the Peierls-Nabarro model, Lu, *et al*. (2002, 2004) studied the cross-slip by assuming that the dislocation remains to be straight during the cross-slip. They found that cross-slip in FCC metals is influenced by the intrinsic stacking fault energy γ_{sf}. The critical stress and the energy barrier per unit length determined in their work is only for the loading condition that the external stresses are applied on the primary slip plane. Since the loading direction and the ratio of the shear stresses on both slip planes affect the

critical conditions the goal of our study is to determine the critical conditions for cross slip under general loading. Moreover, more realistic dislocation cross slip process involves dislocation bowing-out to take minimum energy path. The analysis of the more realistic curved dislocation cross-slip process is conducted using the fully three-dimensional boundary integral formulation (Xu and Ortiz, 1993).

Using Cu and Al as an example, our analysis is focused on delineating the influence of the intrinsic stacking fault energy on dislocation nucleation and cross-slip. The effects on the critical configurations and conditions are ascertained.

The thesis is structured as follows. In Chapter 2, the methodology based on the Peierls-Nabarro dislocation framework for both the dislocation nucleation and cross-slip is summarized, and the atomistic simulation for the generalized stacking fault energy is described in details. At the end of Chapter 2, comparison of the widths of the dissociated dislocation in Al, Ni, and Cu is made as an example of the application of the method. In Chapter 3, the energetics of partial dislocation nucleation at the crack in FCC metals Al and Cu are comparatively studied. In Chapter 4, the energetics of partial dislocation cross-slip in FCC metals Al and Cu are comparatively studied.

Chapter 2 Methodology

2.1 Introduction

Our analysis of dislocation nucleation and cross slip builds on a variational boundary integral formulation of the Peierls-Nabarro dislocation model. In this model the structure of a dislocation is modeled as the relative displacement between two adjacent atomic layers along the slip plane and the surrounding crystals as the linear elastic continuum. The continuum mechanics based boundary integral formulation, which was originally developed for the analysis of three-dimensional cracks of arbitrary geometry is solids (Xu and Ortiz 1993), allows for convenient incorporation of various types of interatomic potentials to account for the local non-linear effect. The generalized stacking fault energy, or the so called γ-surface (Vitek, 1968), obtained by atomistic simulation such as *ab initio* calculation or embedded atom method (EAM), is regarded as the best choice for its fidelity to the properties between interatomic planes. Although this method is not as direct as atomic simulation in terms of determining the nucleation or cross-slip process path, its continuum mechanics based approach possesses advantages in obtaining the stress-dependent saddle-point configurations and the associated activation energies under precisely described external loading conditions. As a complement to the atomic simulation, this method has proved to be a valuable tool in probing the activation parameters in many dislocation mechanisms (e.g., Xu and Zhang 2003; Segall, Li, Xu, 2006; Li and Xu, 2006).

2.2 Formulation of Boundary Integral Equations

Let $\mathbf{u}(\mathbf{x})$ denote displacement discontinuities along the crack and the slip planes. The total energy can be expressed by

$$\Pi[\mathbf{u}(\mathbf{x})] = W[\mathbf{u}(\mathbf{x})] + V[\mathbf{u}(\mathbf{x})] - P[\mathbf{u}(\mathbf{x})] \tag{2-1}$$

where W is the elastic strain energy caused by these displacement discontinuities, V is the interatomic layer potential energy, and P is the work of the external forces. By modeling the relative displacement discontinuities $\mathbf{u}(\mathbf{x})$ as continuous distribution of infinitesimal dislocation loops and using a known expression of interaction energy between two dislocation loops (Lothe, 1982),

$$W_{\text{int}} = \frac{1}{8\pi^2}\oint_{C_1}\oint_{C_2}\frac{1}{R}\int_0^{2\pi}\mathbf{b}_1\cdot\left[(d\mathbf{l}_1\times\mathbf{z}, d\mathbf{l}_2\times\mathbf{z}) - (d\mathbf{l}_1\times\mathbf{z}, \mathbf{z})\cdot(\mathbf{z},\mathbf{z})^{-1}\cdot(\mathbf{z}, d\mathbf{l}_2\times\mathbf{z})\right]\cdot\mathbf{b}_2 d\varphi, \tag{2-2}$$

the elastic energy for general displacement discontinuities in general anisotropic solids can be obtained (Xu 2000) as

$$W[\mathbf{u}(\mathbf{x})] = \frac{1}{16\pi^2}\int_S\int_S\frac{1}{R}\int_0^{2\pi}\mathbf{e}_i\cdot\left\{\begin{array}{l}\left[(\mathbf{n}\times\nabla u_i)_1\times\mathbf{z}, (\mathbf{n}\times\nabla u_j)_2\times\mathbf{z}\right] - \\ \left[(\mathbf{n}\times\nabla u_i)_1\times\mathbf{z}, \mathbf{z}\right]\cdot(\mathbf{z},\mathbf{z})^{-1}\cdot\left[\mathbf{z}, (\mathbf{n}\times\nabla u_j)_2\times\mathbf{z}\right]\end{array}\right\}\cdot\mathbf{e}_j d\varphi dS_1 dS_2 \tag{2-3}$$

where C_1 and C_2 represents two general dislocation loops with the Burgers vector $\mathbf{b}_1$ and $\mathbf{b}_2$ respectively; R is the distance between two points; $\mathbf{z}$ is a unit vector perpendicular to R, and φ is the angle between $\mathbf{z}$ and an arbitrary chosen reference $\mathbf{z}_0$; S represents the slip plane surface; $(,)_1$ and $(,)_2$ denote two different points on the surfaces; $\mathbf{e}_i$, i = 1, 2, 3, are Cartesian basis vectors; $\mathbf{n}$ is the normal vector on the surface S. The components of the

second-rank tensor in the notation $(\mathbf{a},\mathbf{b})$ are defined as $(\mathbf{a},\mathbf{b})_{jk} = a_i c_{ijkl} b_l$, where c_{ijkl} are elastic constants.

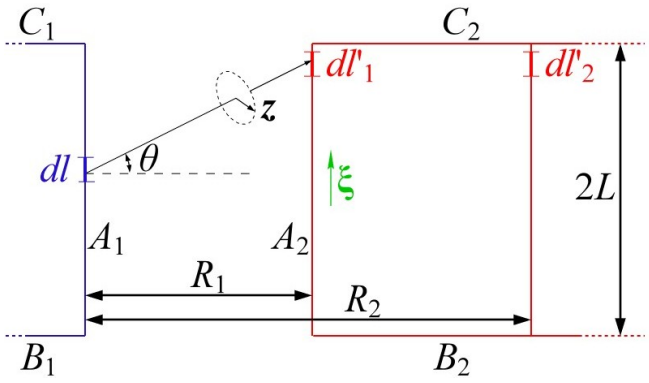

Figure 2-1. Interaction of two straight dislocation segments in coplanar dislocation loops. The interaction energy varies finitely as the distance between them changes from R_1 to R_2.

For the case that dislocations can treated as straight lines, Eq. (2-3) can be simplified from surface integral to line integral through following steps. First, the interaction energy between two parallel straight dislocations in anisotropic media is derived. As illustrated in the Fig. 2-1, a straight dislocation can be considered to be one side of a large closed rectangle loop with other three sides far away from simulation domain. For the interaction energy of two parallel straight dislocations, contained in the rectangle loops, only the two close segments (A_1-A_2) contribute appreciably to Eq. (2-2) and the other interaction terms (B_1-B_2, A_1-B_2, …), called end effects, have a negligible effect producing at most small constant terms on the interaction energy (Hirth and Lothe, 1982). Using Eq. (2-2) and only counting the interaction between A_1 and A_2, when the lengths of the segments A_1 and A_2 are both $2L$ and the distance between them is R, the interaction energy per unit length can be written as

$$\overline{W}_{\text{int}} = \frac{1}{2L}\int_{-L}^{L}\int_{-L}^{L}\frac{E(\theta)dldl'}{\sqrt{R^2+(l-l')^2}} \tag{2-4}$$

where

$$E(\theta) = \frac{1}{8\pi^2}\int_0^{2\pi}\mathbf{b}_1\cdot\left[(\boldsymbol{\xi}\times\mathbf{z},\boldsymbol{\xi}\times\mathbf{z})-(\boldsymbol{\xi}\times\mathbf{z},\mathbf{z})\cdot(\mathbf{z},\mathbf{z})^{-1}\cdot(\mathbf{z},\boldsymbol{\xi}\times\mathbf{z})\right]\cdot\mathbf{b}_2 d\varphi \tag{2-5}$$

is the energy factor as a function of only θ because $\mathbf{z}$ is dependent on θ; $\boldsymbol{\xi}$ is the common sense of two dislocation lines; and the definition of θ is shown in the Fig. 2-1. Eq. (2-4) does not converge but trends to infinity as L trends to infinity. However, the energy variation as the changing of R is finite. Considering the distance between the pair of parallel straight dislocations increasing from R_1 to R_2 as shown in the Fig. 2-1, the energy variation can be obtained from Eq. (2-4) as:

$$\begin{aligned}\Delta\overline{W} &= \overline{W}_2-\overline{W}_1 = \lim_{L\to\infty}\left[\int_{-L}^{L}\frac{E(\theta_2)}{\sqrt{R_2^2+l'^2_2}}dl'_2-\int_{-L}^{L}\frac{E(\theta_1)}{\sqrt{R_1^2+l'^2_1}}dl'_1\right]\\ &= -2\lim_{L\to\infty}\left[\int_{L/R_2}^{L/R_1}\frac{E(\bar{l})}{\sqrt{1+\bar{l}^2}}d\bar{l}\right] = -2\lim_{L\to\infty}\left[E(\bar{l}_\zeta)\ln\frac{R_2\sqrt{(R_1/L)^2+1^2}+R_2}{R_1\sqrt{(R_2/L)^2+1^2}+R_1}\right]\\ &= -2E_0\ln\frac{R_2}{R_1}\end{aligned} \tag{2-6}$$

where $\bar{l}=l'/R=\tan\theta$ and $\bar{l}_\zeta$ is an existing number in the interval $[L/R_2, L/R_1]$ according to the mean value theorem of integrals. As L trends to infinity, $\bar{l}_\zeta$ trends to infinity and the angle θ trends to $\pi/2$. Thus the energy factor becomes $E_0 = E(\pi/2) = \frac{1}{4\pi}\mathbf{b}_1\cdot\mathbf{B}\cdot\mathbf{b}_2$ where

$$\mathbf{B} = \frac{1}{2\pi}\int_0^{2\pi}\left[(\boldsymbol{\xi}\times\mathbf{z},\boldsymbol{\xi}\times\mathbf{z})-(\boldsymbol{\xi}\times\mathbf{z},\mathbf{z})\cdot(\mathbf{z},\mathbf{z})^{-1}\cdot(\mathbf{z},\boldsymbol{\xi}\times\mathbf{z})\right]d\varphi. \tag{2-7}$$

In Eq. (2-7), **z** is constrained in the plane perpendicular to the dislocation sense vector **ξ**. Here **B** is a positive-definite symmetric matrix that depends only on the direction of the dislocation sense **ξ**. Note that the matrix **B** is coincident as in the energy per unit length of a single straight dislocation $\overline{W} = \frac{1}{4\pi}\mathbf{b}\cdot\mathbf{B}\cdot\mathbf{b}\ln(R/R_a)$ and for isotropic solids, **B** takes the diagonal form $B_{11} = B_{22} = \mu/(1-\nu)$, $B_{33} = \mu$. By selecting the energy original point at a distance of r_0 between the pair of parallel dislocations, when the distance between them is R, the interaction energy per unit length can be expressed as

$$\overline{W}_{\text{int}} = \frac{1}{2\pi}\mathbf{b}_1\cdot\mathbf{B}\cdot\mathbf{b}_2\ln(r_0/R). \tag{2-8}$$

Second, following the same approach to obtain the integral equation method for an arbitrary three-dimensional crack in an anisotropic elastic media, the elastic strain energy of the solid with two dimensional penetrating cracks can be expressed from Eq. (2-8). As illustrated in Fig. 2-2, let L represent the two-dimensional crack which penetrates the solid media along the perpendicular direction (**ξ**). It can be divided into n segments, each of which can be regarded as a straight dislocation (straight line in Fig. 2-2) with the sense

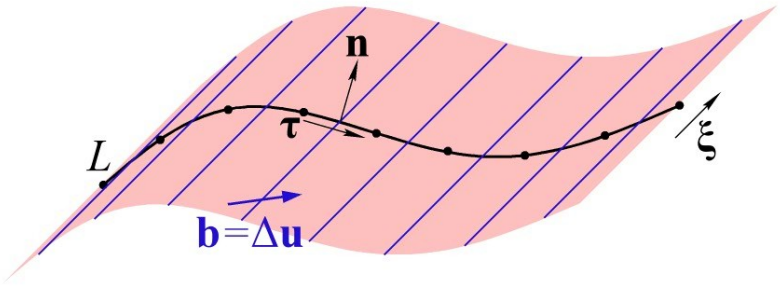

Figure 2-2. Discretization of a penetrating 2D crack.

along $\boldsymbol{\xi}$ direction. The Burgers vector of each straight dislocation equals to the differential of the displacement discontinuities at the end points of each segment as:

$$\mathbf{b} = \Delta\mathbf{u} = \frac{\Delta u_i}{\Delta L}\Delta L\mathbf{e}_i \tag{2-9}$$

where ΔL is the length of each segment and $\mathbf{e}_i$ is the Cartesian basis. Invoking the principle of superposition and using the Eq. (2-8), the elastic strain energy per unit length of the cracked solid follows as

$$\overline{W}\left[\mathbf{u}(\mathbf{x})\right] = \frac{1}{2}\sum_{K_i=1}^{n}\sum_{K_j=1}^{n}\left[\frac{1}{2\pi}\mathbf{b}_{K_i}\cdot\mathbf{B}\cdot\mathbf{b}_{K_j}\ln\left(r_0/R\right)\right] = \frac{1}{4\pi}\sum_{K_i=1}^{n}\sum_{K_j=1}^{n}\left[\left(b_i\right)_{K_i}B_{ij}\left(b_j\right)_{K_j}\ln\left(r_0/R\right)\right] \tag{2-10}$$

The factor 1/2 in Eq. (2-10) compensates for the fact that the double sum accounts for the interaction energy between each pair of straight dislocations twice. The computation of the elastic strain energy is complete by passing to the limit of $\Delta L \to 0$. To this end, the Burgers vector in Eq. (2-9) becomes $b_i = \left(\partial u_i/\partial L\right)dL = \left(\nabla u_i\cdot\boldsymbol{\tau}\right)dL$ where $\boldsymbol{\tau}$ is the tangent direction along L satisfying $\boldsymbol{\tau} = \boldsymbol{\xi}\times\mathbf{n}$ and $\mathbf{n}$ is unit normal vector to the crack surface. Finally, for the two dimensional case, the Eq. (2-3) can be simplified to

$$\overline{W}\left[\mathbf{u}(\mathbf{x})\right] = \frac{1}{4\pi}\int_L\int_L\left(\nabla u_i\cdot\boldsymbol{\tau}\right)_1 B_{ij}\left(\nabla u_j\cdot\boldsymbol{\tau}\right)_2\ln\left(r_0/R\right)dL_1dL_2 \tag{2-11}$$

where $\overline{W}$ now represents elastic energy per unit length; $(,)_1$ and $(,)_2$ denote two different points on L; R is the distance between two points; $\boldsymbol{\tau}$ is the tangent direction along L; r_0 is the reference radius, the section of which has no influence on the variation of the energy; B_{ij} is the energy factor matrix defined in Eq. (2-7). The use of Eq. (2-11) over (2-3) reduces the surface integration to the line integration, which improves not only the efficiency but also the accuracy of the integration. Note that the singular integral kernels

of the type $1/R$ can be accurately treated following the approach given by Xu and Ortiz (1993).

The work of the external force $P[\mathbf{u}(\mathbf{x})]$ in Eq. (2-1) is defined as

$$P[\mathbf{u}(\mathbf{x})] = \int_S \boldsymbol{\sigma} \cdot \mathbf{u}(\mathbf{x}) dS \tag{2-12}$$

where $\boldsymbol{\sigma}$ is the surface traction, which can be related to the remote stress by invoking the principle of superposition.

The interatomic layer potential energy $V[\mathbf{u}(\mathbf{x})]$ in Eq. (2-1) is given by

$$V[\mathbf{u}(\mathbf{x})] = \int_S \Phi[\mathbf{u}(\mathbf{x})] dS \tag{2-13}$$

where $\Phi[\mathbf{u}(\mathbf{x})]$ is the interatomic layer potential energy per unit area, which may be defined as the energy variation as two blocks of crystals move uniformly against each other. Ignoring the coupling effect of normal stress across the atomic plane, this energy variation, termed the generalized stacking fault energy or the so called γ-surface (Vitek, 1968), can be reliably obtained from various atomistic calculations. The details about the energy $\Phi[\mathbf{u}(\mathbf{x})]$ are described in the next section 2.3.

The displacements are discretized through the standard finite elements. The resulting nonlinear equations are solved by Newton-Raphson iterations. The possible saddle-point configurations of dislocations are solved by recourse to displacement control through Lagrange multiplier method. The details of these numerical treatments are referred to Xu and Ortiz (1993) and Xu, *et al* (1995).

2.3 Generalized Stacking Fault Energy (γ-surface)

The energy $\Phi[\mathbf{u}(\mathbf{x})]$ in Eq. (2-13), resulting from the interaction of the atoms on the adjacent layers along the slip plane, is expressed as a 1D sinusoid function in the original Peierls-Nabarro Model. In 2D this energy can be termed as the generalized stacking fault energy or the so called γ-surface (Vitek, 1968), without taking into account of the coupling effect of normal stress across the atomic plane. Consider a perfect crystal which is cut along a plane (Fig. 2-3). The two half crystals are displaced against each other and then reconnected, resulting in a uniform relative slip displacement **u** across cut plane. The generalized stacking fault energy is defined as the energy variation per unit area due to this relative slip.

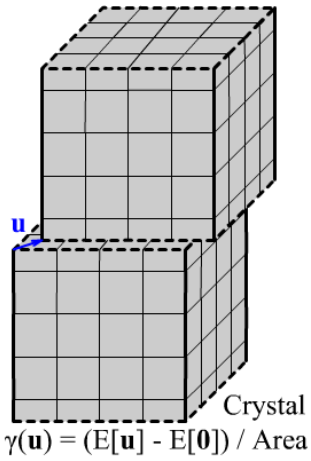

Figure 2-3. Two half crystal blocks have a relative displacement **u** across cut plane which results in an energy increment defined as generalized staking fault energy (γ-surface).

The generalized stacking fault energy can be obtained by atomic calculations based on the embedded atom method (EAM) or first-principles density function theory method

(DFT).To this end, we set up a uniform slip configuration (Segall, 2006) of crystal blocks represented by certain supercells with the lattice vectors of $\mathbf{R}_1$ as the Burgers vector and $\mathbf{R}_3$ as the normal vector of the slip planes. For example, FCC metals have the favorable {111} slip planes so that the lattice vectors of the suppercells are

$$\mathbf{R}_1 = \mathbf{a}_x = \frac{1}{2}[1\,\bar{1}\,0]a_0 = \mathbf{b},\ \mathbf{R}_2 = \mathbf{a}_y = \frac{1}{2}[11\bar{2}]a_0,\ \ \mathbf{R}_3 = 4[111]a_0 \tag{2-14}$$

The supercells contain 8-12 layers atoms on the slip plane and are applied periodic boundary condition along all three lattice vectors direction. The uniform slip configuration with a slip vector **u** ([u_x, u_y]) is achieved by modifying the lattice vector $\mathbf{R}_3$ to $\left(R_{3x} + u_x R_1, R_{3y} + u_y R_2, R_{3z}\right)$ while keeping the atoms' absolute positions (not lattice coordinates) in the suppercell (Fig. 2-4). For every step corresponding to the slip vector **u**,

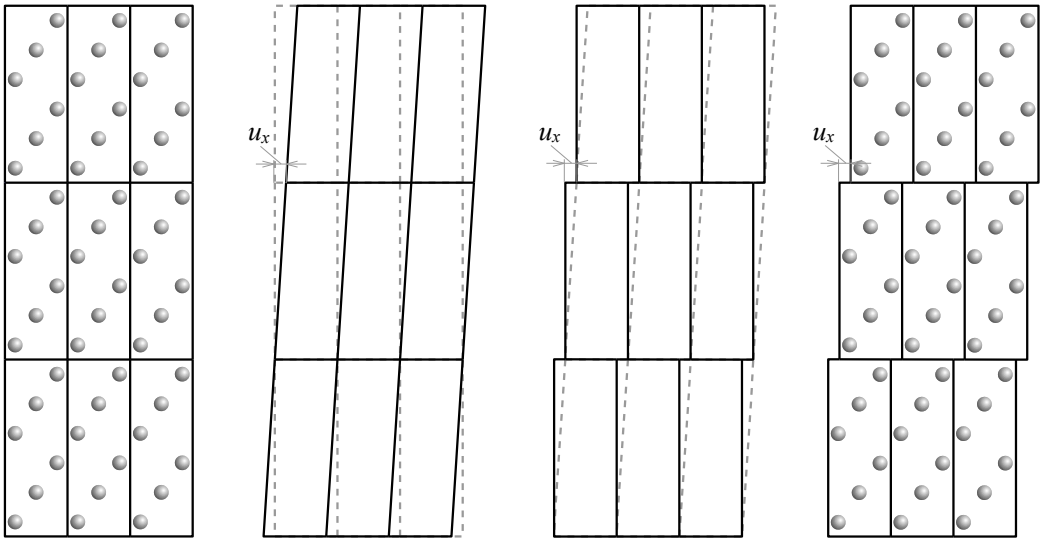

Figure 2-4. Simulate a uniform slip by [u_x, u_y] of crystal blocks by lattice vector transformation **($\mathbf{R}_3 \rightarrow [\,R_{3x} + u_x R_1, R_{3y} + u_y R_2, R_{3z}\,]$).**

the atoms in the supercells are relaxed along the direction perpendicular to the slip plane while not relaxing lattice vectors under dilation to obtain a relaxed total energy. The generalized stacking fault energy due to the slip vector **u** is just the variation of the total energy per unit area as

$$\gamma[\mathbf{u}] = \frac{E_{\text{tot}}[\mathbf{u}] - E_{\text{tot}}[\mathbf{0}]}{A} \tag{2-15}$$

where A is the area of the cell surface parallel to the slip plane and E_{tot} means the total potentials all of the atoms in one supercell.

Both embedded atom method and first principles density function theory have been used to obtain the potentials between the atomic layers. We select embedded atom method for its computational simplicity. The semi-empirical embedded atom method is currently the method of choice for doing calculations in close-packed metals; it combines the computational simplicity needed for larger systems with a physical picture that includes many-atom effects and avoids some of the problems of the pair-potential scheme (Daw, 1983; Daw, 1984). In the embedded atom method, by viewing each atom as embed in a host electron gas created by its neighboring atoms, the total energy of the system of atoms can be represented as

$$E_{\text{tot}} = \frac{1}{2}\sum_{i,j}\phi(r_{ij}) + \sum_{i}F(\bar{\rho}_i) \tag{2-16}$$

where $\phi(r_{ij})$ is the pair potential as a function of the distance r_{ij} between atoms i and j, and F is the "embedding energy" as a function of the host "density" $\bar{\rho}_i$ induced at site of

the atom *i* by all other atoms in the system. The embedding energy can be viewed as the interaction of the atom in the background electron gas. The host density $\overline{\rho}_i$ is given by

$$\overline{\rho}_i = \sum_{j \neq i} \rho\left(r_{ij}\right) \tag{2-17}$$

where $\rho(r_{ij})$ is the "atomic density" function resulting from adjacent atom electron gas. These potentials are expressed in terms of parameterized functions, with the values of the parameters being defined through a fitting procedure based on the requirement that the potential reproduces a given set of experimentally known properties. The implementations of the EAM potential can be various in the choice of the functional forms and in the physical interpretation of the quantities. Basically, the equilibrium parameter a_0, the cohesive energy E_0, the vacancy formation energy E_v^f, and the elastic moduli (C_{11}, C_{12}, and C_{44}) are used as the fitting properties.

A very simple empirical "N-body" potential form for seven BCC transition metals was proposed by Finnis and Sinclair (1984) as

$$\phi(r) = \begin{cases} (r-c)^2\left(c_0 + c_1 r + c_2 r^2\right) & r < c \\ 0 & r \geq c \end{cases}, \tag{2-18}$$

$$F(\rho) = -A\sqrt{\rho}\,, \tag{2-19}$$

$$\rho(r) = \begin{cases} (r-d)^2 + \dfrac{\beta(r-d)^3}{d} & r < d \\ 0 & r \geq d \end{cases} \tag{2-20}$$

where the parameters c_0, c_1, c_2, c, A and d were fitting by certain experimental physical values a_0, E_0, C_{11}, C_{12}, C_{14}, and E_v^f ; the parameter β was chosen to introduce a maximum in ρ within the first-neighbor distance and could be a plausible arbitrary value.

Chantasiriwan and Milstein (1998) proposed a parameterization scheme with other more physical experimental properties such as higher order elastic moduli (C_{111}, C_{112}, C_{123}, C_{144}, C_{166}, and C_{456}). In their potential formula for 12 cubic metals (Ag, Al, Au, Cu, Fe, K, Li, Mo, Na, Nb, Ni, and Rb):

$$\phi(r)=\begin{cases} A(r-r_m)^2\left(1+\sum_{i=1}^{6} d_i r^i\right) & r<r_m \\ 0 & r\geq r_m \end{cases}, \tag{2-21}$$

$$\rho(r)=\frac{1+b_1\cos(\alpha r)+b_2\sin(\beta r)}{r^{\beta}} \tag{2-22}$$

the parameters A and d_i are determined from empirical values of the atomic volume V_0 at zero pressure, the unrelaxed vacancy formation energy E_v^f , and the combinations of elastic moduli $C_{11} - C_{12}$, C_{44}, $C_{111} - 3C_{112} + 2C_{123}$, $C_{144} - C_{166}$, and C_{456}; b_1 and b_2 are fitting parameters that are chosen to satisfy the expressions for the elastic-moduli ratios $(C_{12} - C_{44}) / (C_{144} - C_{456})$ and $(C_{12} - C_{44}) / (2C_{144} + C_{112} - C_{166} - C_{123} - C_{456})$. As to the embedding function $F(\rho)$, it was determined by the Rose's universal equation of status (Rose, 1984) following the suggestion of Foiles, *et al*. (1986) as

$$F(\rho)=E_{EOS}(a^*)-\frac{1}{2}\sum_{i,j}\phi(r_{ij}). \tag{2-23}$$

For a cubic crystal with the lattice parameter a, the Rose's equation of status (EOS) is

$$E_{\mathrm{EOS}}(a^*) = -E_{\mathrm{coh}}\left(1 + a^* + ka^{*3}\right)e^{-a^*} \tag{2-24}$$

with $a^* = (a - a_0)/a_0\lambda$ and $\lambda = \sqrt{E_{\mathrm{coh}}/9V_0\kappa}$. The constants a_0, E_{coh}, V_0, and κ are the lattice parameter, magnitude of cohesive energy, volume per atom, and bulk modulus, respectively, at the unstressed reference state.

Table 2-1. The physical constants used for CM EAM model construction

	Al	Ni	Cu	Fe	Mo	Li	Au
a_0 (Å)	4.03	3.52	3.60	2.87	3.15	3.49	4.09
C_{11} (Mbar)	1.143	2.508	1.762	2.26	4.696	0.148	1.929
C_{12} (Mbar)	0.6192	1.500	1.2494	1.40	1.676	0.125	1.638
C_{44} (Mbar)	0.3162	1.235	0.8177	1.16	1.068	0.108	0.415

In order to improve the accuracy and reliability, the development of a potential form can also be based on the data of both experimental results and a large set of energies generated by *ab initio* calculations. Mishin and Mehl *etc.* (1999) proposed the potential functions for Al and Ni in terms of cubic splines through given sets of $\{r_i, \phi_i\}$, $\{r_i, \rho_i\}$, and $\{\rho_i, F_i\}$ points. The cubic splines coefficient sets are fitting to equilibrium lattice parameter a_0, the cohesive energy E_0, bulk modulus κ, the elastic moduli C_{11}, and C_{12}; phonon frequencies at the zone edge point X; unrelaxed values of the vacancy formation energy E_v^f, the vacancy migration energy E_v^m, the intrinsic stacking fault energy γ_{sf}, the surface energy $\gamma_s(100)$, $\gamma_s(110)$, and $\gamma_s(111)$; an empirical EOS for any given set of lattice parameters; and the *ab initio* energies of several alternative structures (HCP, BCC and diamond structure) with the same first-neighbor distance as that in the equilibrium FCC phase (R_0). For the metal Cu, the potential functions are in the form of formula with the

similar parameterization process based on the same data set of the experimental values and the *ab initio* energies as (Y. Mishion, 2001)

$$\begin{aligned}\phi(r) = &\left[E_1 M\left(r, r_0^{(1)}, \alpha_1\right) + E_2 M\left(r, r_0^{(2)}, \alpha_2\right) + \delta\right]\psi\left(\frac{r - r_c}{h}\right) \\ &- \sum_{n=1}^{3} H\left(r_s^{(n)} - r\right) S_n \left(r_s^{(n)} - r\right)^4\end{aligned} \tag{2-25}$$

where

$$M(r, r_0, \alpha) = \exp\left[-2\alpha(r - r_0)\right] - 2\exp\left[-\alpha(r - r_0)\right] \tag{2-26}$$

is a Morse function, H(x) is a unit step function, $\psi(x)$ is defined as

$$\psi(x) = \begin{cases} 0 & x \geq 0 \\ \dfrac{x^4}{1 + x^4} & x < 0 \end{cases}, \tag{2-27}$$

$$\rho(r) = \left[a\exp\left(-\beta_1\left(r - r_0^{(3)}\right)^2\right) + \exp\left(-\beta_2\left(r - r_0^{(4)}\right)\right)\right]\psi\left(\frac{r - r_c}{h}\right), \tag{2-28}$$

$$F(\bar{\rho}) = \begin{cases} F^{(0)} + \dfrac{1}{2}F^{(2)}(\bar{\rho} - 1)^2 + \sum_{n=1}^{4} q_n (\bar{\rho} - 1)^{n+2} & \bar{\rho} < 1 \\ \dfrac{F^{(0)} + \frac{1}{2}F^{(2)}(\bar{\rho} - 1)^2 + q_1(\bar{\rho} - 1)^3 + Q_1(\bar{\rho} - 1)^4}{1 + Q_2(\bar{\rho} - 1)^3} & \bar{\rho} \geq 1 \end{cases}. \tag{2-29}$$

The intrinsic stacking fault energy γ_{sf} used in the fitting process is actually one special point on the generalized stacking fault energy surface corresponding to a stacking fault structure ABC|BCABC for FCC metals. These potential functions from the work of Mishion *etc.* (1999; 2001) are selected in the γ-surface calculation for the metals Cu, Ni, and Al since the functional parameters already include certain γ-surface information and has better coherence to the experiment results on intrinsic stacking fault energy than the

Chantasiriwan-Milstein potential (CM). Due to the lack of better formula for other metals (Fe, Mo, *etc.*), the CM potentials are chosen for qualitative study.

Table 2-2. The physical constants used for MI EAM model construction

	Al	Ni	Cu
a_0 (Å)	4.05	3.52	3.615
C_{11} (Mbar)	1.14	2.47	1.699
C_{12} (Mbar)	0.616	1.48	1.226
C_{44} (Mbar)	0.316	1.25	0.762

Following the approach described above, the values of stacking fault energies corresponding to 1000 various slip vectors [u_x, u_y] have been obtained and the contour plots of the γ-surfaces on the slip plane for several metals are shown in Fig. 2-5. The γ-surfaces for the FCC metals Al, Ni and Cu have the similar style in Fig. 2-5 due to their

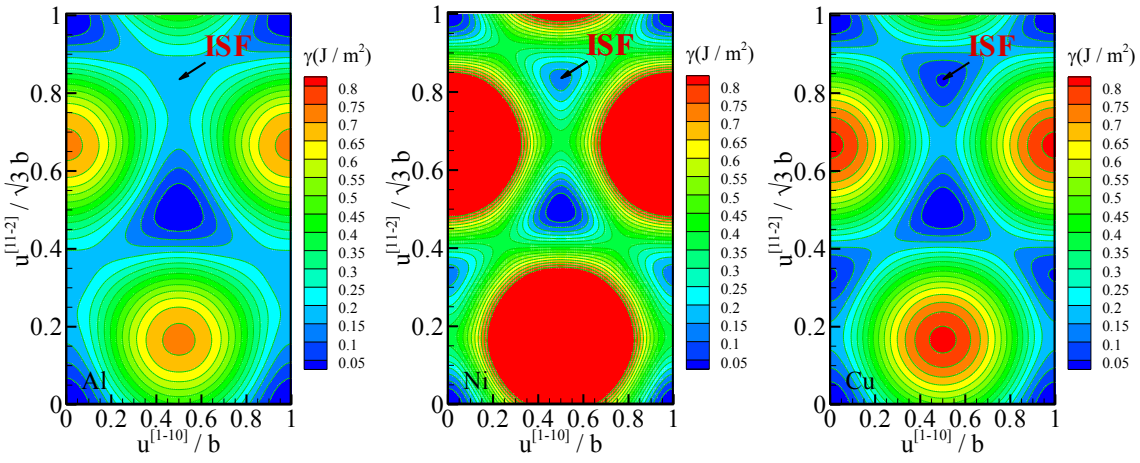

(1) (2) (3)

Figure 2-5. Contour plot of the γ-surfaces for FCC metals: (1) Al, (2) Ni and (3) Cu.

same lattice type. However one significant discrepancy among these metals is their various second lowest energies or the intrinsic stacking fault energy γ_{SF} (marked as ISF in Fig. 2-5) corresponding to the intrinsic stacking fault configuration which can be formed by a uniform slip of the upper crystal block with the slip vector $\mathbf{u} = 1/2\mathbf{R}_1 - 1/6\mathbf{R}_2$ or $\mathbf{u} = 1/3\mathbf{R}_2$, resulting in the stacking sequences as ABC|BCABC. Thus it gives the intrinsic stacking fault energy on the generalized stacking fault energy surface as $\gamma_{sf} = \gamma[R_1 / 2, -R_2 / 6] = \gamma[0, R_2 / 3]$. It must be realized that the intrinsic stalking fault energies for these three metals are distinguished from each other a lot which gives metals various properties by affecting the width of the intrinsic stacking fault area when a full dislocation dissociates. The various intrinsic stacking fault energies γ_{sf} obtained from EAM for the typical FCC metals Al, Ni, and Cu are summarized in Table 2-3 with comparison with the experimental values. We also listed the energy γ_{sf} calculated from CM potential in Table 2-3 as another comparison. The values obtained from Mishion potentials are in good agreement with the experiment measurements listed in the reference. And for metal Cu, CM potential gives a wrong negative γ_{sf}; thus it should be noted that the CM potentials tend not to be suited for the study of plasticity in some FCC metals, since they would fail in the description of the dislocation structure.

Table 2-3. Intrinsic stacking fault energy γ_{sf} (mJ/m^2) for FCC metals Al, Ni and Cu

	Al	Ni	Cu
EAM (Mishion *etc.*)	156.2	127.0	44.45
EAM (Chantasiriwan *etc.*)	90	9	-5
Experiment	166	125	45

Taking into account of the symmetry of the crystal slip plane, the γ-surface can be expressed in the Fourier expansion (Schoeck, 1999; 2001) corresponding to reciprocal lattice vectors, i.e.,

$$\gamma[\mathbf{u}] = \sum_{m,n=-\infty}^{+\infty} C_{mn} e^{i\mathbf{u}\cdot(m\mathbf{G}_1 + n\mathbf{G}_2)} \tag{2-30}$$

where $\mathbf{G}_1$ and $\mathbf{G}_2$ are the reciprocal vectors defined by $\mathbf{G}_i \cdot \mathbf{R}_j = 2\pi\delta_{ij}$; m, n are integers. Let $\mathbf{u} = \bar{u}_x \mathbf{R}_1 + \bar{u}_y \mathbf{R}_2$, where $\bar{u}_x$ and $\bar{u}_y$ are normalized relative displacements, the Fourier expansion of the γ-surface becomes

$$\gamma(\bar{u}_x, \bar{u}_y) = \sum_{m,n=-\infty}^{+\infty} C_{mn} e^{2i\pi(m\bar{u}_x + n\bar{u}_y)} \tag{2-31}$$

where the Fourier expansion coefficients can be determined by the integral

$$C_{mn} = \int_0^1 \int_0^1 \gamma(\bar{u}_x, \bar{u}_y) e^{-2i\pi(m\bar{u}_x + n\bar{u}_y)} d\bar{u}_x d\bar{u}_y \tag{2-32}$$

from which C_{mn} can be calculated from the numerical integral based on the sample values of $\gamma(\bar{u}_x, \bar{u}_y)$ obtained from atomic calculations such as embedded atom method (EAM) or density functional method. Considering $\gamma(\bar{u}_x, \bar{u}_y)$ is an even function to $\bar{u}_x$, an equivalent Fourier expansion of γ-surface in terms of triangle functions is

$$\gamma(\bar{u}_x, \bar{u}_y) = \sum_{m,n=0}^{+\infty} \cos 2m\pi\bar{u}_x \left(a_{mn} \cos 2n\pi\bar{u}_y + b_{mn} \sin 2n\pi\bar{u}_y\right). \tag{2-33}$$

These coefficients a_{mn} and b_{mn} used to determine the interatomic energy in the Peierls-Nabarro model can also be obtained by numerical integral of EAM calculating

$\gamma(\bar{u}_x, \bar{u}_y)$ points. The coefficients of the {111} slip plane γ-surface for Cu are summarized in Table 2-4. More γ-surface coefficients can be referred to the appendix.

Table 2-4 Fourier coefficients of the {111} slip plane γ-surface for Cu (in unit of mJ/m^2)

	m / n	0	1	2	3	4	5
a_{mn}	0	358.2286	0	-97.40841	0	4.48977	0
	1	0	-194.8168	0	-48.42981	0	-3.07021
	2	-24.2149	0	8.97953	0	-3.07021	0
	3	0	-3.07021	0	1.35728	0	0.37411
	4	-0.2277	0	0.37411	0	-0.12366	0
	5	0	0.03028	0	0.07362	0	-0.03780
b_{mn}	0	0	0	152.31662	0	9.76717	0
	1	0	-304.6332	0	0	0	5.66783
	2	0	0	-19.53435	0	-5.66783	0
	3	0	-5.6678	0	0.51707	0	-0.13598
	4	0	0	-0.13598	0	-0.49043	0
	5	0	-0.1943	0	0.07380	0	0.12863

These coefficients a_{mn} and b_{mn} are not independent to each other since the three fold rotational symmetry is not introduced in above Fourier expansion. If the rotational symmetry is considered and set $\bar{x} = 2\pi\bar{u}_x$ and $\bar{y} = 2\pi\bar{u}_y$, the expansion for FCC metals should be

$$\gamma(\bar{x},\bar{y}) = \sum_{m,n} c_{mn}\left[\cos m\bar{x}\cos(2n-m)\bar{y} + \cos n\bar{x}\cos(2m-n)\bar{y} + \cos(n-m)\bar{x}\cos(m+n)\bar{y}\right] + \sum_{m,n} d_{mn}\left[\cos m\bar{x}\sin(2n-m)\bar{y} + \cos n\bar{x}\sin(2m-n)\bar{y} - \cos(n-m)\bar{x}\sin(m+n)\bar{y}\right] \quad (2\text{-}34)$$

(Schoeck, 2003; 2005) and thus the coefficients a_{mn} and b_{mn} have the relation of $a_{mn} = b_{mn} = 0$ (m + n is odd), $a_{mm} = 2a_{0(2m)}$, $b_{mm} = -2b_{0(2m)}$ $a_{13} = 2a_{20}$, $a_{31} = a_{24} = a_{15}$, $b_{31} = b_{24} = -b_{15}$… Nevertheless these relations are automatically satisfied in Eq. (2-34) since the

sample points used for numerical integration are already rotational symmetric. Therefore, we can conveniently use the general expansion form for both BCC and FCC metals without regarding the different rotational symmetries.

2.4 Example Studies

The incorporation of the generalized stacking fault energy (γ-surface) into the Peierls-Nabarro model allows for dealing with dislocations with mixed screw and edge components. One application of this extended Peierls-Nabarro model is to determine the core structure of a dissociated dislocation consisting of two Shockley partials connected by the intrinsic stacking fault in FCC metals. Because of the various intrinsic stacking fault energies (γ_{sf}), the widths of the dissociated dislocations, defined by the separation distance between the consisting two Shockley partials, are various for different FCC metals. The width of the straight dissociated dislocation is important for determining the presence of the intrinsic stacking faults. The width may be estimated by the continuum theory. The Shockley partials in a dissociated dislocation repel each another by a force that varies as $\mathbf{b}_1 \cdot \mathbf{B} \cdot \mathbf{b}_2 / 2\pi r$, where r is the separation between the partials; $\mathbf{B}$ is the energy factor as in Eq. (2-8); and $\mathbf{b}_1$, $\mathbf{b}_2$ are the Burgers vectors of the partials. The formation of the stacking fault between the partials produces an increase in energy per unit length; this energy leads to an attractive force per unit length between partials by γ_{sf}. At the equilibrium separation r_e, the attractive force is equal and opposite to the repulsive elastic force. Thus, if the coordinator system is setting as $\mathbf{x}_2 = \mathbf{n}$, $\mathbf{x}_3 = \xi$ where $\mathbf{n}$ is the

normal direction of the slip plane and $\boldsymbol{\xi}$ is the sense of the dislocation, the equilibrium separation can be given by

$$\frac{r_e}{b} = \frac{b}{8\pi\gamma_{\mathrm{sf}}} \frac{(B_{11}+B_{33}) - 2(B_{11}-B_{33})\cos 2\beta}{3} \tag{2-35}$$

where **b** is the total Burgers vector of the dissociated dislocation ($\mathbf{b} = \mathbf{b}_1 + \mathbf{b}_2$); β is the angle between the total Burgers vector and the sense of the dislocation ($\cos\beta = \mathbf{b}\cdot\boldsymbol{\xi}$). The total dislocation is a screw one when $\beta = 0°$ and it is an edge dislocation when $\beta = 90°$. The tensor B_{ij} also depends on the angle β. However, the term B_{13} always equals to zero when the slip plane is {111} plane because of the symmetry of the material constants tensor C_{ijkl} in the cubic lattice crystal. For the angle $\beta = 0°$, the tensor **B** can be analytically integrated as (Hirth and Lothe, 1982)

$$B_{33} = K_s = \sqrt{C'_{44}C'_{55}}\,,\ B_{11} = K_e = \frac{1}{3}\left(2 + \frac{C'_{22}}{\overline{C}'_{11}}\right)\left(\overline{C}'_{11}+C'_{12}\right)\sqrt{\frac{C'_{55}\left(\overline{C}'_{11}-C'_{12}\right)}{C'_{22}\left(\overline{C}'_{11}+C'_{12}+2C'_{55}\right)}} \tag{2-36}$$

where

$$\begin{aligned}
&\overline{C}'_{11} = \sqrt{C'_{11}C'_{22}} \\
&C'_{11} = C_{11} \quad C'_{22} = C_{11} + \frac{h}{2} \\
&C'_{12} = C_{12} \quad C'_{23} = C_{12} - \frac{h}{2} \\
&C'_{55} = C_{44} \quad C'_{44} = C_{44} - \frac{h}{2} \\
&h = 2C_{44} + C_{12} - C_{11}.
\end{aligned} \tag{2-37}$$

According to Eq. (2-35), normally the FCC metal with lower γ_{sf} has larger separation distance e.g. Cu ($\gamma_{sf} = 0.0032\mu b$) and Al ($\gamma_{sf} = 0.0185\mu b$) is on the contrary. Therefore, three metals Al, Ni and Cu are selected to analysis due to their various γ_{sf}.

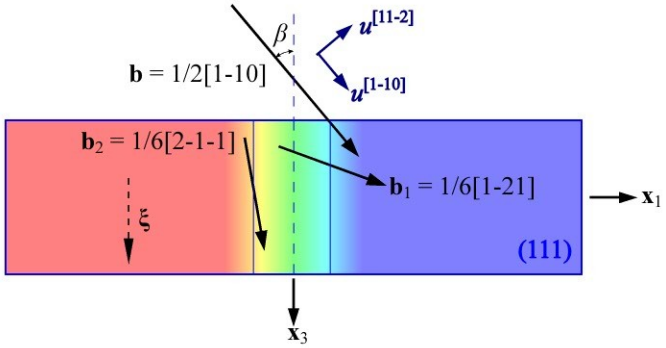

Figure 2-6. Dissociation of a perfect dislocation into Shockley partials.

The configuration of the simulation is set up as in Fig. 2-6. The slip plane is generally selected as (111) plane. The coordinator system is setting as $\mathbf{x}_1 = \mathbf{n} \times \boldsymbol{\xi}$, $\mathbf{x}_2 = \mathbf{n}$, $\mathbf{x}_3 = \boldsymbol{\xi}$ where $\mathbf{n}$ is the normal direction of the slip plane and $\boldsymbol{\xi}$ is the sense of the dislocation. The mixed perfect dislocation is inclined at an angle β to its Burgers vector. The partials $\mathbf{b}_1 = 1/6[1\bar{2}1]$ and $\mathbf{b}_2 = 1/6[2\bar{1}\bar{1}]$ are inclined at $\beta \pm 30°$. The displacement discontinuities can always be decomposed into two components: one along the total Burgers vector direction ($u^{[1\bar{1}0]}$) and the other along the perpendicular direction ($u^{[11\bar{2}]}$) no matter at what angle the dislocation is inclined. The dislocations are considered to be straight so that 2D simplification can be performed by Eq. (2-11). The simulation is initialized by introducing a complete idealistic intrinsic stacking fault with ($2L$) the width estimated by Eq. (2-35). Setting $u^{[1\bar{1}0]}(-L < x_1 < L) = b/2$, $u^{[11\bar{2}]}(-L < x_1 < L) = -\sqrt{3}b/6$,

$u^{[1\bar{1}0]}(x_1 \le -L) = b$ and other displacement discontinuities to be 0, the relaxation by Newton-Raphson iteration leads to the dissociated core structure. This core structure is actually independent on the initial width of the intrinsic stacking fault. Fig. 2-7 shows the core structure profiles of Al, Ni and Cu respectively under different inclined angles β.

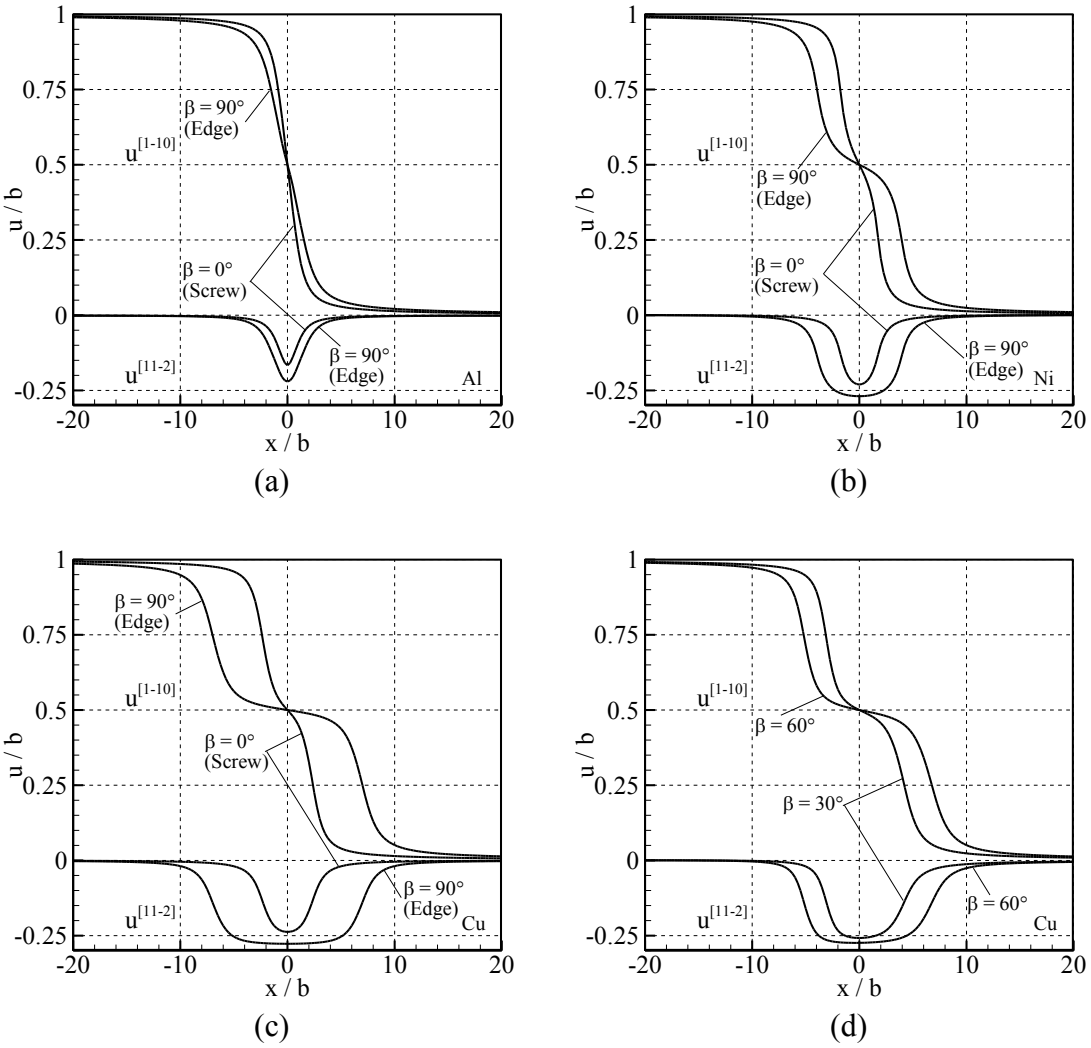

Figure 2-7. Core structure profiles of dissociated dislocations for different inclined angles: (a) Al, (b) Ni and (c) (d) Cu.

It shows that the intrinsic stacking fault can span more widely in the edge dissociated dislocation than the screw dislocation for all the three metals. The simulation also indicates that the intrinsic stacking fault is obvious in Cu and is not clear in Al, which agrees well with the experiment observation. The separation distance between the two dissociated partials can be measured from the profiles. The positions of the partials can be defined as the points at which the displacement continuities component $u^{[1\bar{1}0]}$ becomes equal to $b/4$ or $3b/4$. The separation distances for FCC metals Al, Ni and Cu as a function of the inclined angle β are plotted in Fig. 2-8 along with the estimated values by Eq. (2-35). The discrepancy between the simulation results and the estimates comes from the fact that the area between the partials is not an idealistic intrinsic stacking fault according to the core structure profiles in Fig. 2-7. The discrepancy is relatively small when the intrinsic stacking fault is wide and trends to be more idealistic. It will be

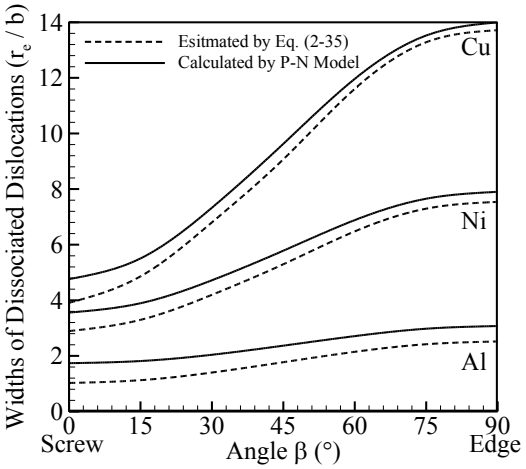

Figure 2-8. Widths of dissociated dislocations as a function of the inclined angle β in the FCC metals of Al, Ni and Cu.

discussed in later chapters about how the width affects the dislocation behavior in the FCC metals.

Without taking the straight dislocation simplification, a dissociated dislocation loop can be simulated using the general 3D integral formulas e.g. Eq. (2-3). Then the effects of the curved dislocation line to the width can be analyzed. In the homogenous media, a dislocation loop is a saddle-point configuration once it is nucleated, and it can expand assisted by a decreasing external shear stress (Xu, 2000). In this part, because we mainly concern about the width of dissociated dislocation loop, the nucleation process of the dislocation loop is not involved. Selecting the coordinator system as $\mathbf{x}_1 = 1/\sqrt{2}[1\,\bar{1}\,0]$, $\mathbf{x}_2 = 1/\sqrt{3}[1\,1\,1]$, and $\mathbf{x}_3 = 1/\sqrt{6}[\bar{1}\,\bar{1}\,2]$, and applying the external stress only along $\mathbf{x}_1$ direction, one possible dislocation loop configuration in Al is calculated using the similar approach for the straight dislocations. Fig. 3-9 shows the contour plot of the displacement continuities field and two components along $[1\,\bar{1}\,0]$ and $[\bar{1}\,\bar{1}\,2]$ direction are plotted separately. The applied shear stress for this configuration is determined as $0.028C_{44}$. At this stress level, the radius of the dislocation loop is about 16b along the $[1\,\bar{1}\,0]$ direction and 11b along the $[\bar{1}\,\bar{1}\,2]$ direction. The shape is consistent with expectation based on anisotropic line tension. The width of the dissociated dislocation loop is measured as 3.16b for the edge segments and 2.13b for the screw segments.

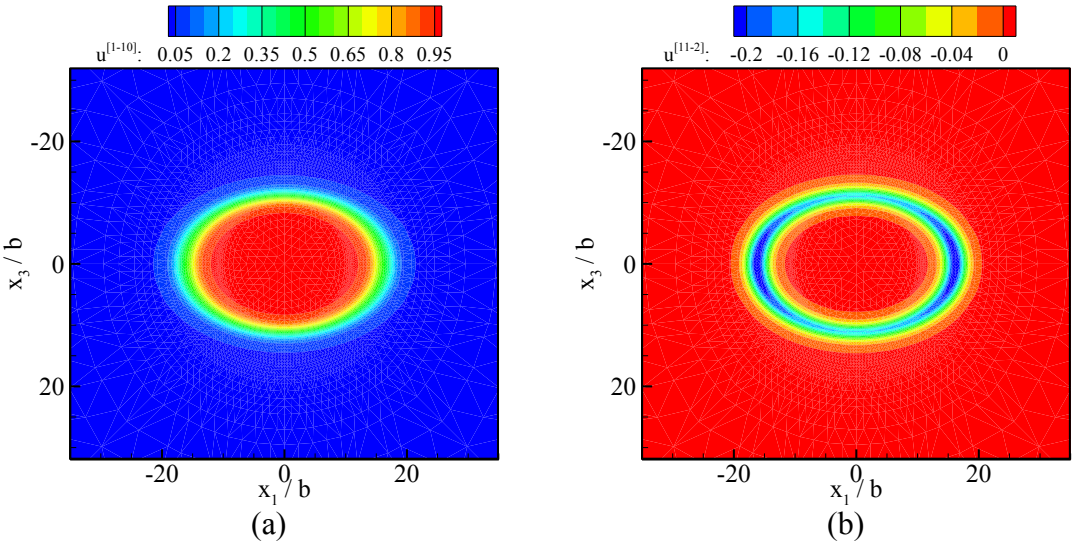

Figure 2-9. Contour plot of the displacement continuities profile of a dissociated dislocation loop: (a) the $u^{[1\bar{1}0]}$ components, and (b) the $u^{[\bar{1}\bar{1}2]}$ components.

Overall, by incorporating the generalized stacking fault energy, the variational boundary integral formulation based on the Peierls-Nabarro dislocation frame work is a powerful and reliable method to simulate the dissociated dislocation consisted by partial dislocations and intrinsic stacking faults in FCC metals. This method can be further used to analyze the partial dislocation behaviors, e.g. nucleation of partial dislocations at a crack and the cross-slip of a partial dislocation, which are important phenomena to affect the behavior of the FCC metals.

Chapter 3 Nucleation of Partial Dislocations at a Crack

3.1 Introduction

Dislocation nucleation at cracks has been of considerable interest because of its significant implications on brittle versus ductile behavior of crystalline materials (Rice and Thomson, 1974; Argon, 1987; Schoeck and Puschl, 1991; Rice, 1992; Rice and Beltz, 1994; Xu, et al., 1995, 1997; Kysar, 2003; Zhu, et al., 2004). When an atomically sharp crack in a perfect crystal is subjected to an increasing loading, the stress concentration at the crack tip can eventually initiate either Griffith cleavage fracture between atomic layers or dislocation nucleation induced plastic deformation. The competition between these two deformation modes plays an important role in determining whether the crystal is intrinsically ductile or brittle. Temperature and loading rate may also influence such competition because dislocation nucleation is a rate controlling process, although the activation energy required for thermally assisted dislocation nucleation at the crack appears to be too high for such a process to occur at the stress level markedly below the critical stress for athermal dislocation nucleation (Xu, et al., 1995; 1997). For the well known rapid brittle to ductile transition phenomena in a number of intrinsically brittle crystals such as silicon, tungsten, and iron, one should note the distinction that the process could be controlled by either the competition between cleavage fracture and dislocation nucleation at the crack or cleavage fracture and the motion and multiplication of shielding dislocations in the crack tip region. The study by Xu, et al. (1997) has shown that brittle to ductile transition in certain metals such as iron could be nucleation

controlled because of their high dislocation mobility while other studies indicate that such a transition in tungsten and silicon with relatively low dislocation mobility is more likely influenced by dislocation motion (Hartmaier and Gumbsch, 2002, 2005). In either case, the energetics of dislocation nucleation at cracks is of great importance for understanding the source of dislocations and its influences on mechanical behavior of crystalline materials.

The energetics of dislocation nucleation at cracks has been previously analyzed through the incorporation of the Peierls-Nabarro dislocation model (Peierls, 1941; Nabarro, 1947; Hirth and Lothe, 1982) along the slip planes at the cracks (Schoeck and Puschl, 1991; Rice, 1992; Rice and Beltz, 1994; Xu, et al., 1995, 1997). These analyses generally adopted the constrained path assumption, i.e., the slip between the adjacent atomic layers is assumed to be in the Burgers vector direction, which is not applicable to complex nucleation configurations that include partial dislocations and stacking faults. Many recent studies of nanostructured metals appear to indicate that certain mechanical behavior of nanostructured metals such as the limit strength and the strong strain rate sensitivity may be controlled by nucleation of partial dislocations at stress concentration sites on grain boundaries and their subsequent generation of stacking faults across nano-sized grains (Asaro and Suresh, 2005). A preliminary analysis using continuum elastic dislocation theory is insightful but needs the incorporation of sufficient atomic information to delineate the influence of various atomic configurations and parameters on the nucleation process. It is this problem that motivated us to study partial dislocation nucleation at a crack using the relatively more definitive Peierls-Nabarro dislocation

model. The model allows for incorporation of atomic information into continuum mechanics based method to more faithfully account for dislocation core structure. We choose the crack configuration because of its generic interest as well as its well characterized stress concentration. One should bear in mind that dislocation nucleation is largely a high stress driven process. In nanostructured metals, it is most likely to occur at heterogeneities on grain boundaries or surfaces where high stress concentrations exist.

In general, two conditions are of particular interest for understanding dislocation nucleation behavior. One is the critical stress for athermal nucleation, which occurs instantaneously at absolute zero temperature. The other is the activation energy required for thermally assisted nucleation at a stress level below the critical stress for athermal nucleation. The critical conditions for nucleation of full dislocations in various configurations, including cracks, have been extensively studied in the literature (e.g., Rice, 1992; Rice and Beltz, 1994; Xu, et al., 1997; Xu and Argon, 2000; Xu and Zhang, 2003; Li and Xu, 2006). Because of the formation of intrinsic stacking faults during the nucleation process, nucleation of a pair of partial dislocations accompanied by a stacking fault, however, appears to be different from nucleation of a full dislocation in many aspects. Specifically, the leading partial is nucleated first and leaves an intrinsic stacking fault connected to the crack front. The critical condition for nucleation of the trailing partial is then influenced by the stacking fault and the position of the leading partial. Depending on the critical conditions for both partial nucleation processes, nucleation of the trailing partial could occur either simultaneously with the leading partial or after the leading partial is driven far away from the crack front under increasing loading.

Nucleation of partial dislocations from a crack in a two dimensional configuration has been first analyzed by Rice (1992). The critical stresses required for nucleation of the leading and trailing partials are obtained by applying the constrained path assumption separately to each partial. The constrained path assumption may cause significant errors especially for a pair of curved partial dislocation configurations when significant slip involved in the configuration does not strictly follow the partial Burgers vector direction. By incorporating the generalized stacking fault energy into the fully three dimensional boundary integral formulation of the Peierls-Nabarro dislocation model, slip is allowed in all directions along the slip plane and constrained path assumption is no longer necessary. The generalized stacking fault energy is obtained based on direct atomistic calculations so that the influence of atomic parameters on dislocation nucleation can be most faithfully accounted. The unstable saddle-point configurations of embryonic dislocations in general three dimensional configurations are solved by controlling slip through the Lagrange multiplier method in the continuum mechanics based variational boundary integral method. The critical conditions for nucleation of both leading and trailing partial dislocations at the crack in Al and Cu are determined.

3.2 Modeling

We consider the configuration of an atomically sharp as shown in Fig. 3-1. The slip plane is along the extension of the crack. Between adjacent atomic layers along the slip plane is incorporated with the nonlinear interatomic layer potential. The crack is subjected to shear loading characterized by the standard *K*-field with the stress intensity

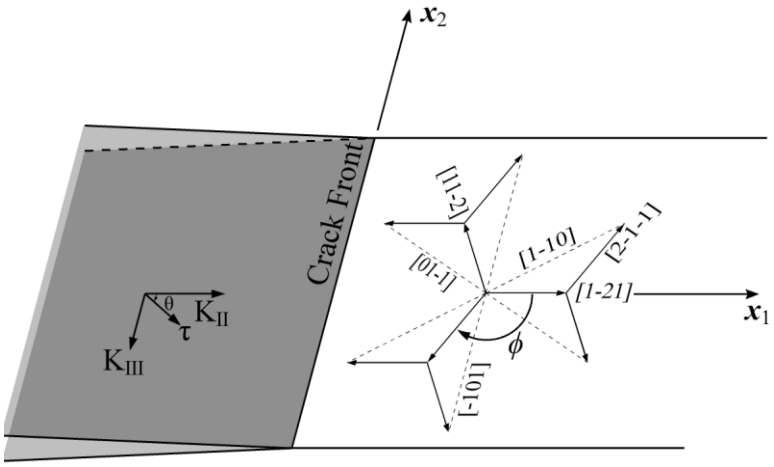

Figure 3-1. Configuration of a semi-infinite crack in an anisotropic crystal.

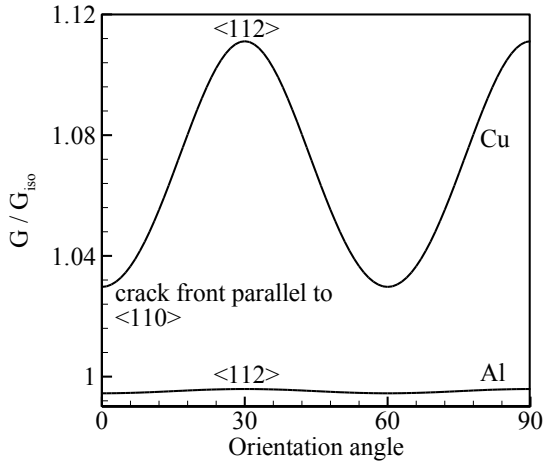

Figure 3-2. Dependence of the energy release rate on crack front orientation on {111} crack surface in Al and Cu. The preferred crack front direction is $\langle 110 \rangle$ for both Al and Cu.

factors K_{II} and K_{III}. For convenience, we represent $K_{II} = K\cos\theta$ and $K_{III} = K\sin\theta$, where K is a single combined stress intensity factor and θ is the arctangent of the ratio K_{III}/K_{II}, which is aligned with the shearing direction at the crack front. As the shear loading increases from zero, the stress concentration at the crack front induces slip, i.e., a relative displacement between the adjacent atomic planes along the slip plane, which eventually leads to the formation of a dislocation emanating from the crack front. We select FCC metals Al and Cu for the following comparative studies for their distinctive difference in the intrinsic stacking fault energy and its potential influence on the formation of the stacking fault at the crack front. The slip plane in both metals is the {111} plane. The preferred crack front direction is chosen by following the approach presented in Xu, et al. (1997) in which the variation of the energy release rate of a tensile crack as a function of the crack front orientation is calculated. The orientation with the minimum energy release rate is the most favored crack front orientation. Results as shown in Fig. 3-2 suggest that the preferred crack front orientation of cleavage fracture on the {111} plane in both Al and Cu is parallel to the <110> direction, although Cu appears to be far more anisotropic than Al. For this crack front orientation, a full dislocation can be nucleated along six possible <110> directions, which can be split into six groups of Burgers vectors for corresponding leading and trailing partials as shown in Fig. 3-1. Note that there are only three possible Burgers vectors $\boldsymbol{b}_L$ for the leading partials: $1/6[1\bar{2}1]$, $1/6[11\bar{2}]$ and $1/6[\bar{2}11]$. Denote the angle between the crack front normal direction and the Burgers vector of the leading partial as ϕ; the possible Burgers vectors of the leading partials are along $\phi = 0°$, $\phi = 120°$, and $\phi = -120°$. The choice of the direction is

determined by the shear loading angle θ: for $-60° < \theta < 60°$, $\boldsymbol{b}_L = 1/6[1\bar{2}1]$, $\phi = 0°$; for $60° < \theta < 180°$, $\boldsymbol{b}_L = 1/6[11\bar{2}]$, $\phi = 120°$; and for $-180° < \theta < -60°$, $\boldsymbol{b}_L = 1/6[\bar{2}11]$, $\phi = -120°$. The anisotropic material constants are used in the calculations unless the isotropic material constants are specified. The anisotropic material constants are chosen to be consistent with the atomic potentials used for the calculations of the generalized stacking fault energies.

Following the methodology described in Chapter 2, the solution of $\mathbf{u}(\mathbf{x})$, both the crack opening displacements and displacement discontinuities along the slip planes, can be obtained by the minimization of the total energy

$$\Pi[\mathbf{u}(\mathbf{x})] = W[\mathbf{u}(\mathbf{x})] + V[\mathbf{u}(\mathbf{x})] - P[\mathbf{u}(\mathbf{x})] \tag{3-1}$$

where W is the elastic strain energy, V is the interatomic layer potential energy, and P is the work of the external force. The expression for these three terms can be referred to Eq. (2-3), Eq. (2-13) and Eq. (2-14) in Chapter 2. For the semi-infinite crack, in order to reduce the computation on the finite domain, a mathematical treatment can be manipulated following the procedure introduced by Xu *et al*. (1995) and Xu and Ortiz (1993). The reduction can be achieved by writing the opening displacement of the crack surface and displacement discontinuities along the slip planes as

$$\mathbf{u} = \bar{\mathbf{u}} + \boldsymbol{\delta} \tag{3-2}$$

where $\bar{\mathbf{u}}$ represents the standard K displacement field for a reference semi-infinite crack and can be expressed as $\bar{\mathbf{u}} = \mathbf{0}$ for $x_1 \geq 0$ and

$$\bar{u}_i = 4B_{ij}^{-1}K_j\sqrt{\frac{-x_1}{2\pi}} \tag{3-3}$$

for $x_1 < 0$. Note that in this notation the stress intensity factor component K_1, K_2, and K_3 represents K_{II}, K_{III}, and K_I, respectively. The expression for **B** is identical to the pre-logarithmic energy factor of the interaction energy of parallel straight dislocations in Eq. (2-8) and **B** depends only on the direction of the dislocation of the crack front. The term $\bar{\mathbf{u}}$ matches the behavior of the opening displacements far away from the tip. Consequently, the remaining term $\boldsymbol{\delta}$, which is the primary unknown in the calculations, decays rapidly to zero with the distance away from the crack tip. In this manner, $\boldsymbol{\delta}$ can be restricted to a finite domain $\hat{S}_C \cup \hat{S}_S$, where $\hat{S}_C$ lies on the crack surface and $\hat{S}_S$ on the slip plane. Then, the potential energy of the crack and slip plane system can be written as

$$\Pi[\bar{\mathbf{u}}+\boldsymbol{\delta}] = W[\bar{\mathbf{u}}+\boldsymbol{\delta}] + V[\boldsymbol{\delta}] = W[\bar{\mathbf{u}}] + W[\boldsymbol{\delta}] + V[\boldsymbol{\delta}] + W_2[\bar{\mathbf{u}},\boldsymbol{\delta}] \tag{3-4}$$

where $W[\bar{\mathbf{u}}]$ is identified as the self energy of the loaded elastic solid according to the conventional solution in which $\boldsymbol{\delta}$ is constrained to be zero; $W[\boldsymbol{\delta}]+V[\boldsymbol{\delta}]$ is the self energy of the system of the modifications consisting of the distributed dislocations and the interlayer interaction energy on the slip plane; and $W_2[\bar{\mathbf{u}},\boldsymbol{\delta}]$ is the interaction of the initial unmodified standard *K*-field with the second system of modifications. Hence, $W[\boldsymbol{\delta}]$ can be expressed according to Eq. (2-3) on the domain of $\hat{S}_C \cup \hat{S}_S$; $V[\boldsymbol{\delta}]$ can be expressed according to Eq. (2-13) on the domain of $\hat{S}_S$; and $W_2[\bar{\mathbf{u}},\boldsymbol{\delta}]$ can be expressed as

$$W_2[\bar{\mathbf{u}},\boldsymbol{\delta}] = -\int_{\hat{S}_S} \mathbf{n}\cdot\boldsymbol{\sigma}\cdot\boldsymbol{\delta}\, dS \tag{3-5}$$

where $\boldsymbol{\sigma}$ is the stress of the standard *K*-field on the extended slip plane of the crack surface and for the semi-infinite crack surface referred in Fig. 3-1, $\boldsymbol{\sigma}$ can be expressed as

$$\sigma_{3i} = \frac{K_i}{\sqrt{2\pi x_1}},\ \sigma_{11} = \sigma_{22} = \sigma_{12} = 0\,. \tag{3-6}$$

The minimization of the potential energy $\Pi[\bar{\mathbf{u}} + \boldsymbol{\delta}]$ with respect to the displacement $\boldsymbol{\delta}$ leads to nonlinear integral equations. The displacements are discretized through the standard finite elements. The resulting nonlinear equations are solved by Newton-Raphson iterations. The saddle-point configurations of dislocations in the nucleation process are solved by recourse to displacement control through Lagrange multiplier method. The details of these numerical treatments refer to Xu and Ortiz (1993) and Xu, et al. (1995).

3.3 Nucleation of Straight Partial Dislocations

We begin by considering nucleation of a straight dislocation parallel to the crack front. For this two dimensional case the elastic energy equation can be simplified to Eq. (2-11). It reduces the surface integration to the line integration, which improves not only the efficiency but also the accuracy of the integration. Therefore, the potential energy in Eq. (3-4) can be simplified to

$$\overline{\Pi}[\boldsymbol{\delta}(x)] = \overline{W}_0 + \int_{-\infty}^{+\infty}\int_{-\infty}^{+\infty} \frac{d\delta_i(x')}{dx'}\frac{d\delta_j(x)}{dx}\frac{B_{ij}}{4\pi}\ln\frac{1}{|x-x'|}dxdx' + \int_0^{+\infty}\overline{\Phi}(\boldsymbol{\delta})dx - \int_0^{+\infty}\frac{K_i\delta_i(x)}{\sqrt{2\pi x}}dx \tag{3-7}$$

where $\overline{W}_0$ is the elastic energy per unit length of the standard *K*-field and independent on $\boldsymbol{\delta}$; and x, x' is the short for x_1 and x_1' respectively. In the numerical analysis of the crack and slip plane that are co-planar, the integration in Eq. (3-7) can be further reduced on the domain of the slip plane using the condition that the crack surface is traction free.

First, consider a dislocation on the extended slip plane with a distance of ρ from the crack front and its profile can be presented by $\delta_i(0 < x < \rho) = -b_i$ and $\delta_i(x > \rho) = 0$ as illustrated in Fig. 3-3. In anisotropic solids, the stresses on the slip plane of a dislocation with the Burgers vector of **b** can be written as

$$\sigma_{3i} = -\frac{B_{ij}}{2\pi}\frac{b_j}{r} \tag{3-8}$$

where r is the distance from the dislocation on the slip plane. Invoking the principle of superposition, the free traction condition on the crack surface can then be expressed as

$$F_i = \frac{B_{ij}}{2\pi}\left(\int_{-\infty}^{0}\frac{d\delta_j(x')}{dx'}\frac{1}{x'-x}dx' + \frac{b_j}{\rho - x}\right) = 0, \quad (x < 0). \tag{3-9}$$

Because the matrix B_{ij} is positive-definite symmetric, the solution of $d\delta_i(x)/dx$ in Eq. (3-9) can be calculated by the inverse Hilbert transformation as

$$\frac{d\delta_i(x)}{dx} = \frac{1}{\pi^2\sqrt{-x}}\int_{-\infty}^{0}\frac{\sqrt{-x'}}{x'-x}\frac{b_i}{\rho - x'}dx' = \frac{b_i}{\pi}\frac{1}{x-\rho}\sqrt{\frac{\rho}{-x}}, \quad (x < 0). \tag{3-10}$$

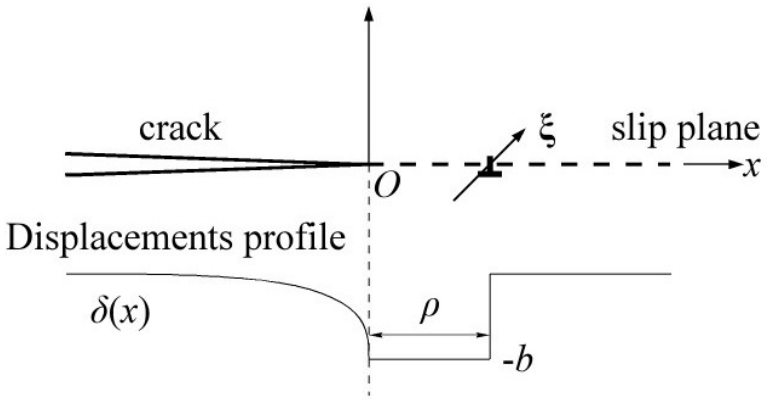

Figure 3-3. Illustration of a dislocation in a semi-infinite crack.

Invoking the principle of superposition, the crack opening displacements can be expressed as a function of the displacement continuities on the extended slip plane as

$$\frac{d\delta_i(x)}{dx} = \int_0^{+\infty} \frac{1}{\pi} \frac{d\delta_i(x')}{dx'} \frac{1}{x-x'} \sqrt{\frac{x'}{-x}} dx', \quad (x<0). \tag{3-11}$$

Then, for $x>0$, the integration of $d\delta_i(x)/dx$ on the crack surface can be expressed as integration only on the domain of the slip plane:

$$\int_{-\infty}^{0} \frac{d\delta_i(\xi)}{d\xi} \frac{1}{\xi-x} d\xi = \frac{1}{\pi} \int_0^{+\infty} \frac{d\delta_i(x')}{dx'} \left(\int_{-\infty}^{0} \frac{1}{\xi-x'} \sqrt{\frac{x'}{-\xi}} \frac{1}{\xi-x} d\xi \right) dx' = \int_0^{+\infty} \frac{d\delta_i(x')/dx'}{x+\sqrt{xx'}} dx'. \tag{3-12}$$

Therefore, the second term in Eq. (3-7), representing the self elastic energy of the displacements modification, can be written as

$$\begin{aligned} W[\boldsymbol{\delta}] &= \frac{B_{ij}}{2\pi} \int_{-\infty}^{+\infty} \int_{-\infty}^{+\infty} \frac{d\delta_i(x')}{dx'} \frac{d\delta_j(x)}{dx} \ln \frac{1}{|x'-x|} dx dx' = -\frac{B_{ij}}{2\pi} \int_0^{+\infty} \delta_j(x) \int_{-\infty}^{+\infty} \frac{d\delta_i(x')}{dx'} \frac{1}{x'-x} dx' dx \\ &= -\frac{B_{ij}}{2\pi} \int_0^{+\infty} \delta_j(x) \int_0^{+\infty} \frac{d\delta_i(x')}{dx'} \left(\frac{1}{x'-x} + \frac{1}{x+\sqrt{xx'}} \right) dx' dx \\ &= \frac{B_{ij}}{2\pi} \int_0^{+\infty} \delta_j(x) \int_0^{+\infty} \sqrt{\frac{x'}{x}} \frac{d\delta_i(x')/dx'}{x-x'} dx' dx \\ &= \frac{B_{ij}}{2\pi} \int_0^{+\infty} \int_0^{+\infty} \frac{d\delta_i(x')}{dx'} \frac{d\delta_j(x)}{dx} \ln \left| \frac{\sqrt{x}+\sqrt{x'}}{\sqrt{x}-\sqrt{x'}} \right| dx' dx \end{aligned}. \tag{3-13}$$

Finally, the integral formulas only on the domain of the slip plane is

$$\overline{\Pi}[\boldsymbol{\delta}(x)] = \frac{B_{ij}}{2\pi} \int_0^{+\infty} \int_0^{+\infty} \frac{d\delta_i(x')}{dx'} \frac{d\delta_j(x)}{dx} \ln \left| \frac{\sqrt{x}+\sqrt{x'}}{\sqrt{x}-\sqrt{x'}} \right| dx' dx + \int_0^{+\infty} \overline{\Phi}(\boldsymbol{\delta}) dx - \int_0^{+\infty} \frac{K_i \delta_i(x)}{\sqrt{2\pi x}} dx. \tag{3-14}$$

The final integration is mathematically equivalent to Eq. (8) in Rice (1992) if the material is assumed to be isotropic.

3.3.1 Nucleation of leading partial dislocations

Consider the configuration as shown in Fig. 3-1. As the shear loading increases from zero, the stress concentration on the slip plane near the crack induces stable slip until the shear loading reaches the critical value at which the slip becomes unstable, forming a leading partial dislocation emanating from the crack. The critical stress intensity factor for nucleation of the leading partial varies with the orientation angle ϕ (the angle between the Burgers vector of the leading partial and crack front) and the shearing angle θ. Using *J*-integral, Rice gave a nucleation criterion for isotropic solids as

$$K_{\mathrm{II}}\cos\phi + K_{\mathrm{III}}\sin\phi = \sqrt{\frac{2\mu}{1-\nu}\left[\cos^2\phi + (1-\nu)\sin^2\phi\right]\gamma_{\mathrm{us}}} \tag{3-15}$$

where γ_{us}, defined as the unstable stacking fault energy, is the maximum value of γ along the constrained slip path in the Burgers vector direction. For anisotropic solids, the energy release rate is $G = \frac{1}{2}K_i B_{ij}^{-1} K_j$ where B_{ij} is the same variable as in Eq. (3-3). The corresponding nucleation criterion for the leading partial dislocation is given by

$$K_{\mathrm{II}}\cos\phi + K_{\mathrm{III}}\sin\phi = \sqrt{\gamma_{\mathrm{us}} p(\phi)} \tag{3-16}$$

where $p(\phi) = 2\left(B_{11}\cos^2\phi + B_{33}\sin^2\phi + B_{13}\sin 2\phi\right)$. Using the combined stress intensity factor *K*, the nucleation criterion can be re-casted as

$$\frac{K_C(\theta,\phi)}{K_C^{\mathrm{Ref}}} = \sqrt{\overline{B}_{11}\cos^2\phi + \overline{B}_{33}\sin^2\phi + \overline{B}_{13}\sin 2\phi}\,\frac{1}{\cos(\theta-\phi)} \tag{3-17}$$

where $K_C^{\mathrm{Ref}} = \sqrt{2\mu\gamma_{\mathrm{us}}/(1-\nu)}$ is the critical value for nucleation in the Voigt averaged isotropic solid when $\theta = 0$ and $\phi = 0$; $\overline{B}_{11}$, $\overline{B}_{33}$ are the normalized material constants

given by $\overline{B}_{ij} = B_{ij}(1-\nu)/\mu$. This equation suggests that the normalized critical stress intensity factor is linearly dependent on $1/\cos(\theta-\phi)$ with various slopes as a function of ϕ.

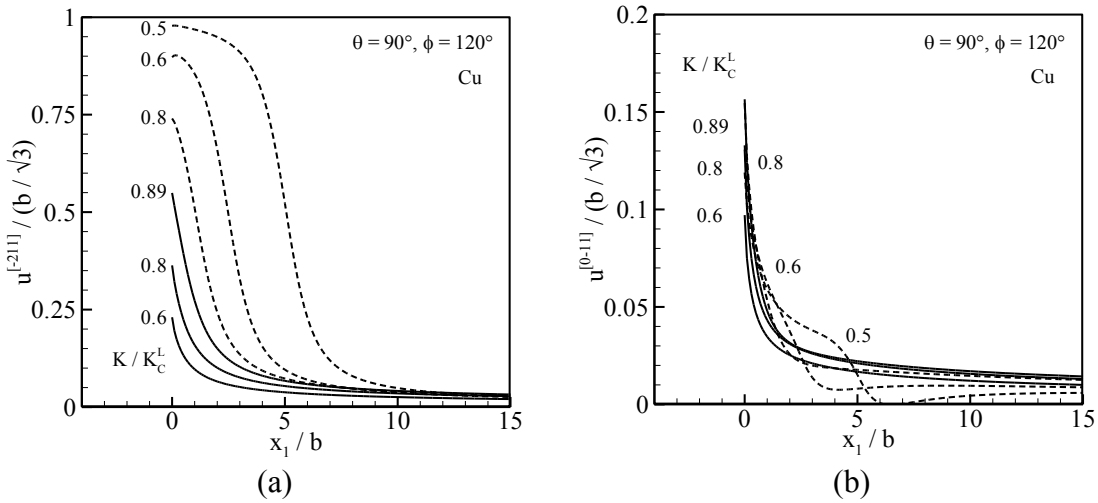

Figure 3-4. Sequence of the leading partial configurations at various loading levels for Cu ($\theta = 90°$, $\phi = 120°$). The configuration is represented by the shearing displacement components in $[\bar{2}11]$ (parallel to the partial Burgers vector) and $[0\,\bar{1}\,1]$ (perpendicular to the partial Burgers vector) directions. The solid lines represent the stable configurations while the dashed lines represent the saddle-point configurations. The relative critical loading for nucleation of the leading partial is $K_C^L = 0.89$.

For the configuration as shown in Fig. 3-1, the possible slip angle ϕ are 0°, 120°, and –120°. The corresponding shearing angle θ ranges from $\phi - 60°$ to $\phi + 60°$. Since the slip systems associated with $\phi = 120°$ and $\phi = -120°$ are symmetric, only two sets of calculations are performed for various shearing angle θ from –180° to 60° with a 10° interval. Using the case of $\theta = 90°$ and $\phi = 120°$ in Cu as an example, the relative

displacement components at the crack tip, both parallel and perpendicular to the Burgers vector direction, are plotted in Fig. 3-4 for various loading levels. All length parameters are normalized. The parameter b is the magnitude of the Burgers vector of the full dislocation. It can be seen from Fig. 3-4(b) that considerable lateral slip is involved, in contrast with zero lateral slip assumed in the constrained path assumption. The actual slip paths at the crack tip for various loading configurations on the background of the contour plot of the generalized stacking fault energy are plotted in Fig. 3-5. The dashed line represents the constrained path in the Burgers vector direction. Note that the actual slip paths in the figure represent the whole nucleation process, including both leading and trailing partials. At this stage the discussion is focused only on the first halves of the paths, which correspond to the nucleation processes of the leading partials. The figure shows that the slip path at the crack tip progressively deviates from the constrained path as the shear loading direction progressively deviates from the Burgers vector direction of the leading partial. The curved slip paths are influenced by material, loading configuration, and the landscape of the generalized stacking fault energy surface, as evidenced in the figures for both Al and Cu. For Cu with relatively low intrinsic stacking fault energy, most paths go through the area near the intrinsic stacking fault energy, which means the intrinsic stacking fault prevails in Cu under most shear conditions. On the contrary, for Al with relatively high intrinsic stacking fault energy, the fact that most paths do not go through the area near the intrinsic stacking fault energy means distinctive intrinsic stacking faults are rare, indicating that the trailing partial is most likely to follow the leading partial closely in the nucleation process. Along each path, the peak value of

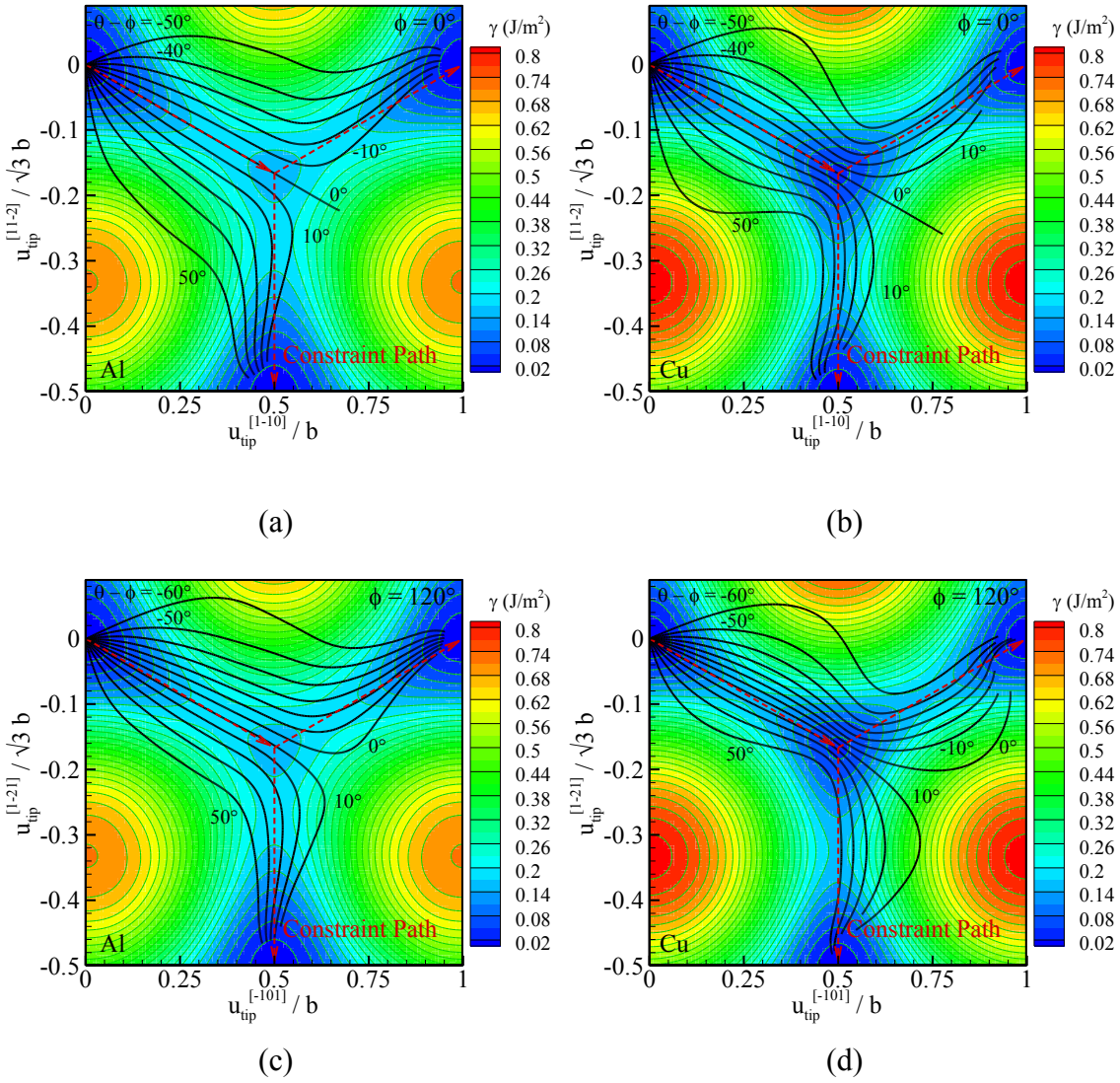

Figure 3-5. The slip paths at the crack tip for various loading directions. (a) Al, $\phi = 0°$; (b) Cu, $\phi = 0°$; (c) Al, $\phi = 120°$; (d) Cu, $\phi = 120°$; The dashed lines represent the constrained paths in the Burgers vector directions of partial dislocations.

the generalized stacking fault energy still represents the stage at which the partial can be fully formed, as the *J*-integral approach used for obtaining the nucleation criterion based on the constrained path assumption is still valid. However, an analytical solution for the criterion is hard to obtain because the slip path cannot be determined analytically anymore. Therefore, we plot numerical results of the critical loading for nucleation of the leading partial as a function of shearing angle θ in Fig. 3-6 for various ϕ. The Rice results based on the constrained path assumption is also plotted as a comparison. It is interesting to note that even the constrained path assumption becomes increasingly invalid as the shearing direction deviates from the Burgers vector direction, the analytical results nevertheless remain to be good approximations to the large extent.

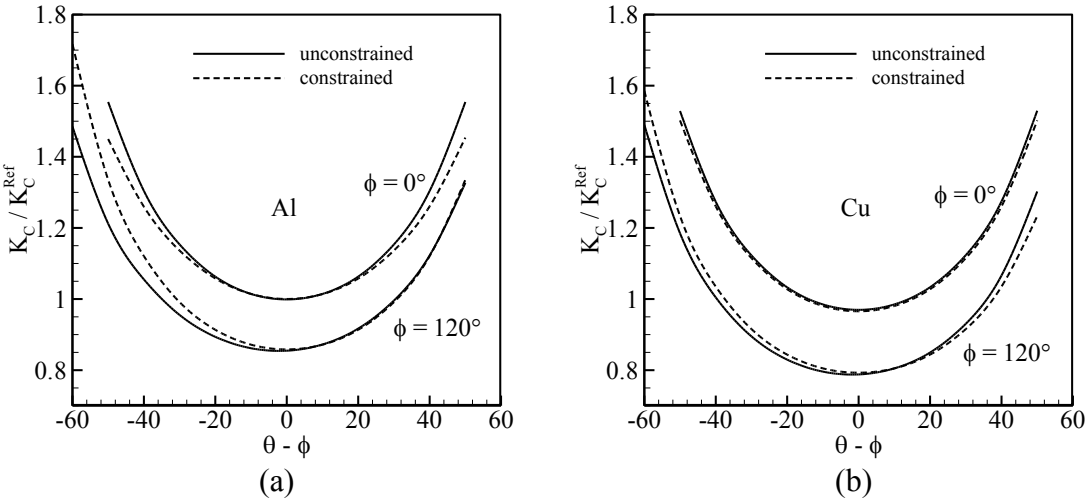

Figure 3-6. Critical loading for nucleation of the leading partial as a function of loading direction for (a) Al and (b) Cu.

3.3.2 Nucleation of trailing partial dislocations

When an embryonic full dislocation reaches its unstable configuration at the critical loading, it would emanate from the crack dynamically if the loading is maintained. Theoretically the dislocation may also emanate from the crack steadily at the decreasing loading as long as the loading is balanced unstably by the image stress, which attracts the dislocation back to the crack. Here the lattice resistance is negligible compared with other stresses in the crack tip region. The energy difference between the unstable and stable equilibrium configurations at the same loading level is the activation energy required for thermally assisted dislocation nucleation at that stress level, assuming that the change of the entropy of the system is negligible. Because the image stress of the embryonic dislocation keeps decreasing faster than the loading stress as the dislocation moves away from the crack ($1/r$ versus $1/\sqrt{r}$, r is the distance of the dislocation position to the crack tip), the fully nucleated dislocation at certain stress level keeps moving away from the crack till it is hindered by other obstacles or trapped by lattice resistance at far distance to the crack tip.

Compared with nucleation of the full dislocation, the nucleation process of a pair of partial dislocations is rather different. When the leading partial reaches its unstable configuration and moves away from the crack, it does not leave behind the perfect lattice structure but rather an intrinsic stacking fault of energy γ_{sf}. The leading partial always impedes nucleation of the trailing partial while the stacking fault facilitates it. The formation of the stacking fault also exerts a constant attraction force to the leading partial

as it moves away from the crack. All these factors have rather complicated influence on nucleation of the trailing partial. For example, for materials with relatively high stacking fault energy such as Al, the trailing partial may be nucleated instantaneously after the leading partial. On the other hand, for materials with relatively low stacking fault energy such as Cu, the leading partial has to be driven relatively far away from the crack before the trailing partial can be nucleated. Because of the low attracting force to facilitate nucleation of the trailing partial, additional loading may be required for its nucleation.

To illustrate the difference between nucleation of partials in Al and Cu, we consider a special loading configuration $\theta = 90°$ under which a dissociated screw dislocation is nucleated with the leading partial in the direction $\phi = 120°$. Note that in this special case the resolved shear stress components on both leading and trailing partials are the same. Both stable and unstable configurations are solved by controlling slip through the Lagrange multiplier method. The calculations are carried out till the trailing partial dislocation is fully formed for both Al and Cu.

Fig. 3-7 shows the sequence of the stable and unstable configurations of the dissociated dislocation at various loading levels for both Al and Cu. Only the slip component in $[\bar{1}01]$ direction is plotted. The solid lines represent stable configurations while the dashed lines unstable ones. Note the scale difference in the horizointal axes of Fig. 3-7 (a) and (b). For Al, the trailing dislocation is nucleated almost immediately after nucleation of the leading partial. For Cu, the trailing partial is not nucleated until the the leading partial is moved away from the crack (the nucleation configurations for the

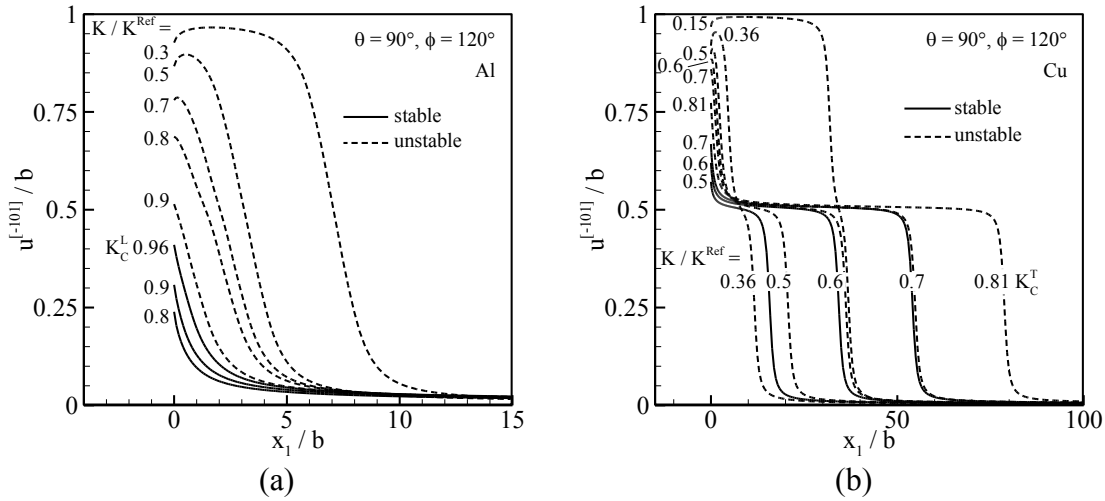

Figure 3-7. Sequence of the embryonic configurations of the dissociated dislocation ($\theta = 90°, \phi = 120°$) at various loading levels. (a) For Al, the trailing partial is nucleated almost immediately after nucleation of the leading partial; (b) For Cu, the trailing partial is nucleated only after the leading partial is moved relatively far away from the crack.

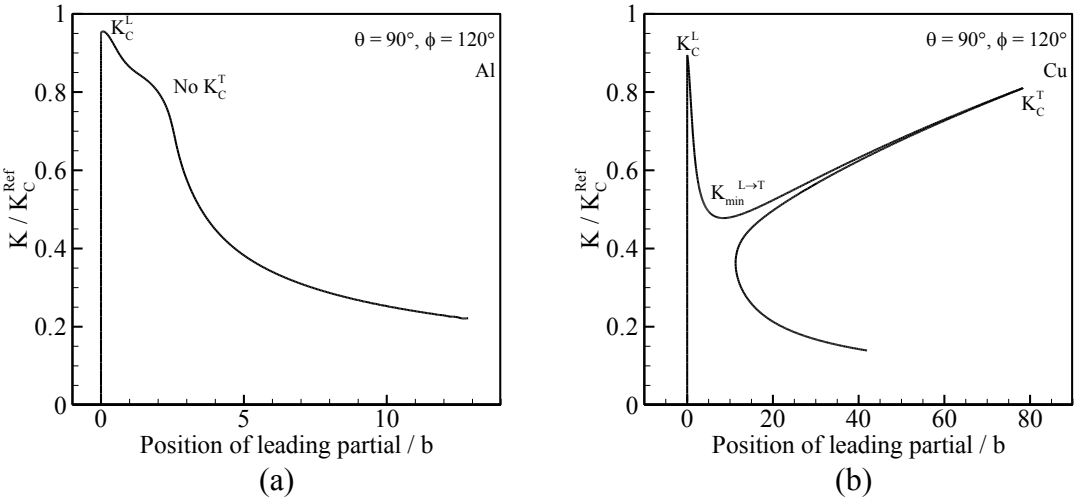

Figure 3-8. The equilibrium loading as a function of leading partial position for (a) Al and (b) Cu.

leading partial are omitted in Fig. 3-7(b) for better visualization). This difference may be better understood from Fig. 3-8, which plots the equilibrium loading level versus the position of the leading partial for both Al and Cu. The peaks denoted by K_C^L and K_C^T represent the critical loading for nucleation of the leading and trailing partials, respectively. The local minimum value $K_{min}^{L\to T}$ denotes the transition from the unstable to stable loading as the leading partial moves away from the crack. For Al, there is no peak value K_C^T. The trailing partial is nucleated almost immediately after the leading partial is nucleated. For Cu, nucleation of the trailing partial can only occur after the leading partial is moved relatively far away from the crack. The existence of $K_{min}^{L\to T}$ indicates that the loading needs to be increased to the new peak value K_C^T in order for nucleation of the trailing partial to occur. It should be noted that even K_C^T is lower than K_C^L, nucleation of the trailing partial cannot occur simultaneously because the critical loading for nucleation of the trailing partial would be significantly higher if the leading partial is still at the vicinity of the crack to impede nucleation. This phenomenon has significant implication on the formation of stacking faults. Although the width of the equilibrium stacking fault of a dissociated screw dislocation in Cu is only about 5*b*, the stacking fault formed during the nucleation process has to be significantly larger before the trailing partial can be nucleated. It is very likely that, for example, in a nano-grained crystal the leading partial is moved across the grain and pinned or absorbed by the grain boundary before the trailing partial is nucleated, resulting in a relatively large stable stacking fault across the

grain. Many atomistic simulations of the deformation process of Cu appear to confirm this phenomenon (Kumar, et al., 2003; Yamakov, et al., 2003).

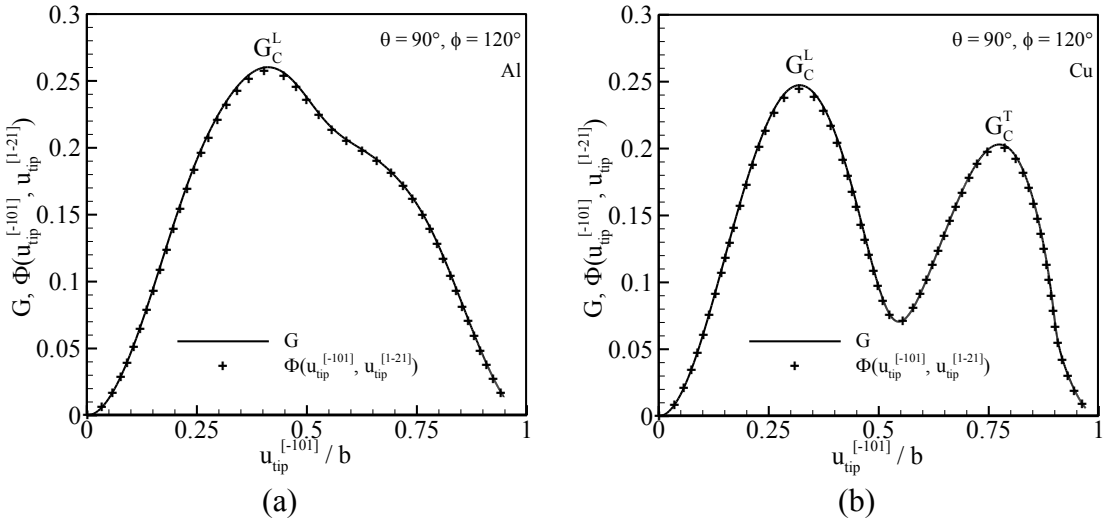

Figure 3-9. The enegery release rate is always equal to the generalized stacking fault energy at the crack tip during the nucleation process. The local maxium value represents the critical loading required for athermal nucleation of the leading or trailing partials.

It is interesting to note that the energy release rate is always equal to the generalized stacking fault energy at the crack tip during the nucleation process according to *J*-integral as shown in Fig. 3-9, which plots both of them versus the relative slip along the $[\bar{1}01]$direction. The local maximum value along the slip path of the crack tip therefore represents the critical loading for athermal nucleation of the leading or trailing partial. Since the slip path of the crack tip as shown in Fig. 3-5 is influenced by many factors, it is difficult to obtain simple formula to describe the criterion for partial dislocation nucleation. Using the constrained path assumption and *J*-integral to the entire dissociated dislocation, including the leading partial dislocation, the associated stacking fault zone,

and the incipient trailing partial dislocation, Rice (1992) gave a nucleation criterion of the trailing partial as

$$\begin{aligned}&\left(K_{\mathrm{II}}\cos\phi_{\mathrm{T}}+K_{\mathrm{III}}\sin\phi_{\mathrm{T}}\right)-\frac{b_{\mathrm{L}}}{\sqrt{2\pi r_{\mathrm{L}}}}\left[\mathrm{B}_{11}\cos\phi_{\mathrm{L}}\cos\phi_{\mathrm{T}}+B_{33}\sin\phi_{\mathrm{L}}\sin\phi_{\mathrm{T}}+B_{13}\sin\left(\phi_{\mathrm{L}}+\phi_{\mathrm{T}}\right)\right]\\&=\sqrt{\left(\gamma_{\mathrm{us}}-\gamma_{\mathrm{sf}}\right)p\left(\phi_{\mathrm{T}}\right)}\end{aligned} \tag{3-18}$$

where ϕ_{L} and ϕ_{T} are the angles between the crack front and the Burgers vector of the leading and the trailing partial, respectively; b_{L} is the Burgers vector length of the leading partial and r_{L} is the equilibrium position of the leading partial, which can be obtained by the balance of all the forces (applied *K*-field, image force due to the stress-free crack surface, and the force γ_{sf} to annihilate the stacking fault) exerted on it through

$$\frac{b_{\mathrm{L}}}{2\sqrt{2\pi r_{\mathrm{L}}}}=\frac{\left(K_{\mathrm{II}}\cos\phi_{\mathrm{L}}+K_{\mathrm{III}}\sin\phi_{\mathrm{L}}\right)-\sqrt{\left(K_{\mathrm{II}}\cos\phi_{\mathrm{L}}+K_{\mathrm{III}}\sin\phi_{\mathrm{L}}\right)^{2}-\gamma_{\mathrm{sf}}p\left(\phi_{\mathrm{L}}\right)}}{p\left(\phi_{\mathrm{L}}\right)} \tag{3-19}$$

Using the combined stress intensity factor K ($K_{\mathrm{II}}=K\cos\theta$, $K_{\mathrm{III}}=K\sin\theta$) and substituting Eq. (3-19) into Eq. (3-18), the criterion for nucleation of the second partial may be written as

$$K_{\mathrm{T}}^{*}=K\left[\cos\left(\theta-\phi_{\mathrm{T}}\right)-\eta\cos\left(\theta-\phi_{\mathrm{L}}\right)\right]+\eta\sqrt{\cos^{2}\left(\theta-\phi_{\mathrm{L}}\right)K^{2}-\gamma_{\mathrm{sf}}p\left(\phi_{\mathrm{L}}\right)}=\sqrt{\left(\gamma_{\mathrm{us}}-\gamma_{\mathrm{sf}}\right)p\left(\phi_{\mathrm{T}}\right)} \tag{3-20}$$

where

$$\eta=2\left[\mathrm{B}_{11}\cos\phi_{\mathrm{L}}\cos\phi_{\mathrm{T}}+B_{33}\sin\phi_{\mathrm{L}}\sin\phi_{\mathrm{T}}+B_{13}\sin\left(\phi_{\mathrm{L}}+\phi_{\mathrm{T}}\right)\right]/\,p\left(\phi_{\mathrm{L}}\right). \tag{3-21}$$

For most cases, K_{T}^{*} increases as *K* increases, so that when *K* reaches a critical value of $K_{\mathrm{C}}^{\mathrm{T}}$, the criterion is satisfied and then the trailing partial is nucleated. By moving the first

term of Eq. (3-20) to the right side and making both sides squared, the critical value K_C^T can be obtained by solving the quadratic equation

$$\left(a_2^2 - a_1^2\right)K^2 - \left(2C_1 a_2\right)K + \left(C_1^2 + \eta^2 C_2^2\right) = 0 \tag{3-22}$$

where $a_1 = \eta\cos\left(\theta - \phi_L\right)$, $a_2 = \cos\left(\theta - \phi_T\right) - a_1$, $C_1 = \sqrt{\left(\gamma_{us} - \gamma_{sf}\right)p\left(\phi_T\right)}$, and $C_2 = \sqrt{\gamma_{sf}p\left(\phi_L\right)}$. The root of the critical stress intensity factor K_C^T should satisfy two requirements: (1) the term under the square root on the left side in Eq. (3-20) should be positive, i.e., $K_C^T > \sqrt{\gamma_{sf}p\left(\phi_L\right)}/\cos\left(\theta - \phi_L\right)$, which comes from the fact that K_C^T needs to exceed $K_{min}^{L\to T}$ to have a physical meaning and (2) the first term in Eq. (3-20) should be less than the right side due to the positive value of the square root, $a_2 K_C^T < \sqrt{\left(\gamma_{us} - \gamma_{sf}\right)p\left(\phi_L\right)}$. It is also possible that both roots do not satisfy these two requirements or there is no real root, which suggests that for every $K > \sqrt{\gamma_{sf}p\left(\phi_L\right)}/\cos\left(\theta - \phi_L\right)$, the condition $K_T^* > \sqrt{\left(\gamma_{us} - \gamma_{sf}\right)p\left(\phi_T\right)}$ is always satisfied, leading to the case that the trailing partial is simultaneously nucleated after nucleation of the leading partial. Fig. 3-10 plots the numerical results of the critical loading for nucleation of the trailing partial dislocation as a function of shearing angle θ for the leading partial with $\phi = 120°$, together with Rice analytical results based on the constrained path assumption. For the references, the numerical and Rice results of the critical loading for nucleation of the leading partial are also plotted in Fig. 3-10. According to the relationship between K_C^L and K_C^T, the plots in Fig. 3-10 can be divided into several zones: (1) $K_C^T > K_C^L$; (2) $K_C^T < K_C^L$; (3) there is no critical stress for the

nucleation of the trailing partial. Once more, it is interesting to note that even the constrained slip path assumption appears to be increasingly invalid as the shearing direction deviates from the Burgers vector direction, the analytical results based on the constrained path assumption are still reasonably good approximation for nucleation of trailing partials for most configurations. However, for Al, the division of the loading zones for different nucleation mechanisms based on numerical results is quite different from the Rice analysis. This is probably because in Al the closer interaction between the leading and trailing partial causes their configurations to deviate more from the standard dislocation configuration of linear elastic dislocation theory on which Rice analysis is based.

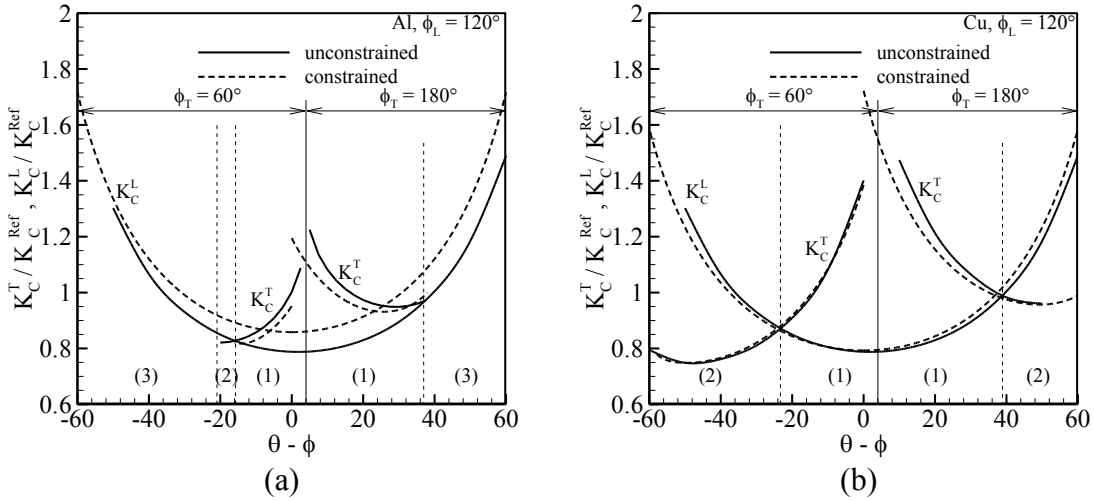

Figure 3-10. Critical loading for nucleation of the trailing partial as a function of loading direction for (a) Al and (b) Cu. According to the relationship between K_C^L and K_C^T, the plots can be divided into three zones: (1) $K_C^T > K_C^L$; (2) $K_C^T < K_C^L$; (3) there is no critical stress for the nucleation of the trailing partial.

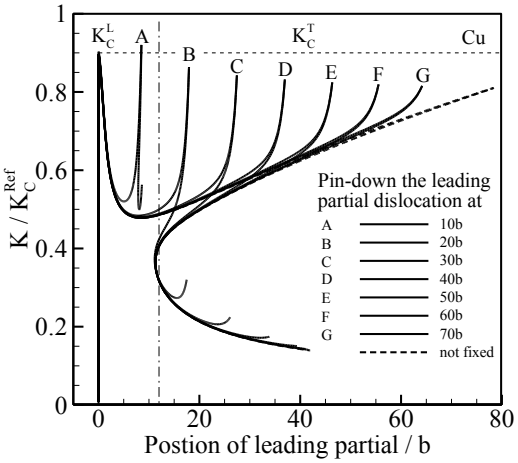

Figure 3-11. The equilibrium loading versus the position of the leading partial pinned down at various distance. The peak values at A, B, …, G represent the critical loading required for nucleation of the trailing partial.

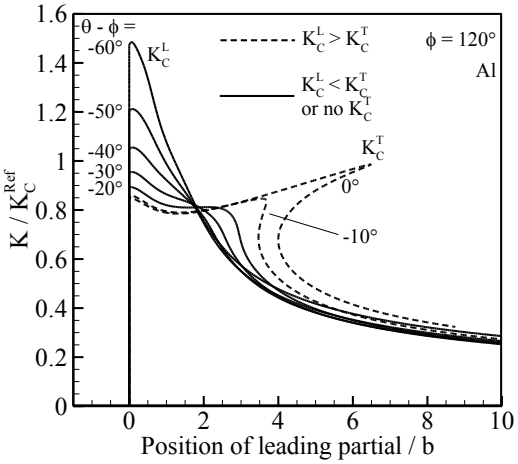

Figure 3-12. The equilibrium loading versus the position of the leading partial for vaious loading directions.

To further reveal how various factors influence nucleation of the trailing partial, we first consider how the position of the leading partial affects the critical loading K_C^T for nucleation of the trailing partial for the considered configuration in Cu. Assume there exists an obstacle in front of the crack to pin down the leading partial. The critical loading for nucleation of the trailing partial K_C^T varies with distance of the obstacle to the crack. The equilibrium loading versus the position of the leading partial for various positions of the obstacle during the nucleation process is plotted in Fig. 3-11. For each curve, the first peak value (note that all the first peaks coincide) represents the critical loading for nucleation of the leading partial while the second peak value represents the critical loading for nucleation of the trailing partial. When the obstacle is located relatively far from the crack, no more additional loading is required for nucleation of the trailing partial because the second peak value is less than the first peak value. Larger than K_C^L loading is required for nucleation of the trailing partial if the leading partial is pinned down by the obstacle at the position closer than about 15 Burgers vectors to the crack. For the configuration we have considered in Al, the position of the leading partial becomes a lesser issue since the trailing partial is nucleated almost immediately after nucleation of the leading partial. Instead, we focus on understanding how the loading direction affects the critical loading K_C^T for nucleation of the trailing partial for $\phi_L = 120°$. Fig. 3-12 plots the equilibrium loading versus the position of the leading partial for various loading directions during the nucleation process. Together with the curves in Fig. 10(a), the results may be summarized as three cases:

(1) $\sim -15° < \theta - \phi <\sim 0°$, $K_C^T > K_C^L$; (2) $\sim -15° < \theta - \phi <\sim -25°$, $K_C^T < K_C^L$; and (3) $-60° < \theta - \phi <\sim -25°$, no critical stress for nucleation of the trailing partial. For case (2) and (3), the trailing partial can be considered to be simultaneously nucleated as the leading partial is being developed. We shall note that for all geometrical and loading conditions there seldom exist large intrinsic stacking faults in Al. The intrinsic stacking fault formed in the nucleation process has a size of about 3*b*, which is similar to the intrinsic stacking fault size of the final dissociated full dislocation in a perfect crystal. By contrast, the intrinsic stacking faults in Cu prevail and have much larger size than the size of the dissociated full dislocation in a perfect crystal.

3.3.3 Activation energy

The difference of the nucleation process in Al and Cu is also reflected in the activation energy required for thermally assisted nucleation. Taking the example configuration of $\theta = 90°$ and $\phi = 120°$, the relative total energy per unit Burgers vector length for different dislocation configurations under various stress levels for Al and Cu, respectively, is plotted in Fig. 3-13(a) and (b). For Al, since the leading and trailing partials are nucleated almost simultaneously and there is only one critical stress as shown in Fig. 3-8(a), the activation energy analysis is similar to that of a single full dislocation. Note that at the stress level near the critical stress, the activation energy is regarded as the activation energy required to activate the leading partial. The trailing partial is formed immediately after the leading partial emanates from the crack. At the relatively low stress level, significant energy is required for nucleation of the fully dissociated dislocation at

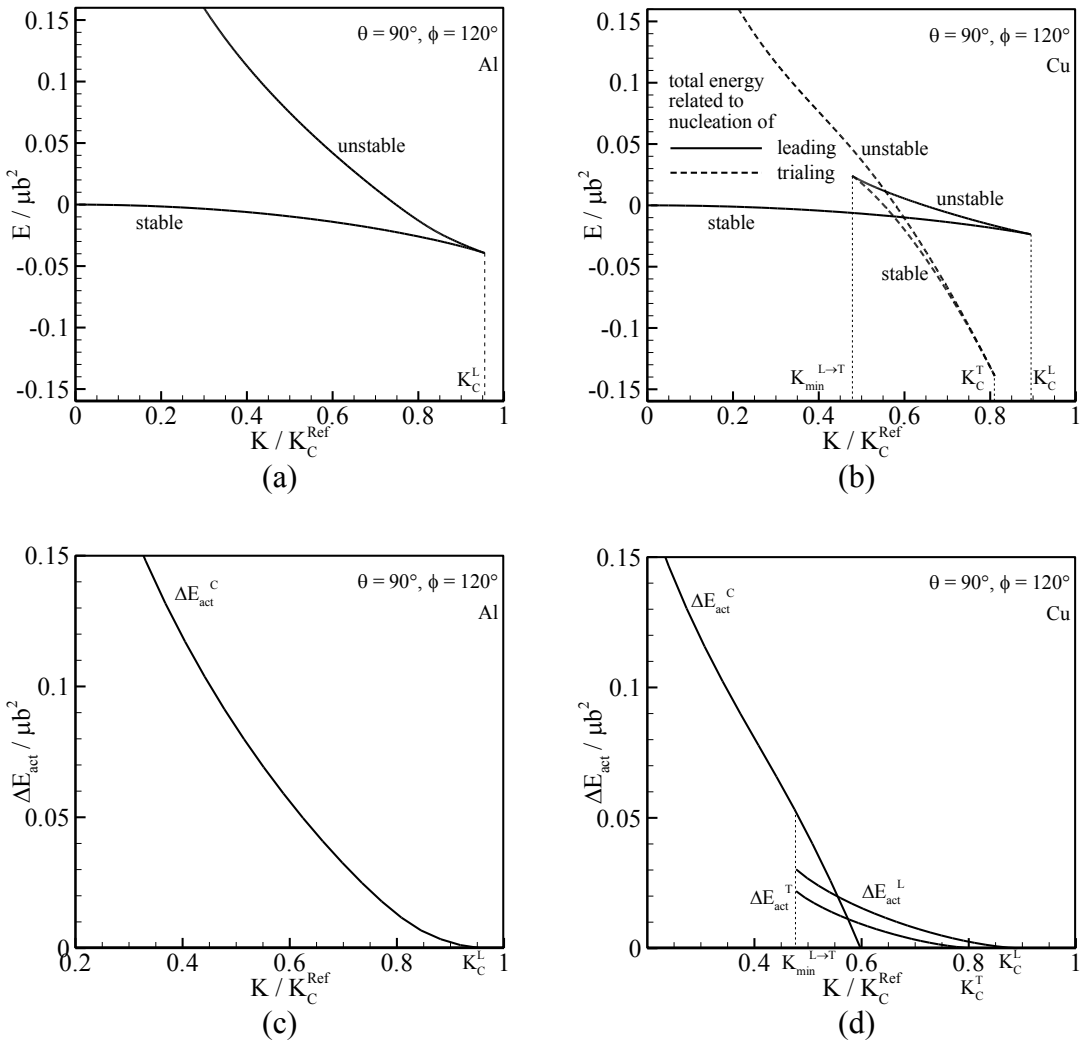

Figure 3-13. Dependence of the total energy and activation energy on loading ($\theta = 90°$, $\phi = 120°$): (a) and (c) Al; (b) and (d) Cu.

the crack. For Cu, the total energy variation is divided into four segments related to the loading process: (1) stable equilibrium loading till the leading partial is nucleated at $K_{\mathrm{C}}^{\mathrm{L}}$, (2) unstable equilibrium loading till the conversion from unstable to stable configuration at loading $K_{\min}^{\mathrm{L}\to\mathrm{T}}$, (3) stable equilibrium loading till the trailing partial is nucleated at $K_{\mathrm{C}}^{\mathrm{T}}$, (4) unstable equilibrium loading as the fully formed dissociated dislocation moves away from the crack. Several activation energies may be identified as shown in Fig. 3-13(d): (1) the energy differences between the unstable and stable configuration for each leading and trailing partial nucleation, marked as $\Delta E_{\mathrm{act}}^{\mathrm{L}}$ and $\Delta E_{\mathrm{act}}^{\mathrm{T}}$; (2) the energy difference between the stable configuration of the leading partial and the final saddle-point configuration of the combined leading and trailing partials, marked as $\Delta E_{\mathrm{act}}^{\mathrm{C}}$. At the loading level between $K_{\mathrm{C}}^{\mathrm{T}}$ and $K_{\mathrm{C}}^{\mathrm{L}}$, $\Delta E_{\mathrm{act}}^{\mathrm{L}}$ is the activation energy required for thermally assisted nucleation of the leading partial. Once the leading partial is nucleated at this loading level, the trailing partial is subsequently nucleated, leading to fully formed dissociated dislocation with a stacking fault as the leading partial moves away from the crack. At the loading level between $K_{\min}^{\mathrm{L}\to\mathrm{T}}$ and $K_{\mathrm{C}}^{\mathrm{L}}$, $\Delta E_{\mathrm{act}}^{\mathrm{L}}$ is still the activation energy required for thermally assisted nucleation of the leading partial first. Once the unstable configuration of the leading partial is formed, it moves naturally to the stable configuration with the incipient trailing partial because the energy of this state is lower than that of the unstable configuration as shown in Fig. 3-13(b). $\Delta E_{\mathrm{act}}^{\mathrm{T}}$ is then the required energy to activate this stable configuration with the leading partial and the stacking fault to the unstable configuration of the full formed dissociated dislocation. Once the dissociated dislocation is fully

formed, it moves away from the crack while the stacking fault eventually shrinks to the normal equilibrium spacing. Finally, at the loading level below $K_{\min}^{L\to T}$, ΔE_{act}^{C} is required for thermally assisted nucleation of the fully formed dissociated dislocation, which in general is an unlikely event because of extremely high energy barrier.

3.4 Nucleation of Curved Partial Dislocations

The above energetic analysis of idealistic nucleation of straight dislocations in the two dimensional configuration provides a good insight on the complex nucleation process of partial dislocations at the crack. The realistic situation is nucleation of a curved dislocation as a consequence of a localized outward protrusion of slip into an unstable saddle-point configuration from the stable configuration. To carry out the analysis of nucleation of curved dislocations, we consider a symmetric configuration of a slit crack of the length $2a$ instead of using the semi-infinite crack configuration. The crack length $2a$ is purposely set to be large enough (e.g., $2000b$) compared to the size of the dislocation nucleation configuration so that the standard K-field characterized by the stress intensity factor K can still be used to characterize the loading. The selection of the slit crack configuration is purely a choice for convenience because it is relatively more direct to carry out the following computation using Eq. (3-1) as compared with the previous selection of a semi-infinite crack for which we need to perform the rather tedious mathematical manipulation in order to reduce the computation on the finite domain (Xu and Ortiz, 1993; Xu, *et al*, 1995). Both treatments lead to the same result as

long as the length of the crack is sufficient larger than the size of the dislocation nucleation configuration. Similar to the previous analysis, the periodic boundary condition is implemented along the crack front direction. The period of the domain is selected to be 100*b* so that it is sufficient to reduce the interaction between the dislocation configurations in each period. Because the dislocation configurations act like a dipole in the crack front direction, the interaction between them drops quickly as the period increases. The geometric angles ϕ and θ defined in Fig. 3-1 are selected as $\theta = 90°$ and $\phi = 120°$ (mode III loading). A tiny perturbation at each side of the domain along the crack front is introduced to naturally activate the saddle point configuration of the curved leading partial ($b = 1/6[\bar{2}11]$) in computation as the loading approaches the critical value. For Al, similar to nucleation of the straight partials, the trailing partial ($b = 1/6[\bar{1}\,\bar{1}\,2]$) is nucleated simultaneously after the leading partial, resulting in a fully dissociated dislocation configuration combined with two partials and an enclosed intrinsic stacking fault. Fig. 3-14(a) shows the typical saddle-point configuration of a curved dissociated dislocation at the crack in Al at the loading level $K = 0.627K_C$, while Fig. 3-14(b) shows a curved leading partial in Cu at the loading level of $K = 0.600K_C$. The contour plots represent two slip components of the partials. For Cu, the stacking fault area is enclosed by the crack front and the leading partial. The profile of the partial is very similar to those perfect dislocations obtained before (Xu, *et al*., 1997), except that there are now two slip components. The elliptical shape of the emitting intrinsic stacking fault is in contrast with the circular shape assumed in the analysis of this problem based on continuum elastic

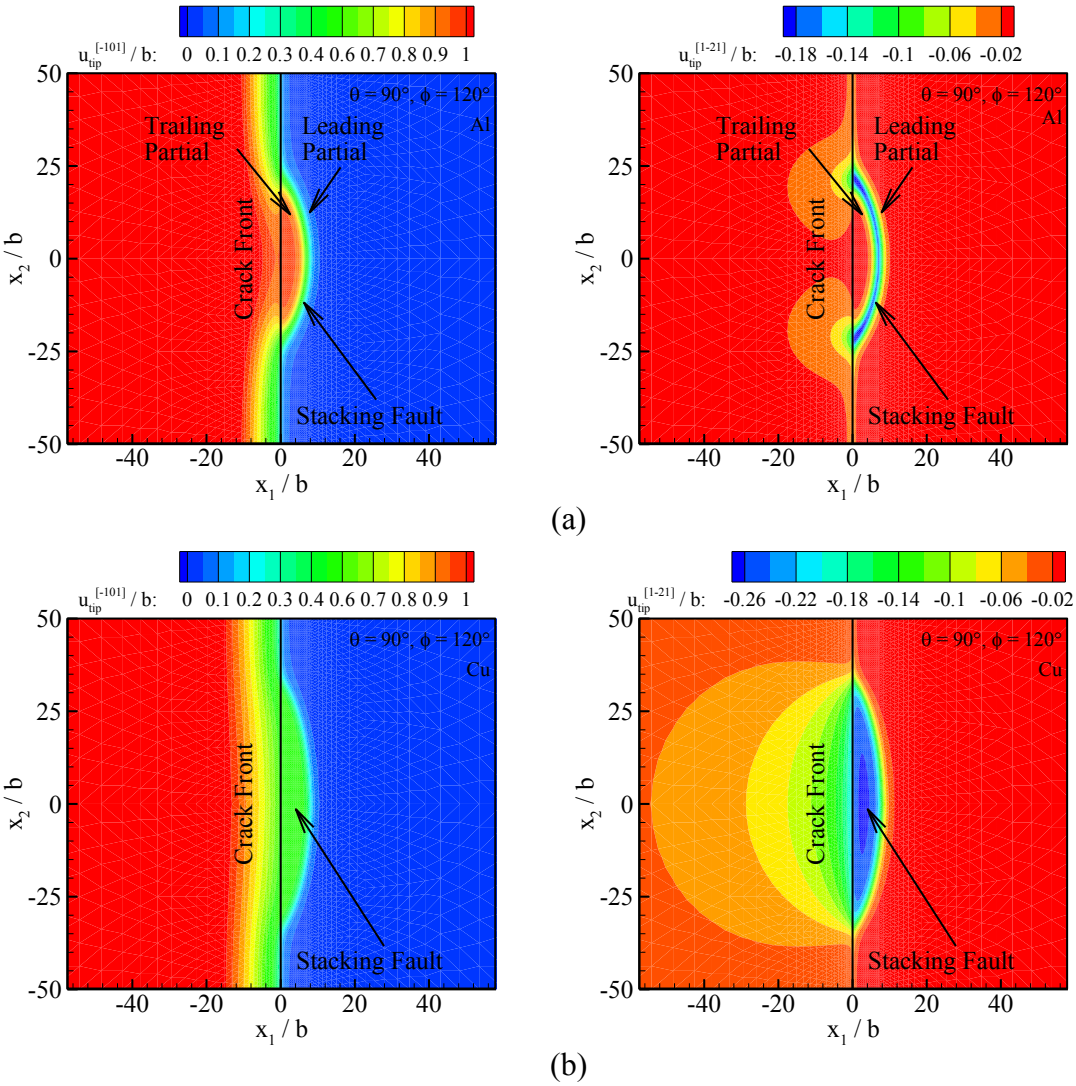

Figure 3-14. Saddle-point configurations of the partial dislocation loops at the crack ($\theta = 90°$, $\phi = 120°$): (a) Al; (b) Cu.

dislocation theory (Asaro and Suresh, 2005). For Al, after the dissociated dislocation is fully formed, the relatively small stacking fault is enclosed by the leading and trailing partials. For given the mesh size, the curved leading partial has to be driven beyond the periodic boundary before the curved trailing partial can be nucleated for Cu. Hence the curved full dissociated dislocation configuration for Cu cannot be obtained because of the limitation of the mesh. Nevertheless, the basic feature that large stacking faults tend to form in Cu before nucleation of the trailing partial obtained in the two dimensional configuration remains intact.

Fig. 3-15 shows the dependence of the activation energy on loading for nucleation of the curved partial dislocations. As a comparison, the dependence of the activation energy on loading for nucleation of the perfect dislocation $b = 1/2[\bar{1}01]$ is also obtained using the constrained path assumption. For Al, the critical loading for nucleation of the partial is considerably lower than for nucleation of the perfect dislocation. At relatively low stress level the activation energy is asymptotically close to that of the full dislocation since the stacking fault area between the two partials are very small and the dissociated dislocation has similar structure to that of the full dislocation. For Cu, we note that both critical loading and activation energy for nucleation of the leading partial are markedly lower than those for the full dislocation. The much lower activation energy for nucleation of the partials may be one of the major sources for the high strain rate sensitivity of nano-grained metals. Unlike coarse-grained metals, where there are abundant dislocation generation mechanisms, there are limited sources for dislocations in nano-grained metals. Nucleation of partial dislocations at the heterogeneities of grain boundaries with high

stress concentration therefore may significantly contribute to mechanical behavior of nano-grained metals.

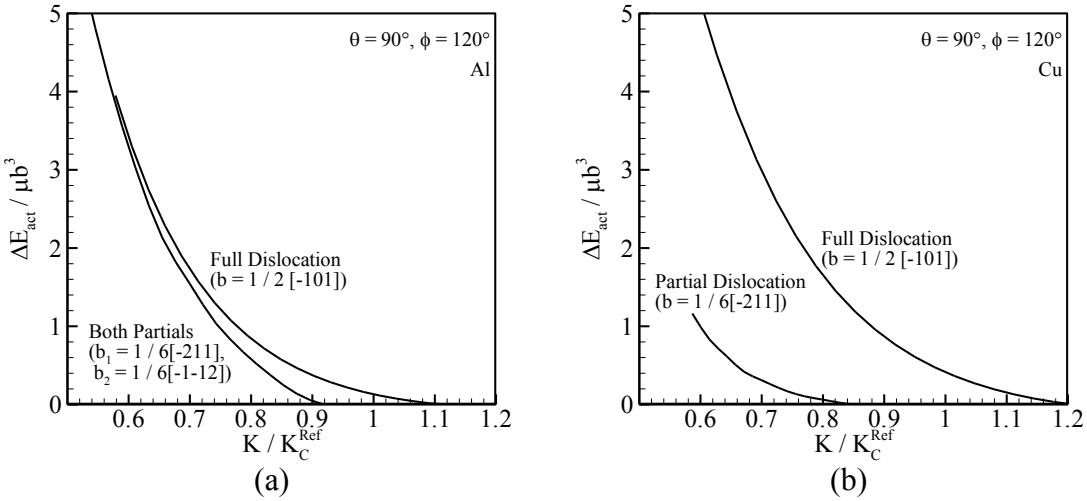

Figure 3-15. Activation energy for nucleation of partial dislocation loops at the crack tip ($\theta = 90°,\ \phi = 120°$): (a) Al; (b) Cu.

3.5 Summary and Conclusion

Nucleation of partial dislocations at a crack is analyzed based on a multiscale model that incorporates atomic information into continuum mechanics approach. The crack and the slip plane as the extension of the crack are modeled as a surface of displacement discontinuities embedded in an elastic medium. The atomic potential between the adjacent atomic layers along the slip plane is assumed to be the generalized stacking fault energy, which is obtained based on atomic calculations. The relative displacements along the slip plane, corresponding to the configurations of partial dislocations and stacking faults, are solved through the variational boundary integral method.

The energetics of partial dislocation nucleation at the crack in Al and Cu are comparatively studied for their distinctive difference in the stacking fault energy. Several new features have emerged compared with nucleation of perfect dislocations in previous studies. Among them, the critical stress and activation energy for nucleation of partial dislocations are significantly lowered. For metals with relatively high stacking fault energy such as Al, nucleation of trailing partials immediately follows nucleation of leading partials, seldom resulting in the formation of large stacking faults in most configurations. For metals with relatively low stacking fault energy such as Cu, nucleation of trailing partials only occurs after leading partials are moved relatively far away from the crack, commonly resulting in the formation of much larger stacking faults compared with the stacking faults in normally dissociated dislocations in perfect crystals. The activation energy for thermally assisted partial dislocation nucleation in Cu is also significantly lower compared with the one for assumed perfect dislocation nucleation.

Our results may have significant implications for identifying the fundamental dislocation and grain boundary mediated deformation mechanisms in nanostructured metals. It has been well recognized that conventional collective dislocation interactive mechanisms become non-operable as the grain size reduces to sub 100 nanometers range. The limiting strength of nanostructured metals could be ultimately determined by the critical condition for partial dislocation nucleation at heterogeneities where large stress concentration exists. Here, we have specifically shown how intrinsic stacking fault energy influences the partial dislocation nucleation process. In general, low stacking fault energy shall facilitate nucleation and motion of partial dislocations. The formation of

large stacking faults across the grains in the metals with low stacking fault energy, however, may hinder dislocation nucleation and motion in other slip systems. Further studies are necessary for better understanding the combined effect. The much lower activation energy for partial dislocation nucleation in the metals with relatively low stacking fault energy could be the major source of high strain rate sensitivity in nano-grained metals, although the concrete conclusion of this link also requires further analyses and experiments to delineate how the energetics of dislocation nucleation in various configurations collectively influence overall mechanical behavior of metals. On the other hand, for certain well defined nanoscale material structures such as thin film systems or nano-sized pillars, where dislocation nucleation configurations are relatively certain (Weigner, 1999; Gao, et al, 1999; Buehler, et al, 2003; Uchic, et al., 2004; Greer, et al, 2005), the link between partial dislocation nucleation and mechanical behavior of the structures can be probably more readily identified by directly comparing experiments with analyses.

Chapter 4 Cross Slip of Partial Dislocations

4.1 Introduction

Plastic deformation of crystals proceeds with not only the nucleation of dislocations but also the motion of dislocations. When a dislocation moves along a slip plane which is not necessarily the most favorable one in terms of local stress, it can move to the other one through cross-slip. This phenomenon has long been recognized as the most single important mechanism that accounts for the development of complex dislocation microstructure leading to pattern formation, strain hardening, and dynamic recovery (Puschl, 2002). Previous experimental and theoretical studies have indicated that cross-slip is a rate controlling process which depends on temperature as well as stress (Bonneville, Escaig, Martin, 1988). Because cross-slip mechanisms are generally versatile, and controlled by a wide range of atomic parameters, the critical conditions for cross-slip for most crystals largely remain uncertain. As a consequence, their influence on plastic deformation, especially at the later hardening stages, still cannot be quantitatively characterized with certainty.

A number of possible cross-slip configurations have been proposed in the past (Puschl, 2002; Hirth and Lothe 1982). Here we shall focus on the most common cross-slip mechanism found in FCC metals as shown in Fig. 4-1. In FCC metals, a screw dislocation normally dissociates into two Schockley partials bonding an intrinsic stacking

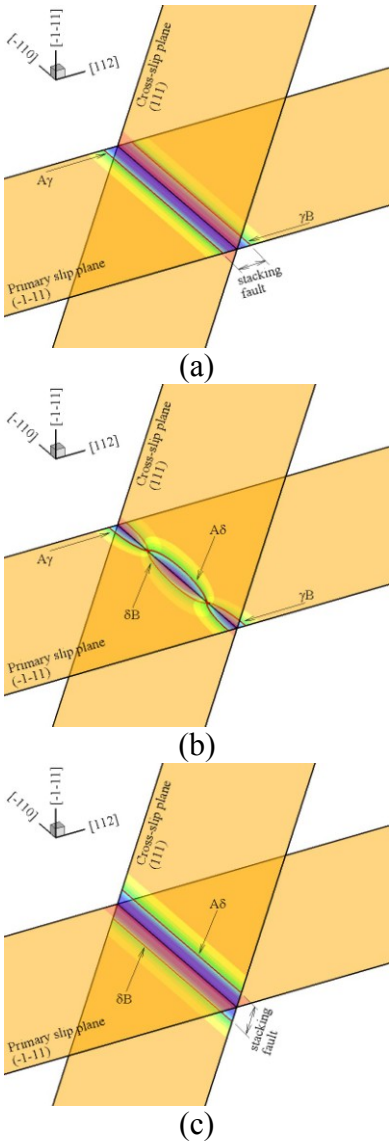

Figure 4-1. Illustration of the physical process of the Friedel-Escaig (FE) cross-slip mechanism of a screw dislocation in a FCC crystal: (a) the dislocation dissociates into two partial dislocation (γB and Aγ) on $(\bar{1}\,\bar{1}\,1)$ plane; (b) the dislocation re-dissociates into two partials (δB and Aδ) on (111) plane; (c) the dislocation finally cross-slips on (111) plane.

fault on the preferred {111} slip plane. When the dislocation is under external stress, the resolved shear stress along the edge components of the partial dislocations, defined as the Escaig stress, exerts equal but opposite forces on the two partials. When the Escaig stress compresses the stacking fault ribbon, the compressed portion of the dislocation may then bow out into the other {111} slip plane and re-dissociate. The bowing-out and re-dissociating process can simultaneously occur in FCC metals and in some cases complete constriction does not appear to be necessary (Duesbery, 1998). This mechanism, first suggested by Friedel (1959), and later developed by Escaig (1968), has been identified through the experimental studies as a favored cross-slip mechanism (Bonneville, Escaig, Martin, 1988). A somewhat similar mechanism had also been envisioned by Fleischer (1959). It differs from Friedel-Escaig mechanism by suggesting that no complete constriction of the stacking fault ribbon should be necessary. Instead, the stacking fault folds over continuously from the primary slip plane into the cross-slip plane. At the intersection the geometric compatibility requires that the leading partial dislocation splits into a stationary stair rod dislocation and a Shockley partial in the cross-slip plane. An analysis taking into account of dislocation characters and line energies showed that in the overwhelming majority of cases it is much more expensive to generate the additional stair rod dislocation than to completely constrict the stacking fault (Puschl, 2002). Therefore, we mainly focus on the Friedel-Escaig cross-slip mechanism.

Up to date three analytical approaches have been used for the study of the Friedel-Escaig cross-slip mechanism (Puschl, 2002). The first is based on the line tension approximation (Friedel, 1959; Escaig, 1968). Because this approach completely ignores

atomic interactions, it is not considered to be reliable in treating the constriction process. The second approach is based on large scale atomistic simulation (Rasmussen, *et al*., 1997; Rao, *et al*, 1999; Wen, *et al*, 2004), which can be directly used to determine the cross-slip process path. The success of this method relies on suitable selection of interatomic potentials that can accurately reproduce some important second order effects such as stacking fault energy. It is generally difficult to incorporate the precise elastic far field so to determine the stress dependent activation energy for appropriate saddle point configurations for large atomic systems. The third approach is the linear elastic mechanics approach with the incorporation of the appropriate dislocation core model to account for nonlinear local interaction. This type of model is generally based on the Peierls-Nabarro framework in which the structure of a dislocation is modeled as the relative displacement between two adjacent atomic layers along the slip plane and the surrounding crystals as the linear elastic continuum. The continuum mechanics based boundary integral formulation allows for convenient incorporation of various types of interatomic layer potentials to account for the local non-linear effect. The generalized stacking fault energy, or the so called γ-surface (Vitek, 1968), obtained by atomistic simulation such as *ab initio* calculation or embedded atom method (EAM), is regarded as the best choice for its fidelity to the properties between interatomic planes. Although this method is not as direct as atomic simulation in terms of determining the cross-slip process path, its continuum mechanics based approach possesses advantages in obtaining the stress-dependent saddle-point configurations and the associated activation energies under precisely described external loading conditions. As a complement to the atomic

simulation, this method has proved to be a valuable tool in probing the activation parameters in many dislocation mechanisms (e.g., Xu, Zhang, 2003; Segall, Li Xu, 2006; Li, Xu, 2006).

Lu, *et al*. (2002, 2004) studied the cross-slip using the third approach by assuming the dislocation remain to be straight during the cross slip. They found that cross-slip in metal such as Al with high intrinsic stacking fault energy γ_{sf} and thus narrow intrinsic stacking fault ribbon occurs spontaneously, while for metal such as Ag with lower γ_{sf} the dislocation splits into partials and cannot cross-slip without being first constricted. Since the analysis based on the straight dislocation model can provide good insights in the critical stresses for the onset of cross slip, we also begin with the study of cross-slip by assuming the dislocation remains to be straight. Two metals Al and Cu are selected for their significant difference in intrinsic stacking fault energy. In addition to the work of Lu (2002, 2004) where only the Escaig stress on the primary slip plane is considered, cross-slip under general loading is further studied. As a consequence, the Escaig stress is applied on both the primary slip plane and the cross-slip plane. The effects of the loading direction and the ratio of the shear stresses on both slip planes on the cross-slip are ascertained. Moreover, using the fully three-dimensional boundary integral formulation (Xu and Ortiz, 1993; Xu, Zhang, 2003; Segall, Li Xu, 2006; Li, Xu, 2006), we extend the analysis to the more realistic dislocation cross-slip process in which the dislocation does not remain straight but rather bows out on both primary and cross slip planes so to take minimum energy path. Our focus is to identify the critical energetic condition for the

occurrence of cross-slip, with the emphasis placed on the effect of the intrinsic stacking fault energy on cross-slip behavior in FCC metals.

4.2 Modeling

Consider a configuration of two slip planes $(\bar{1}\,\bar{1}\,1)$ and (111) intersecting along the line in the $[\bar{1}\,10]$ direction, as shown in Fig. 4-2. The screw dislocation with a Burgers vector of $1/2[\bar{1}\,10]$ can glide on both slip planes, and it is also possible for this crew dislocation to dissociate into two Shockley partial dislocations on both planes. The crystalline indices of the slip systems are summarized with the Thompson notation in Table 4-1. All displacement discontinuities are described in the local coordinate systems (*oxyz*) instead of the global coordinate systems (OXYZ) for their clarity in physical meanings. The origins of the local coordinators are located at the intersection. Note that the positive directions for the screw components on both slip planes are opposite, along AB direction for the slip plane (1) and along BA direction for the slip plane (2), respectively.

Table 4-1. Slip systems of the dislocation cross slip

	Slip plane **n**	Full dislocation **b**	Leading partial $\mathbf{b}_1$	Trailing partial $\mathbf{b}_2$
Slip plane (1)	(c) $(\bar{1}\,\bar{1}\,1)$	AB $1/2[\bar{1}\,10]$	γB $1/6[\bar{1}\,21]$	Aγ $1/6[\bar{2}1\,\bar{1}]$
Slip plane (2)	(d) (111)	AB $1/2[\bar{1}\,10]$	δB $1/6[\bar{2}11]$	Aδ $1/6[\bar{1}2\,\bar{1}]$

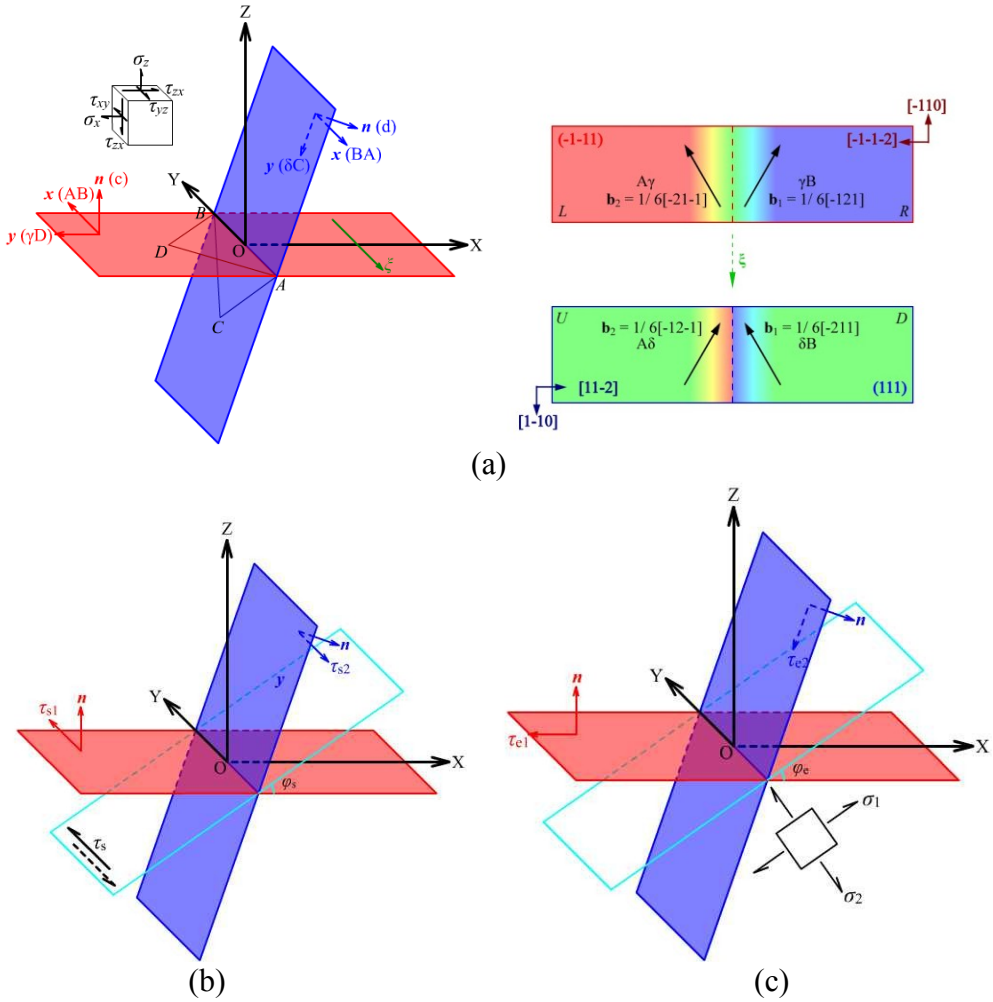

Figure 4-2. Geometric and loading configuration of the cross-slip. Two slip planes $(\bar{1}\,\bar{1}\,1)$ and (111) intersect at the line $[\bar{1}\,10]$.

For a general external loading represented by a stress tensor σ_{ij} in global coordinates, five components τ_{xy}, τ_{yz} and σ_x, σ_y, τ_{zx} may result in resolved shear stresses on the two slip planes. The first two components τ_{xy} and τ_{yz} result in resolved shear stress (τ_{s1} or τ_{s2}) along the screw-components direction on each plane, producing Peach-Köhler forces only on the screw components of the partial dislocations which drive

the dislocation to glide into or away from the intersection of the two slip planes. The components σ_x, σ_y, and τ_{zx} result in the resolved shear stresses (τ_{e1} or τ_{e2}) along the edge-components direction, also called the Escaig stress, producing Peach-Köhler forces only on the edge components to change the area of the intrinsic stacking fault area between two Shockley partial dislocations. Although the components σ_x, σ_y, and τ_{zx} also result in normal stress across each slip plane, the effect of the resolved normal stress is generally negligible because of its relative weak influence on the opening displacements and the γ-surface. Based on the different effects of these two groups of stress components, we propose two independent elementary loading modes: (1) pure gliding shearing stress τ_s on the plane with the tilt angle φ_s to the XY plane as shown in Fig. 4-2(b); (2) loading on the XZ plane characterized by the principle stresses (σ_1, σ_2) with an angle φ_e between the principle direction and the X-direction as shown in Fig. 4-2(c). Let $\tau_e = (\sigma_2 - \sigma_1)/2$, representing the maximum resolved shear stress. The resolved shear stresses on the slip plane (1) can then be expressed as $\tau_{s1} = \tau_s \cos\varphi_s$, $\tau_{e1} = \tau_e \sin 2\varphi_e$ and on the slip plane (2) $\tau_{s2} = \tau_s \cos(\alpha - \varphi_s)$, $\tau_{e2} = \tau_e \sin 2(\alpha - \varphi_e)$, where $\alpha = 70.53°$ is the angle between two slip planes. The ratios of the resolved glide shear stresses and the ratio of the Escaig stresses on both slip planes can be expressed as

$$k_s = \tau_{s1}/\tau_{s2} = \frac{\cos\varphi_s}{\cos(\alpha - \varphi_s)} \text{ and } k_e = \tau_{e1}/\tau_{e2} = \frac{\sin 2\varphi_e}{\sin 2(\alpha - \varphi_e)} \quad (4\text{-}1)$$

In this way, the general external loading is characterized by four parameters τ_s, k_s, τ_e, and k_e, where τ_s and τ_e represent the loading magnitude, and k_s and k_e represent the

loading direction. The parameters τ_s and τ_e distinctly account for the loading effects on screw and edge components of the partial dislocations.

Following the methodology described in Chapter 2, let $\mathbf{u}(\mathbf{x})$ denote displacement discontinuities along both slip planes. The total energy of the system can be expressed by

$$\Pi[\mathbf{u}(\mathbf{x})] = W[\mathbf{u}(\mathbf{x})] + V[\mathbf{u}(\mathbf{x})] - P[\mathbf{u}(\mathbf{x})] \tag{4-2}$$

where W is the elastic strain energy caused by the displacement discontinuities, V is the interatomic layer potential energy, and P is the work of the external force. The expression for these three terms can be referred to Eq. (2-3), Eq. (2-13) and Eq. (2-14) in Chapter 2. The minimization of the total energy $\Pi[\mathbf{u}(\mathbf{x})]$ with respect to the displacement $\mathbf{u}(\mathbf{x})$ leads to nonlinear integral equations. The displacements are discretized through the standard finite elements. The resulting nonlinear equations are solved by Newton-Raphson iterations. The saddle-point configurations of dislocations in the nucleation process are solved by recourse to displacement control through the Lagrange multiplier method. For the convenience of the presentation, the screw or edge components of partial dislocations are denoted as u_{s1}, u_{s2} or u_{e1}, u_{e2} respectively. Because of the continuity, the relative displacements at the intersection must also satisfy the additional constraints

$$u_{s1}(0^+) - u_{s1}(0^-) - u_{s2}(0^+) + u_{s2}(0^-) = 0,\ u_{e1}(0^+) = u_{e1}(0^-) \text{ and } u_{e2}(0^+) = u_{e2}(0^-) \tag{4-3}$$

These constraints are enforced through Lagrange multiplier method.

4.3 Cross-slip of Straight Dislocations

4.3.1 Cross-slip of a straight dislocation in Al

We begin the analysis by introducing a screw dislocation at the intersection on the primary slip plane (1), specified by setting $u_{s1}\left(y_1 \geq 0^+\right) = b$ and other displacement discontinuities including those on the cross-slip plane to be 0. The configuration is then relaxed to minimize the total potential energy under no external loading. The core of the dislocation is found to spread out on both the primary and cross-slip plane. Its profile is plotted in Fig. 4-3, as compared with a screw dislocation profile with a planar core obtained by enforcing no displacement discontinuity on the cross-slip plane (2). Note that the vertical origin for the screw component on the upper-right part of the cross-slip plane (2) is translated up by a distance of b in order not to overlap with the plot of the edge component. The corresponding tick labels are listed at the upper-right corner. For the screw dislocation with the non-planar core, Fig. 4-3 shows that the screw components exist on both slip planes equivalently. The edge components, on the other hand, are not fully developed, indicating the nascent intrinsic stacking fault. Table 4-2 shows that the total energy of the non-planar core structure is lower than the planar core structure, confirming that the core of the screw dislocation in Al is most likely to spread out into two slip planes rather than one slip plane (Lu, *et al*., 2002; 2004).

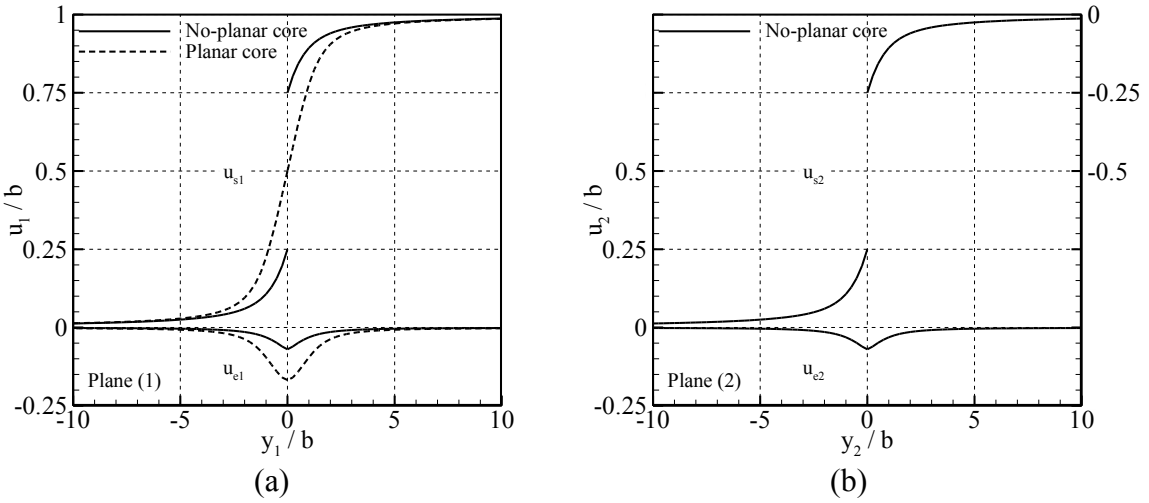

Figure 4-3. The core of a screw dislocation in Al tends to spontaneously spread out into two slip planes. The figure shows two relative displacement components on (a) primary slip plane, (b) cross-slip plane, as compared with no-planar core structure. The vertical original plotting point for the screw components on the right part of the cross-slip plane (2) is moved up by a distance of b in order not to overlap with the edge components, and the tick labels for them are listed at the upper right corner accordingly.

Table 4-2. Total energy comparison between planar and non-planer core in Al

(μb^2)	E_{Elastic}	$E_{\text{Interatomic}}$	E_{Total}	ΔE_{Total}
Planar core	–0.0705426	0.0792767	0.0372220	–0.0288
Non-planar core	–0.0420547	0.0789694	0.0084268	

We then consider the impacts of the external loading on the cross-slip of the screw dislocation with the spread-out core. The loading is characterized by four independent parameters τ_s, k_s, τ_e and k_e. During the simulation, each individual loading is simplified with constant k_s and k_e, which represents only the loading magnitude changes with constant loading direction. Thus the discussion about the simulation results will be based on the various $[\tau_s, \tau_e]$ conditions.

4.3.1.1 *Effects of the pure glide shear stress* (τ_s)

Without the Escaig stress ($\tau_e = 0$), the screw dislocation at the intersection can glide onto both slip planes under the glide shear stress τ_s. Two Peach-Köhler forces on the crew dislocation are resulted from the glide stress components $\tau_{s1} = \tau_s \cos\varphi_s$ on the slip

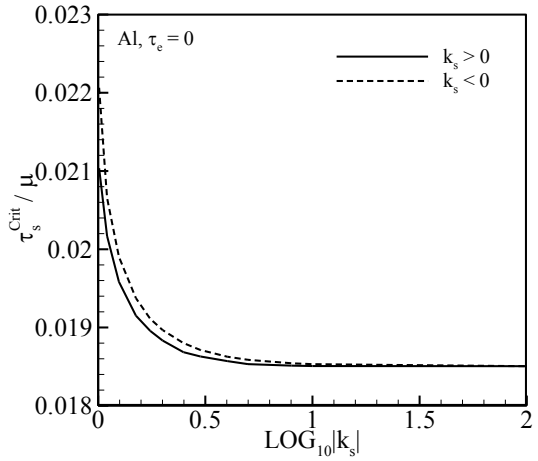

Figure 4-4. The critical glide shear stress (τ_s^{Crit}) is a function of the ratio of the resolved glide shear stress on each slip plane (k_s).

plane (1) and $\tau_{s2} = \tau_s \cos(\alpha - \varphi_s)$ on the slip plane (2). The Peach-Köhler force resulting from τ_{s1} drives the screw dislocation to glide on the slip plane (1), while τ_{s2} drives to glide on the slip plane (2). The preference of the gliding plane depends on the competition between the two resolved shear stresses on the slip planes, which can be characterized by parameter k_s. In the case of dominant τ_{s1}, the screw dislocation glides on the plane (1) when τ_{s1} reaches a critical value τ_{s1}^{Crit} which is a function of k_s due to the interference of τ_{s2}, as shown in Fig. 4-4. Note that the dashed line does not coincide with the solid line because they represent different shear angle φ_s even if $|k_s|$ are the same. On the contrary when τ_{s2} is dominant, the screw dislocation glides on the plane (2) when τ_{s2} reaches a critical value τ_{s2}^{Crit}. Note that $\tau_{s2}^{Crit}(k_s) = \tau_{s1}^{Crit}(1/k_s)$, because of the rotational symmetry of the slip system and the spread-out core structure. The value of the critical glide stresses ranges from 0.018μ or 0.54GPa to 0.022μ or 0.65GPa depending on the shear loading angle characterized by k_s. The shear modulus μ used as the normalization unit here is the Voigt averages

$$\mu = C_{44} - h/5 \text{ and } h = 2C_{44} + C_{12} - C_{11}. \quad (4\text{-}4)$$

It is as the same order to the value of 0.32GPa reported in Lu, *et al*. (2002, 2004) for pure shear on one slip plane, , as well as to the Peierls stress value of 0.008μ in the experiment (Bujard, *et al*., 1987). Assuming that the glide of the screw dislocation from the non-planar core need a transition to planar core similarly as in the bcc metals (Li, Wang, *et al*., 2004), which shares the same type of non-planar core structure, the energy of a planar core structure then represents the energy barrier for a screw dislocation with the spread-

out core structure to complete the gliding process. As a consequence, the maximum activation energy for screw dislocation gliding and the corresponding cross-slip is the core energy variation between the non-planar structure and planar structure, i.e., $0.0288\mu b^2$ or 0.118eV/b. Multiplying this value by $20b$, the typical bow-out width in three dimensional configuration (Xu, Ortiz, Argon, 1997; Xu and Zhang, 2004; Li and Xu, 2006), gives the activation energy about 2eV, indicating that slip process may be a rate process, especially aided with stress.

4.3.1.2 *Effects of the pure Escaig stress* (τ_e)

In the case when only Escaig stress τ_e is applied, the resolved Escaig stress is $\tau_{e1} = \tau_e \sin 2\varphi_e$ on the primary slip plane (1) and $\tau_{e2} = \tau_e \sin 2(\alpha - \varphi_e)$ on the cross-slip plane (2). If the Escaig stress only appears on plane (1) with $\tau_{e2} = 0$, as considered in Lu, *et al*. (2002, 2004), negative Escaig stresses τ_{e1} stretches the edge components of the partial dislocations and enlarges the intrinsic stacking fault area between the two partial dislocations on the primary slip plane (1), as shown in Fig. 4-5(a). Note that the sign definition of Escaig stresses here is contrary to Lu, *et al*. (2002, 2004). By contrast as shown in Fig. 4-5(b), positive Escaig stress τ_{e1} compresses the edge components and shrinks the intrinsic stacking fault area. The screw components on cross-slip plane (2) become larger because u_{s1} on the slip plane (1) is squeezed. Under general loading, the spread-out core structure of the screw dislocation is influenced by the ratios of the two Escaig stresses (k_e). For the positive k_e, the Escaig stresses on both slip planes stretches

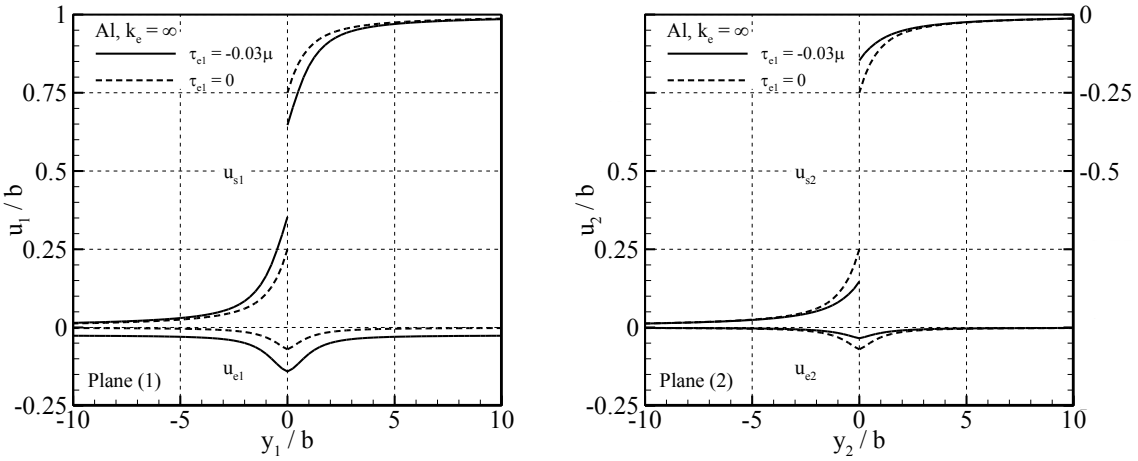

(a)

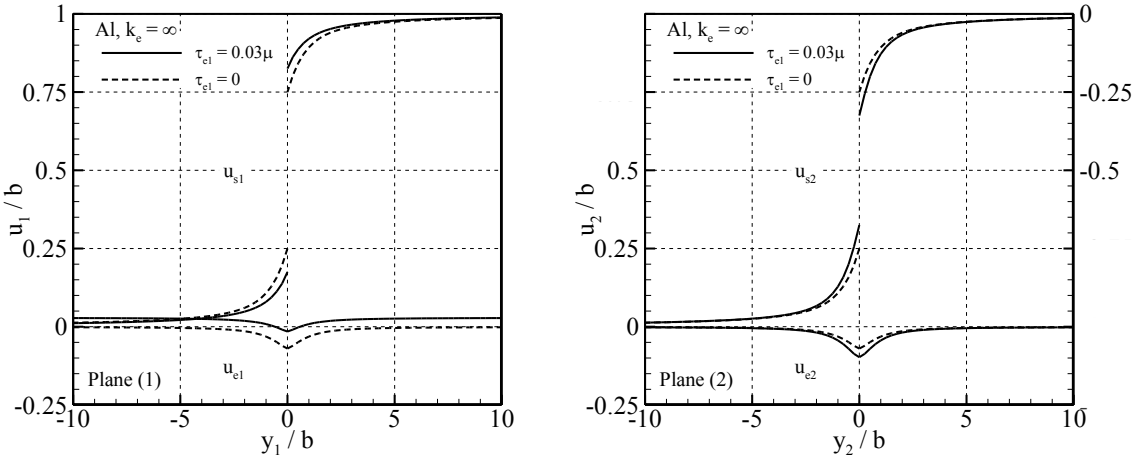

(b)

Figure 4-5. In Al, Escaig stress (τ_{e1}) can break the four-fold symmetry of the balanced screw dislocation with no-planar core and further influnce the critcial glide shear stress (τ_s^{Crit}). The screw and edge components are both plotted on the primary slip plane (left) and the cross-slip plane (right). Figure (a) and (b) show how the oposite Escaig stresses change the dislocation core structure on both slip planes.

or compresses the edge components simultaneously. Since the screw dislocation cannot be spread onto both slip planes, the preferred spread-out plane is determined by the competition between the two Escaig stresses. According to our calculation: (i) in the case of larger stretching Escaig stresses on the primary slip plane (1) or larger compressing Escaig stresses on the cross-slip plane (2), the screw dislocation is maintained on the primary slip plane (1) as shown in Fig. 4-5(a); (ii) in the case of compressing Escaig stresses on the primary slip plane (1) or larger stretching Escaig stresses on the cross-slip plane (2), the screw dislocation spreads onto the cross-slip plane, regarded as the occurrence of cross-slip (Fig. 4-5(b)); (iii) In the case of negative ratio of k_e, the influence of each Escaig stress is complementary to each other. With the stretching Escaig stress on one plane and the compressing Escaig stress on the other, the preferred slip plane is always the one applied by the negative Escaig stress.

4.3.1.3 *Effects of the Escaig stress on the critical glide shear stress*

Under the Escaig stress, the core of the screw dislocation becomes more planar on either the primary slip plane (1) or the cross-slip plane (2), depending on the value of k_e. As a consequence, the critical glide shear stress to move the screw dislocation away from the intersection on the preferred plane decreases. For the case with no resolved Escaig stress on the cross-slip plane (2), the critical glide shear stress (τ_s^{Crit}) as a function of the Escaig stress (τ_{e1}) on the primary plane is plotted in Fig. 4-6. The results show that the critical glide shear resistance can be significantly reduced by the stretching Escaig stress. The cross-slip of the screw dislocation may occur when the resistance for gliding a screw

dislocation on the cross-slip plane becomes lower than the primary slip plane. This can be achieved under a loading condition resulting in either (i) the resolved glide shear stress on the cross-slip plane exceeds the primary slip plane, or (ii) the resolved Escaig stress ratio causes the core of the screw dislocation to spread out more preferably on the cross-slip plane.

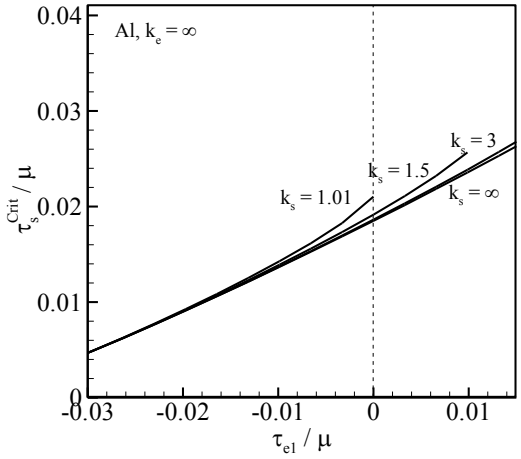

Figure 4-6. The critical glide shear stress (τ_s^{Crit}) is also a function of the Escaig stress (τ_{e1}) on the glide plane. Stretching Escaig Stress decreases the critical glide shear stress on the slip plane.

4.3.1.4 *Critical conditions for cross slip under combined τ_s and τ_e loading*

Under the general loading condition, we assume all the components in the external stress tensor vary proportionally during loading. As a consequence, the shear stresses τ_s and τ_e also increase or decrease proportionally. Define $\tau^2 = \tau_s^2 + \tau_e^2$ and $\tan\theta = \tau_s / \tau_e$. Thus it gives $\tau_s = \tau \sin\theta$ and $\tau_e = \tau \cos\theta$. Note that the physical meaning of τ and θ is clear if the glide shear stress τ_s is coplanar with τ_e (e.g. $\varphi_s = \varphi_e + 45°$) in which τ is

regarded as the resultant of τ_s and τ_e while θ is the angle between them. In simulation, the screw dislocation is initially introduced at the intersection and relaxed to the equilibrium state with non-planar core structure. The combined stress τ is then increased from zero to drive the dislocation to glide on the four slip plane branches. For given k_s and k_e, the dislocation eventually only glide on two of the four branches and the choice of the two possible branches depends on the stress state. The possible gliding branches can be either from different slip planes, indicating occurrence of cross-slip (e.g. $k_s = 3$, $k_e = 1/3$ as shown in Fig. 4-7a), or co-planar, indicating that no cross-slip (e.g. $k_s = 3$, $k_e = 9/7$ as shown in Fig. 4-7b). Detailed characterization appears to be tedious. The essential features is then demonstrated in Fig. 4-8 which maps out the critical k_s, k_e conditions for cross-slip for the case of $\theta = 45°$. In Fig. 4-8, L denotes that the screw dislocation can glide on the branch $y_1 > 0$, R the branch $y_1 < 0$, D the branch $y_2 > 0$, and U the branch $y_2 < 0$. So the green zone denoted by either $\mathrm{L} \leftrightarrow \mathrm{R}$ or $\mathrm{U} \leftrightarrow \mathrm{D}$ represents the k_s, k_e conditions for no cross-slip while the other zone represents the occurrence of cross-slip along with the possible gliding slip planes. The contour plot levels in Fig. 4-8 represent the critical glide shear stress for the cross-slip. It indicates that the cross-slip for this particular case can only happen when the glide shear stresses on both slip planes are comparable. Although k_e is less important than k_s in determining the preference of the slip plane, it still significantly influence the critical shear stress required for cross-slip to occur.

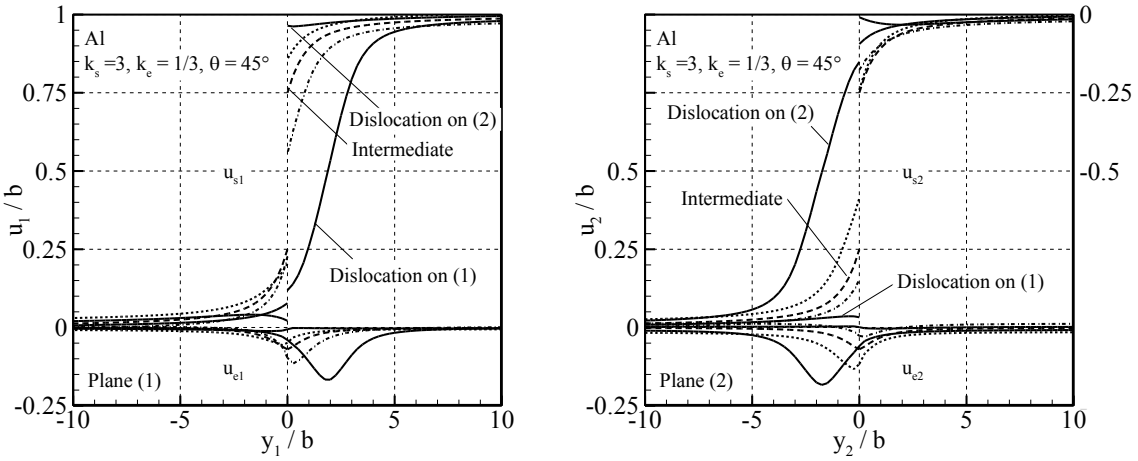

(a)

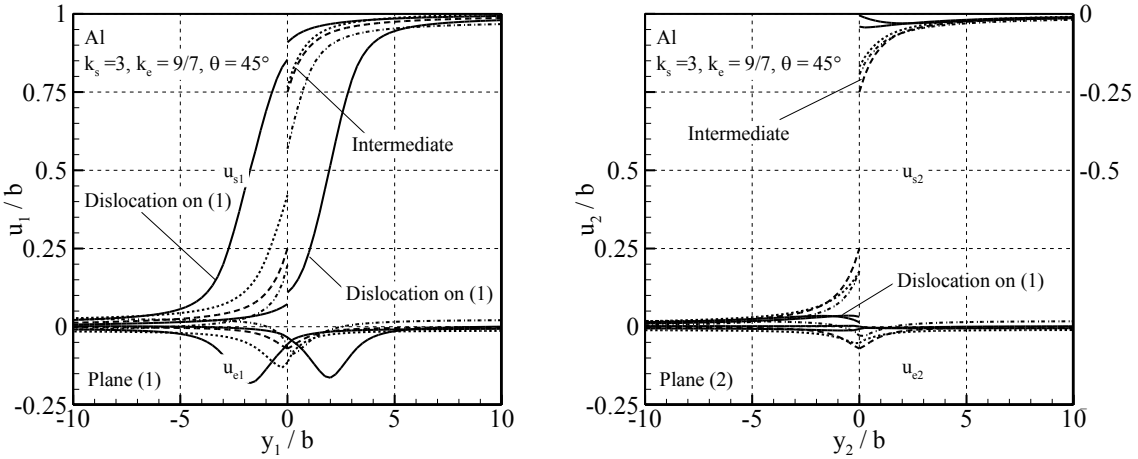

(b)

Figure 4-7. Depending ton the loading, the screw dislocation can glide on two of the four slip branches at the intersection. (a) Dislocation glides on two different slip-planes, and cross-slip occurs. (b) Dislocation glides on one slip plane and no cross-slip occurs.

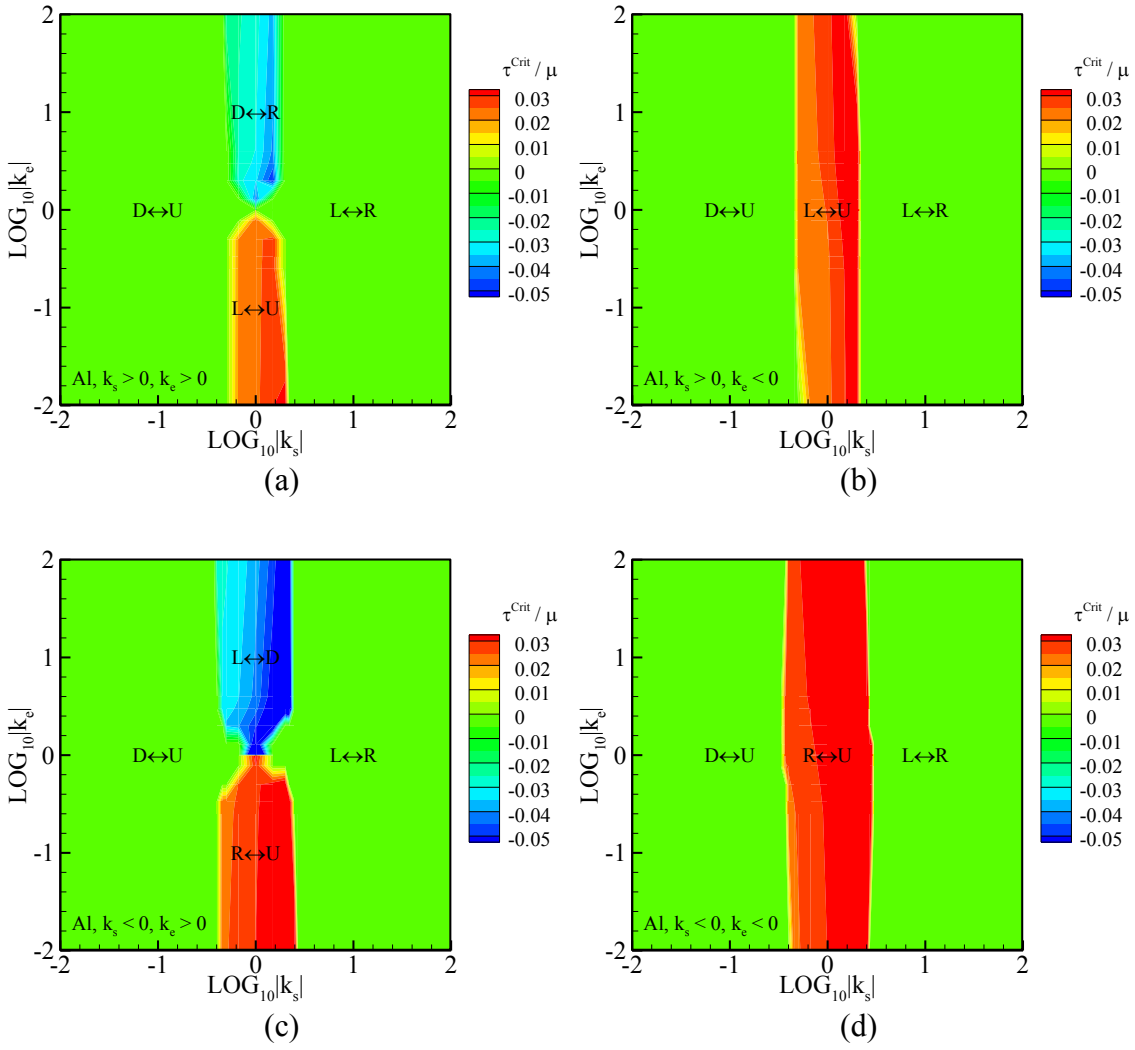

Figure 4-8. The possible glide branches for various loading conditions presented by [k_s, k_e]. In the figure, L denotes that the screw dislocation can glide on the branch $y_1 > 0$; R denotes the branch $y_1 < 0$; D denotes the branch $y_2 > 0$; U denotes the branch $y_2 < 0$. Only the contour level of critical combined external loading stress is plotted for the case when cross-slip occurs.

4.3.2 Cross-slip of a straight dislocation in Cu

In contrast with Al, the stacking fault energy for Cu is relatively lower which results in wider intrinsic stacking fault. The screw dislocation in Cu may have two possible equilibrium core structures, which can be obtained by relaxing from two different initial configurations. By introducing a non-dissociated full screw dislocation at the intersection of the two slip planes, specified by setting $u_{s1}\left(y_2 \geq 0^+\right) = b$ and other displacement discontinuities to be 0, a constricted core structure can be obtained after relaxation. Or in another way, the initial configuration is selected to be a dissociated screw dislocation, specified by a complete idealistic intrinsic stacking fault with the width ($2L$) estimated by elastic theory (Hirth and Lothe, 1982). Setting $u_{s1}\left(y_1 \geq L\right) = b$, $u_{s1}\left(-L < y_1 < L\right) = b/2$, $u_{e1}\left(-L < y_1 < L\right) = -\sqrt{3}b/6$ and other displacement discontinuities to be 0, the relaxation leads to an dissociated quasi-planar core structure. Fig. 4-9 shows the profiles of these two core structures. The corresponding total energy of these two core structures are listed in Table 4-3. Again the pure planar core structure is used as a reference for comparison. The quasi-planar core structure appears to be the most stable configuration due to its lowest total energy. The constricted core structure is similar to the core structure in Al. It can be regarded as the intermediate state during cross-slip. The formation of the constriction needs to overcome the large intrinsic stacking fault area and thus requires additional energy.

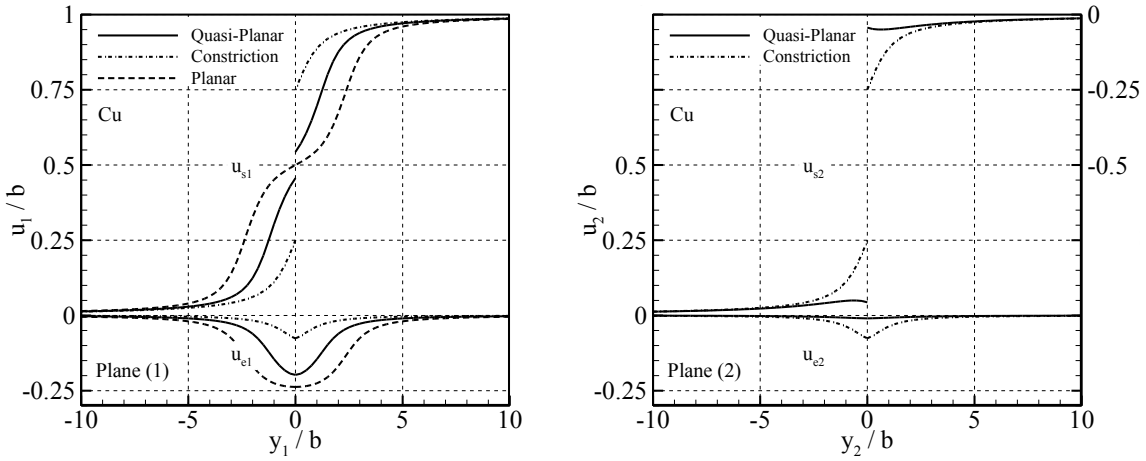

Figure 4-9. In Cu, due to the lower intrinsic stacking fault energy and larger stacking fault zone, the core of a screw dislocation prefers to be quasi-planar and stays in the primary slip plane. The figure shows both screw and edge components on the primary slip plane (left) and the cross-slip plane (right), as compared with planar and constricted core structures

Table 4-3. Total energy comparison of the possible core structure in Cu

(μb^2)	E_{Elastic}	$E_{\text{Interatomic}}$	E_{Total}	ΔE_{Total}
Planar core	–0.044942	0.061065	0.016123	0
Quasi-planar core	–0.051431	0.060890	0.009459	–0.0067
Constriction	–0.049983	0.060886	0.010903	–0.0052

4.3.2.1 *Critical glide shear stress*

Because of the quasi-planar core structure, the screw dislocation is more glissile in Cu. The critical glide shear stress in Cu is much lower than in Al. For the case of $k_s > 1$, the critical glide shear stress (τ_s^{Crit}) is plotted as a function of k_s in Fig. 4-10. The values of τ_s^{Criti} ranging from $3.16\times10^{-3}\mu$ to $3.19\times10^{-3}\mu$ are not as sensitive to k_s as Al. Although τ_s^{Criti} is in the same order to $2.7\times10^{-3}\mu$ from atomistic simulation (Duesbery, 1998) and $1.2\times10^{-3}\mu$ from internal friction experiments (Bujard, *et al*., 1987), it is still three orders larger than the value of $5\times10^{-6}\mu$ measured in plastic deformation (Basinski, 1959). The larger value in our simulation may result from introducing the over-estimated spread-out screw components on the cross-slip plane. For the case that the critical shear stress is more dominant on the cross slip plane (2), the transition of the gliding process on the

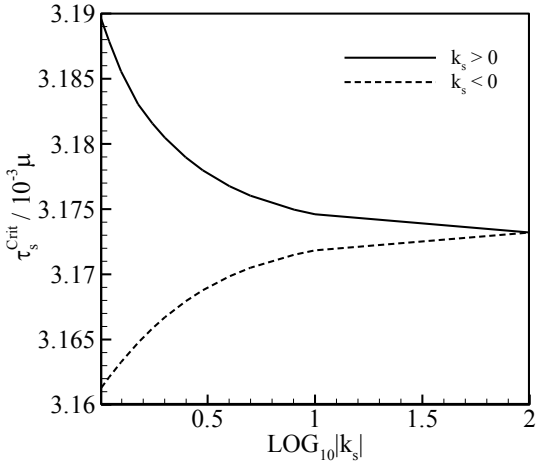

Figure 4-10. The critical glide shear stress (τ_s^{Crit}) as a function of the ratio of the resolved glide shear stress on each slip plane (k_s).

primary slip plane to the cross slip plane involves the Fleischer cross-slip mechanism (Fleischer, 1959). The simulation requires the incorporation of normal opening displacement so to incorporate the "stair rod" dislocation. We leave the Fleischer cross-slip mechanism for the future study after the opening displacements can be implemented by developing tension coupled γ-surface.

4.3.2.2 *Effects of the Escaig stresses* (τ_e) *on cross-slip*

We shall first focus on the case that the Escaig stress only exists on the primary slip plane. As the positive Escaig stress increasing from 0, it compresses the partial dislocations while reducing both the edge and screw components on the primary slip plane (1). This constriction process simultaneously stretches the core structure of the dislocation on the cross slip plane as both the associated edge and screw components increase. The process is stable until the resolved Escaig stress (τ_{e1}) reaches a critical value τ_e^{Crit} when the configuration becomes unstable. Further quasi-static constriction process would require a decreasing τ_{e1}, and eventually forming the constricted core when Escaig stress returns to 0. The cross-slip ends when the constricted core is spontaneously transferred to the quasi-planar core on the cross-slip plane by the repulsion force between the edge-components. The whole cross-slip process is depicted in Fig. 4-11(c). The energy variation during the cross slip is illustrated in Fig. 4-11(a). The balanced Escaig stress versus the partial dislocation separation is plotted in Fig. 4-11(b). It is also evident from the energy landscape that Escaig stress the constricted core structure is an unstable equilibrium configuration.

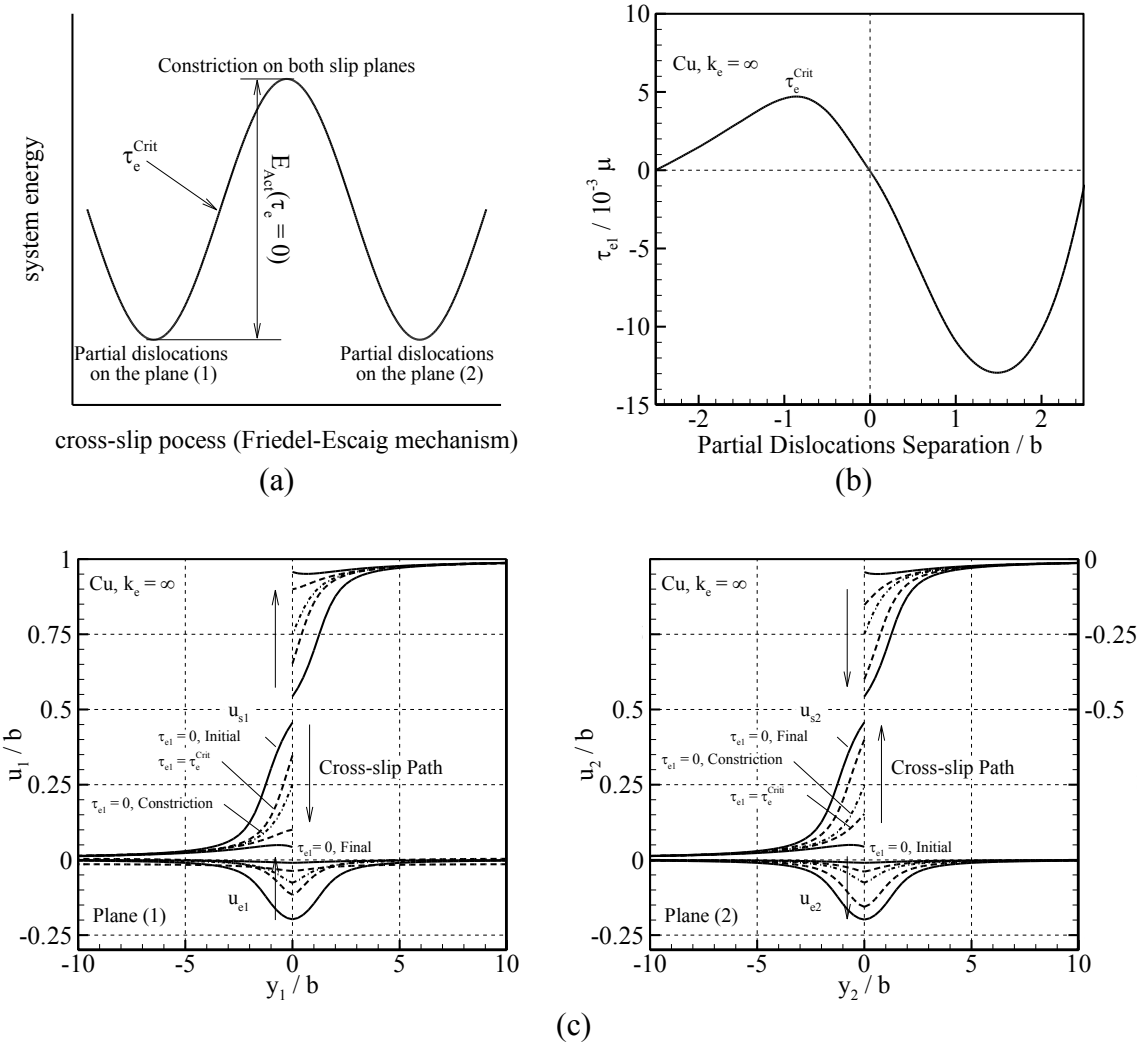

Figure 4-11. In Cu cross-slip occurs when compressive Escaig stress is applied on the primary slip plane. (a) Schematic energy variation during the cross-slip. (b) The resolved Escaig-stress vuses the partial dislocation separation. (c) The sequences of relative displacements during the cross-slip on the primary slip plane (left) and the cross-slip plane (right).

For the more general case with Escaig stress acting on both primary and cross-slip plane, the occurrence of cross-slip is determined by the ratio of the Escaig stresses (k_e). For the case of both compressing Escaig stresses with the larger one on the primary slip plane, τ_{e1} dominates the slip system and the cross-slip occurs if $\tau_{e1} > \tau_e^{Crit}$, following the process described above. For the case of both compressive Escaig stresses with the larger one on the cross-slip plane, although τ_{e1} can achieve positive value to shrink the intrinsic stacking fault zone on the primary plane (1), the same positive but larger τ_{e2} prevents the separation of the partial dislocation on the cross-slip plane (2). Thus it is seldom for cross-slip to occur under this condition even a quite large external loading is applied. For the case of the opposite resolved Escaig stresses, no matter which one is larger, the negative τ_{e2}, which helps the formation of the embryonic partial dislocations on the cross-slip plane (2), always accompanies with the positive τ_{e1}, the cross-slip occurs if $\tau_{e1} > \tau_e^{Crit}$. The critical Escaig stress as a function of k_e is plotted in Fig. 4-12. For all the cases in which cross-slip can occur, the maximum activation energy at zero stress is always the energy variation between the quasi-planar core and constricted core, i.e. $0.015\mu b^2$ or 0.064eV/b.

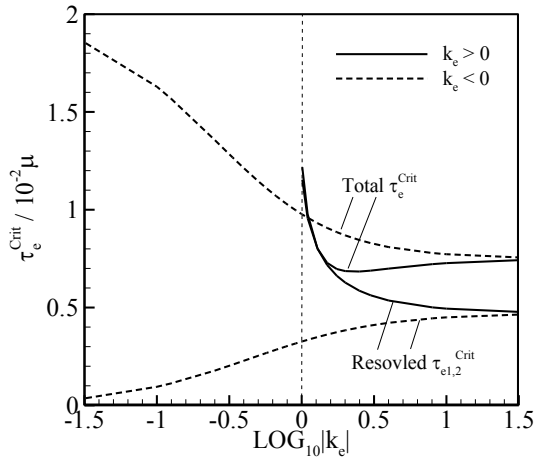

Figure 4-12. The critical Escaige stress as a function of k_e. For the case of $0 < k_e < 1$, cross-slip does not occur.

4.4 Analysis of 3D Cross-slip Process in Cu

The above analysis of the cross slip of idealistic straight dislocations under the plane strain condition provides good insights in the energetic of cross-slip process. The more realistic Friedel-Escaig cross-slip involves the curved partial dislocations on both primary and cross-slip plane as a consequence of a localized constriction and outward protrusion of slip into an unstable saddle-point configuration as the resolved Escaig stress reaches the critical value. To incorporate the three dimensional configuration, the periodic boundary condition is implemented along the intersection line direction. The period of the domain is selected to be 50*b*. As a demonstration for the cross-slip following the Friedel-Escaig mechanism, only Cu is used for calculation. The loading condition is selected so that only Escaig stresses are applied with the ratio $k_e = -1$, under which the opposite Escaig stress on the cross-slip plane favors for the occurrence of cross-slip, and

the dislocation configurations on the primary plane at τ_e is the same as on the cross-slip at $-\tau_e$ due to the symmetric slip system. In the calculation, a tiny perturbation at the intersection is introduced to naturally activate the saddle-point configuration of the curved partial dislocations. The sequences of the displacement continuities on the slip plane (1) and (2) are plotted in Fig. 4-13. The contour plots represent two slip components of the partials. Fig. 4-13(a) shows the configuration of the initial dissociated dislocation on the primary slip plane. Under increasing compressing Escaig stress, the partial dislocations are constricted straightly. When τ_e reaches the critical value, the dislocations protrude partially into the cross-slip plane without fully constricted as a straight line. The joints of the four partial dislocations have the same configuration as an equilibrium constricted core (dash-dot line in Fig. 4-9). Fig. 4-13(b) shows the protrusion of the partial dislocations onto the cross-slip plane and the formation of the constriction joints. An unstable equilibrium can be formed when τ_e returns to zero (Fig. 13c). Two types of constriction joints have also been found in the intermediate of the cross-slip as in the atomistic simulation (Rao, *et al*. 1999; Wen, *et al*., 2004): edge-like (Joint B) and screw-like (Joint A) constrictions. Fig. 4-13(d) shows the expansion of the partial dislocations on the plane (2) with the motion of the constriction joints to the periodic boundary. Fig. 4-13(e) shows the final configuration of dissociated dislocation on the cross-slip plane.

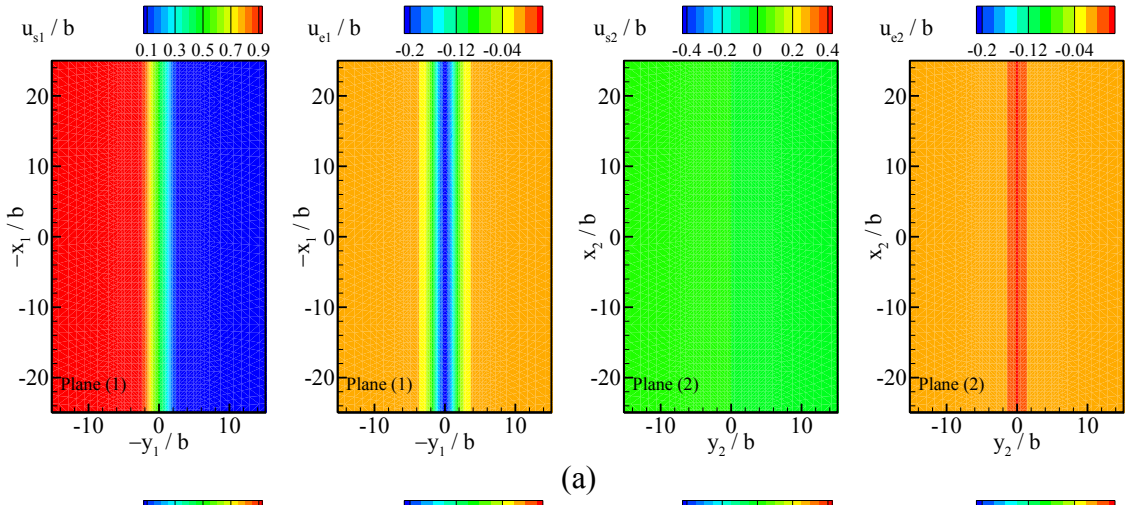
u_{s1} / b
0.1 0.3 0.5 0.7 0.9
u_{e1} / b
-0.2 -0.12 -0.04
u_{s2} / b
-0.4 -0.2 0 0.2 0.4
u_{e2} / b
-0.2 -0.12 -0.04
$-x_1$ / b
$-y_1$ / b
x_2 / b
y_2 / b
Plane (1)
Plane (2)

(a)

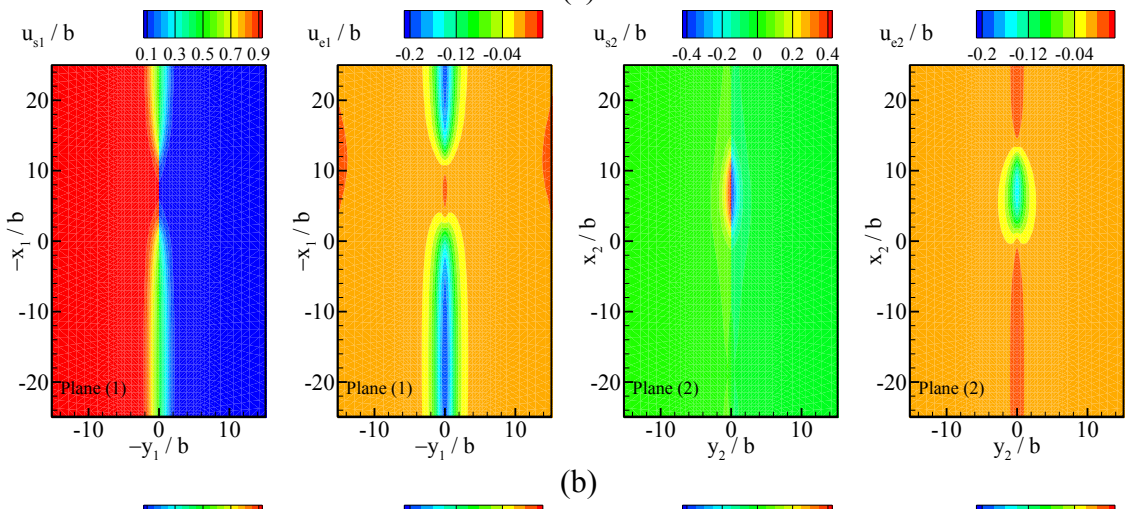
u_{s1} / b
0.1 0.3 0.5 0.7 0.9
u_{e1} / b
-0.2 -0.12 -0.04
u_{s2} / b
-0.4 -0.2 0 0.2 0.4
u_{e2} / b
-0.2 -0.12 -0.04
$-x_1$ / b
$-y_1$ / b
x_2 / b
y_2 / b
Plane (1)
Plane (2)

(b)

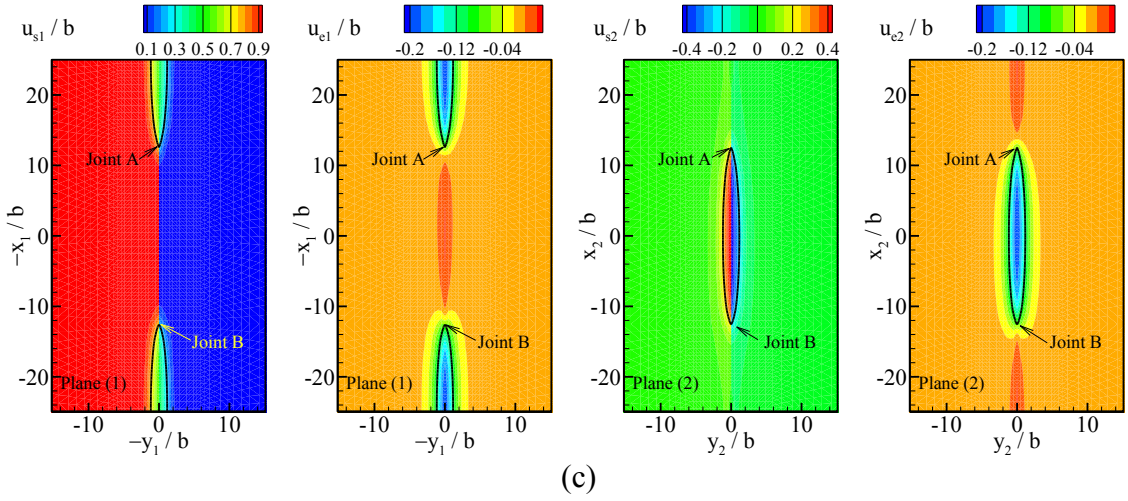
u_{s1} / b
0.1 0.3 0.5 0.7 0.9
u_{e1} / b
-0.2 -0.12 -0.04
u_{s2} / b
-0.4 -0.2 0 0.2 0.4
u_{e2} / b
-0.2 -0.12 -0.04
Joint A
Joint B
$-x_1$ / b
$-y_1$ / b
x_2 / b
y_2 / b
Plane (1)
Plane (2)

(c)

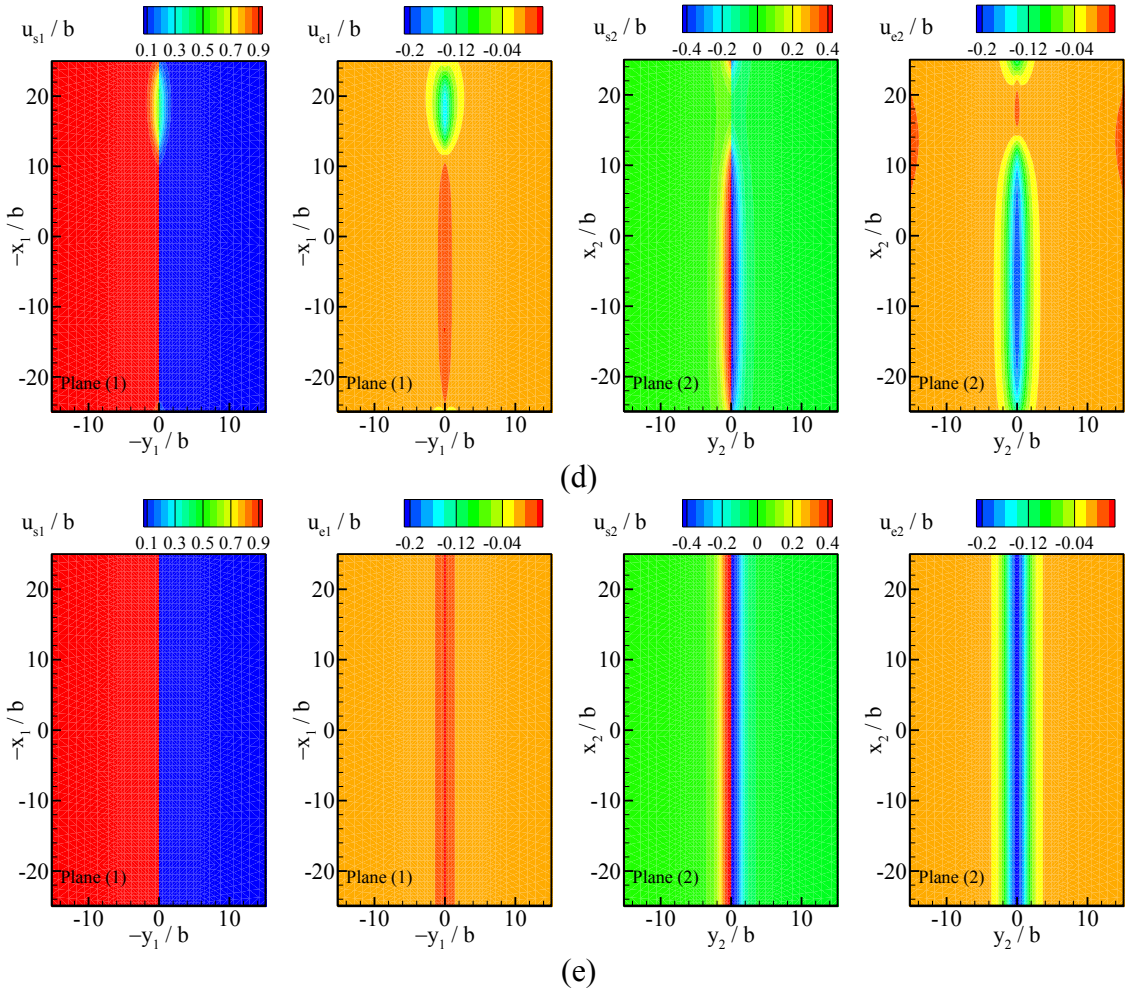

Figure 4-13. The sequences of the displacement continuities on the intersecting two slip planes during dislocation cross-slip in Cu. (a) The configuration of the initial dissociated dislocation on the primary slip plane. (b) The protrusion of the partial dislocations onto the cross-slip plane and the formation of the constriction joints. (c) An unstable equilibrium can be formed when τ_e returns to zero. (d) The expansion of the partial dislocations on the plane (2) with the motion of the constriction joints to the periodic boundary. (e) The final configuration of dissociated dislocation on the cross-slip plane.

Fig. 4-14 plots the dependence of the activation energy on loading for cross-slip of the screw dislocation involved with curved partial dislocations. The maximum activation energy at $\tau_e = 0$ is determined as 1.45eV for Cu compared with the 2.7eV reported in atomistic simulation (Rasmussen, *et al*., 1997) and 1.15eV estimated by the experiments (Bonneville, Escaig, Martin, 1989). The activation energy is in the same order of magnitude in creep experiments (1.4eV) (Bonneville, Escaig, Martin, 1989), indicating that cross-slip could be a rate controlling process. Note that the maximum activation energy in the simulation would be influenced by the period length (L_y) of the domain. However, considering the activation energy is mainly determined by energy of the constrictions and the constriction profiles eventually kept invariant as the increased constrictions separation, so the activation energy converges quickly as the domain period (L_y) increases.

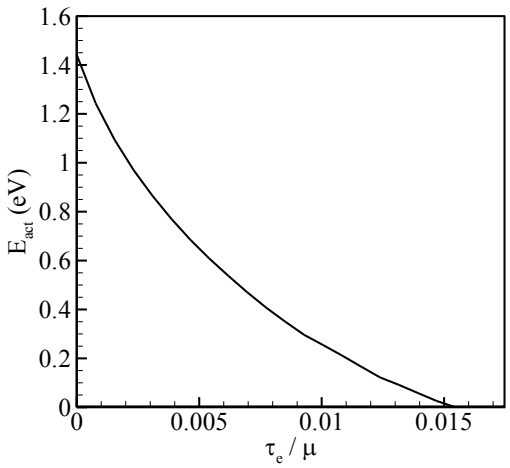

Figure 4-14. Activation energy of cross-slip of a dissociated dislocation.

4.5 Summary and Discussion

We have analyzed the Friedel-Escaig cross-slip mechanisms in FCC metals using a multiscale model that incorporates atomic information into continuum-mechanics approach. The intersecting slip planes are modeled as surfaces of displacement discontinuities embedded in the linear elastic medium. The atomic potential between the adjacent atomic layers along the slip plane is assumed to be the generalized stacking fault energy, which is obtained based on atomic calculations. The relative displacements along the slip plane, corresponding to the configurations of partial dislocations and stacking faults, are solved through the variational boundary integral method.

The cross-slip behaviors in Al and Cu are comparatively studied for their distinctive difference in the stacking fault energy. For metals with narrow intrinsic stacking fault due to the relatively high γ_{sf} such as Al, the dislocation core tends to spontaneously spread-out on both primary and cross-slip planes. The spread-out core becomes an obstacle for dislocation gliding. Relatively large shear stress is required to drive the dislocation to glide during the cross-slip. Without Escaig stress, the preference of the gliding plane depends on the competition between the two resolved shear stresses on the slip planes. The energy barrier between the spreaded-out and planar core configurations appears to be in the range that the cross slip may occur under thermal motion with the aid of the preferable shear stress on the cross slip plane. On the other hand, Escaig stress plays almost an equally important role in cross-slip. It can either compress or stretch the stacking fault, which directly facilities or impedes the occurrence of the cross slip. It is

generally difficulty to characterize the critical conditions for cross-slip under general loading condition, for the reason that the cross slip not only depends only on the stress state but also on the energy associated with the configuration under the stress state. For metals with large intrinsic stacking fault due to the relatively low γ_{sf} such as Cu, the dislocation core prefers to be planar on the primary slip plane and thus it has much lower Peierls stress for dislocation to glide. Thus during the cross-slip, Escaig shear stresses need to be mainly applied to constrict the dissociated dislocation and force it protrude to the cross-slip plane. The preferred loading condition is that there is lager compressing Escaig shear stress on the primary slip plane accompanied with stretching Escaig shear stress on the cross slip plane. Although the mechanism of cross-slip is slightly different from Al, the calculated activation energy is also at about 2eV, the same range of Cu. This indicates that the cross-slip could be thermal activated as a common phenomenon in FCC metals.

The unstable equilibrium core structure and the critical Escaig stress in Cu are similar features to the atomistic simulation study of cross-slip of iridium (Cawkwell, *et al*., 2007). The rate of cross-slip is high in both metals. However, it is more brittle for iridium than Cu. The phenomenon may result from that cross-slip can play different roles at the different stages of the plasticity deformation. Cross-slip at the early stage as a hardening mechanism may lead to intense forest hardening and increase in dislocation density so that brittle cleavage is a natural consequence (Puschl 2002; Cawkwell, *et al*., 2007). At the contrary, cross-slip at the later stage as a softening mechanism may help dislocations escape from their locked positions and annihilate with others, reducing

dislocation density and relaxing internal stress (Puschl 2002). For Ir, the critical Escaig stress for cross-slip, calculated by atomistic simulation as $0.025C_{44}$, can be achieved at the stage II of the plasticity deformation when dislocations begin to pile up at obstacles (Cawkwell, *et al*., 2007). For Cu, because the maximum resolved shear stress was approximately 24MPa or $4.6\times10^{-4}\mu$ up to the end of stage II at 473K (Bonneville, Escaig, Martin, 1988) and it is 2 orders lower than the calculated critical Escaig stress, the cross-slip can only occur at Stage III of the plasticity deformation.

References

Argon A. S., 1987. Brittle to ductile transition in cleavage fracture, *Acta Metallugica*, 35(1), 185-196.

Asaro, R. J., Suresh, S., 2005. Mechanistic models for the activation volume and rate sensitivity in metals with nanocrystalline grains and nano-scale twins. *Acta Materialia*, 53(12), 3369-3382.

Barnett D.M, Asaro R.J., 1972. Fracture mechanics of slit-like cracks in anisotropic elastic media. *Journal of the Mechanics and Physics of Solids*, 20(6), 356-366.

Basinski, Z. S., 1959. Thermally activated glide in face-centred cubic metals and its application to the theory of strain hardening. *Philosophical Magazine*, 4(40), 393-432.

Berner. R., 1960. Die temperaturabhangigkelt und geschwindigkeitsabhangigkeit der verfestigung kubis ch-flachenzentrierter metalleinkristalle. *Z Naturf (A)*,15, 689.

Brochard, S., Beauchamp, P., Grilhe, J., 2000. Dislocation nucleation from surface steps: atomistic simulation in aluminium. *Philosophical Magazine A*, 80(503).

Bonneville, J., Escaig, B., Martin, J.L., 1988. A study of cross-slip activation parameters in pure copper. *Acta Metall.*, 36 (8), 1989-2002.

Buehler, M., Hartmaier, A., Gao, H., 2003. Atomistic and continuum studies of crack-like diffusion wedges and associated dislocation mechanisms in thin films on substrates. *Journal of the Mechanics and Physics of Solids*, 51 (2003) 2105-2125.

Bujard, M., Benoit, W., Gremaud, G., 1987. Study of the dislocation mechanism responsible for the bordoni relaxation in aluminum by the 2-wave acoustic coupling method. *Journal of applied physics*, 62(8), 3173-3183.

Burgers, J. M., 1939. Some considerations on the fields of stress connected with dislocations in a regular crystal lattice. *Proc. Kon. Ned. Akad. Wetencschap.*, 42, 293-378.

Cawkwell, M. J., Woodward, C., Nguyen-Manh, D., Pettifor, D.G., Vitek V., 2007. Atomistic study of athermal cross-slip and its impact on the mechanical properties of iridium. *Acta Materialia*, 161–169.

Chantasiriwan, S., Milstein, F., 1998. Embedded-atom models of 12 cubic metals incorporating second- and third-order elastic-moduli data. *Physical Review B*, 58, 5996.

Dash, W. C., 1957. *Dislocation and Mechanichal Properties of Crystals*. (Fisher, J., Ed.) New York: Wiley.

Daw, M. S., Baskes, M.I., 1983. Semiempirical, quantum-mechanical calculation of hydrogen embrittlement in metals. *Phys Rev Lett*, 50, 1285.

Daw, M. S., Baskes, M.I., 1984. Embedded-atom method - derivation and application to impurities, surfaces, and other defects in metals. *Phys Rev Lett*, 28, 6443.

Duesbery, M.S., 1998. Dislocation motion, constriction and cross-slip in fcc metals. *Modelling Simul. Mater. Sci. Eng.*, 6, 35–49.

Escaig, B., 1968. Sur le glissement dévié des dislocations dans la structure cubique à faces centrées. *J Physique*, 29, 225.

Feltner, C. E., Laird. C., 1967. Cyclic stress-strain response of fcc metals and alloys. *Acta Metall*, 15, 1621.

Finnis M. W., Sinclair, J. E., 1984. A simple empirical N-body potential for transition metals. *Philosophical Magazine A*, 50(1), 45-55.

Fleischer, R. L., 1959. Cross slip of extended dislocations. *Acta Metall.*, 7, 134.

Foiles, S. M., Baskes, M. I., Daw, M. S., 1986. Embedded-atom-method functions for the fcc metals Cu, Ag, Au, Ni, Pd, Pt, and their alloys. *Physical Review B*, 33, 7983.

Frank, F. C., 1949. *Physica*, 15, 131.

Friedel, J., 1959. *Internal stresses and fatigue in metals*. (Rassweiler, G.M., Grube, W.L., Ed.) Amsterdam: Elsevier, p. 220.

Gao, H., Zhang, L., Nix, W., Thompson, C., Arzt, E., 1999. Crack-like grain boundary diffusion wedges in thin metal films. *Acta Materialia*, 47, 2865–2878.

Greer, J. R., Oliver, W. C. and Nix, W. D., 2005. Size dependence in mechanical properties of gold at the micron scale in the absence of strain gradients. *Acta Materialia*, 53, 1821-1830.

Godet, J., Pizzagalli, L., Brochard, S., 2004. Theoretical study of dislocation nucleation from simple surface defects in semiconductors. *Physical Review B*, 70, 054109.

Haasen, P., 1967. *Lattice defects and their interactions*. (Hasiguti, Ed.) New York, p. 437.

Hartmaier, A., Gumbsch, P., 2005. Thermal activation of crack-tip plasticity: The brittle or ductile response of a stationary crack loaded to failure. *Physical Review B* 71 (2). 024108.

Hartmaier, A., Gumbsch, P., 2002. Scaling relations for crack-tip plasticity. *Philosophical Magazine A*, 82 (17-18), 3187-3200.

Hirth, J. P., Lothe, J., 1982. *Theory of Dislocations, 2nd ed.* New York.: John Wiley.

Kumar, K. S., Van Swygenhoven, H., Suresh, S., 2003. Mechanical behavior of nanocrystalline metals and alloys. *Acta Materialia*, 51 (19), 5743-5774.

Kysar, J. W., 2003. Energy dissipation mechanisms in ductile fracture. *Journal of the Mechanics and Physics of Solids*, 51, 795 – 824

Lothe J. (1982). Dislocations in anisotropic media: The interaction energy. *Philosophical Magazine A*, 46(1), 177-180.

Li, C., Xu, G., 2006. Critical conditions for dislocation nucleation at surface steps. *Philosophical Magazine A*, 86 (20), 2957-2970.

Li, J., Wang, C. Z., Chang, J. P., Cai, W., Bulatov, V. V., Ho, K. M., Yip, S., 2004. Core energy and Peierls stress of a screw dislocation in bcc molybdenum: a periodic-cell tight-binding study. *Physical Review B*, 70 (10), 104113.

Liu, G., Xu G., 2009. Nucleation of partial dislocations at a crack and its implication on deformation mechanisms of nanostructured metals. *Journal of the Mechanics and Physics of Solids*, 1078–1092.

Lu, G., Bulatovb, V. V., Kioussisc, N., 2002. Dislocation constriction and cross-slip: An ab initio study. *Physical Review B*, 66, 144103.

Lu, G., Bulatovb, V. V., Kioussisc, N., 2004. On stress assisted dislocation constriction and cross-slip. *International Journal of Plasticity*, 20, 447-458.

Mishin, Y., Farkas, D., Mehl, M. J., Papaconstantopoulos, D. A., 1999. Interatomic potentials for monoatomic metals from experimental data and ab initio calculations. *Physical Review B*, 59 (5), 3393-3407.

Mishin, Y., Mehl, M. J., Papaconstantopoulos, D. A., Voter, A. F., Kress, J. D., 2001. Structural stability and lattice defects in copper: Ab initio, tight-binding, and embedded-atom calculations. *Physical Rreview B*, 63(22), 224106.

Nabarro, F. R. N., 1947. Dislocations in a simple cubic lattice. *Proceedings of the Physical Society of London*, 59 (332), 256-272.

Orowan, E., 1934. Mechanical strength properties and real structure of crystals. *Z. Phys.* 89, 634.

Peierls, R., 1940. The size of a dislocation. *Proceedings of the Physical Society*, 52, 34-37.

Polany, M., 1934. *Z. Phys.*, 89, 660.

Puschl, W., 2002. Models for dislocation cross-slip in close-packed crystal structures: a critical review. *Progress in Materials Science*, 415-461.

Rasmussen, T., Jacobsen, K.W., Leffers, T., Pedersen, O.B., 1997. Simulations of the atomic structure, energetics, and cross slip of screw dislocations in copper. *Physical Review B*, 56 (6), 2977.

Rao, S., Parthasarathy, T.A., 1999. Atomistic simulation of cross-slip processes in model fcc. *Philosophical Magazine A*, 79 (5), 1167-1192.

Rice, J. R., 1992. Dislocation nucleation from a crack tip - an analysis based on the peierls concept. *Journal of the Mechanics and Physics of Solids*, 40 (2), 239-271.

Rice, J. R., Beltz, G.E., 1994. The activation-energy for dislocation nucleation at a crack. *Journal of the Mechanics and Physics of Solids*, 42(2), 333-360.

Rice J. R., Thomson R., 1974. Ductile versus brittle behavior of crystals. *Philosophical Magazine*, 29(1), 73-97.

Rose, J. H., Smith, J. R., Guinea, F., Ferrante, J., 1984. Universal features of the equation of state of metals. *Phys Rev B*, 29, 2963.

Segall D. E., Li, C., Xu, G., 2006. Corroboration of a multiscale approach with all atom calculations in analysis of dislocation nucleation from surface steps. *Philosophical Magazine A*, 86(32), 5083-5101.

Schoeck, G., Puschl, W., 1991. The formation of dislocation loops at crack tips in 3 dimensions. *Philosophical Magazine A*, 64 (4), 931-949.

Schoeck, G., 2001. The core structure, recombination energy and Peierls energy for dislocations in Al. *Philosophical Magazine A*, 81(5), 1161-1176.

Schoeck, G., 2003. The emission of dislocations from crack tips - A critical assessment. *Materials Science and Engineering A*, 356, 93-101.

Schoeck, G., 2005. The Peierls model: Progress and limitations. *Materials Science and Engineering A*, 400-401, 7-17.

Taylor, G. F., 1934. *Proc. R. Soc*. A 145, 362.

Vitek, V., 1968. Intrinsic stacking faults in body-centred cubic crystals. *Philosophical Magazine*, 18 (154), 773 - 786.

Xu, G., Argon, A. S., 2000. Homogeneous nucleation of dislocation loops under stress in perfect crystals. *Philosophical Magazine Letters*, 80 (9), 605-611.

Xu, G., Argon, A. S., Oritz, M., 1997. Critical configurations for dislocation nucleation from crack tips. *Philosophical Magazine A*, 75 (2), 341-367.

Xu, G., Argon, A. S., Ortiz, M., 1995. Nucleation of dislocations from crack tips under mixed-modes of loading - implications for brittle against ductile behavior of crystals. *Philosophical Magazine A*, 72 (2), 415-451.

Xu, G., Ortiz, M., 1993. A variation boundary integral method for the analysis of 3-d cracks of arbitrary geometry modeled as continuous distributions of dislocation loops. *International Journal for Numerical Methods in Engineering*, 36 (21), 3675-3701.

Xu, G., Zhang, C., 2003. Analysis of dislocation nucleation from a crystal surface based on the Peierls-Nabarro dislocation model. *Journal of the Mechanics and Physics of Solids*, 51 (8), 1371-1394.

Uchic, M. D., Dimiduk, D. M., Florando, J. N., Nix, W. D., 2004. Sample Dimensions Influence Strength and Crystal Plasticity. *Science*, 305, 986-989.

Wen, M., Fukuyama, S., Yokogawa, K., 2004. Hydrogen-affected cross-slip process in fcc nickel. *Physical Review B*, 174108.

Yamakov, V., Wolf, D., Phillpot, S. R., Mukherjee, A. K., Gleiter, H., 2003. Deformation mechanism crossover and mechanical behaviour in nanocrystalline materials. *Philosophical Magazine Letters*, 83 (6), 385-393.

Zhu, T., Li, J., Yip, S., 2004. Atomistic study of dislocation loop emission from a crack tip. *Physical Review Letters*, 93 (2), 025503.

Appendix: Tables of Fourier coefficients of γ-surfaces

The Fourier expansion of the generalized stacking fault energy (γ-surface) can be written as

$$\gamma(\bar{u}_x, \bar{u}_y) = \sum_{m,n=0}^{+\infty} \begin{bmatrix} \cos 2m\pi\bar{u}_x \left(a_{mn} \cos 2n\pi\bar{u}_y + b_{mn} \sin 2n\pi\bar{u}_y\right) + \\ \sin 2m\pi\bar{u}_x \left(c_{mn} \cos 2n\pi\bar{u}_y + d_{mn} \sin 2n\pi\bar{u}_y\right) \end{bmatrix}.$$

The γ-surfaces for several metals have been calculated by atomistic simulation based on embedded atom method. The Fourier coefficients of γ-surface for these metals are listed in below tables.

Table A-1. Fourier coefficients of the {111} slip plane γ-surface for Al.

Al	Slip Plane: {111}		Minshion's potential (1999)	
(J/m^2)	a_{mn}	b_{mn}	c_{mn}	d_{mn}
m = 0, n = 0	3.2747E-001	0.0000E+000	0.0000E+000	0.0000E+000
m = 0, n = 1	0.0000E+000	0.0000E+000	0.0000E+000	0.0000E+000
m = 0, n = 2	-1.0021E-001	1.1688E-001	0.0000E+000	0.0000E+000
m = 0, n = 3	0.0000E+000	0.0000E+000	0.0000E+000	0.0000E+000
m = 0, n = 4	1.9781E-003	1.0308E-002	0.0000E+000	0.0000E+000
m = 0, n = 5	0.0000E+000	0.0000E+000	0.0000E+000	0.0000E+000
m = 1, n = 0	0.0000E+000	0.0000E+000	0.0000E+000	0.0000E+000
m = 1, n = 1	-2.0043E-001	-2.3375E-001	0.0000E+000	0.0000E+000
m = 1, n = 2	0.0000E+000	0.0000E+000	0.0000E+000	0.0000E+000
m = 1, n = 3	-2.1902E-002	0.0000E+000	0.0000E+000	0.0000E+000
m = 1, n = 4	0.0000E+000	0.0000E+000	0.0000E+000	0.0000E+000
m = 1, n = 5	8.9746E-004	3.1685E-004	0.0000E+000	0.0000E+000
m = 2, n = 0	-1.0951E-002	0.0000E+000	0.0000E+000	0.0000E+000
m = 2, n = 1	0.0000E+000	0.0000E+000	0.0000E+000	0.0000E+000
m = 2, n = 2	3.9562E-003	-2.0617E-002	0.0000E+000	0.0000E+000
m = 2, n = 3	0.0000E+000	0.0000E+000	0.0000E+000	0.0000E+000
m = 2, n = 4	8.9746E-004	-3.1686E-004	0.0000E+000	0.0000E+000
m = 2, n = 5	0.0000E+000	0.0000E+000	0.0000E+000	0.0000E+000
m = 3, n = 0	0.0000E+000	0.0000E+000	0.0000E+000	0.0000E+000
m = 3, n = 1	8.9746E-004	-3.1686E-004	0.0000E+000	0.0000E+000
m = 3, n = 2	0.0000E+000	0.0000E+000	0.0000E+000	0.0000E+000
m = 3, n = 3	-2.2031E-003	5.0470E-005	0.0000E+000	0.0000E+000
m = 3, n = 4	0.0000E+000	0.0000E+000	0.0000E+000	0.0000E+000
m = 3, n = 5	2.7860E-004	1.3392E-004	0.0000E+000	0.0000E+000
m = 4, n = 0	-5.5327E-004	0.0000E+000	0.0000E+000	0.0000E+000
m = 4, n = 1	0.0000E+000	0.0000E+000	0.0000E+000	0.0000E+000
m = 4, n = 2	2.7859E-004	1.3392E-004	0.0000E+000	0.0000E+000
m = 4, n = 3	0.0000E+000	0.0000E+000	0.0000E+000	0.0000E+000
m = 4, n = 4	1.6427E-004	-7.4270E-004	0.0000E+000	0.0000E+000
m = 4, n = 5	0.0000E+000	0.0000E+000	0.0000E+000	0.0000E+000
m = 5, n = 0	0.0000E+000	0.0000E+000	0.0000E+000	0.0000E+000
m = 5, n = 1	5.9628E-004	3.7857E-004	0.0000E+000	0.0000E+000
m = 5, n = 2	0.0000E+000	0.0000E+000	0.0000E+000	0.0000E+000
m = 5, n = 3	3.3920E-005	1.2713E-004	0.0000E+000	0.0000E+000
m = 5, n = 4	0.0000E+000	0.0000E+000	0.0000E+000	0.0000E+000
m = 5, n = 5	3.4860E-005	1.3249E-004	0.0000E+000	0.0000E+000

Table A-2. Fourier coefficients of the {111} slip plane γ-surface for Ni.

Ni	Slip Plane: {111}		Minshion's potential (1999)	
(J/m^2)	a_{mn}	b_{mn}	c_{mn}	d_{mn}
m = 0, n = 0	6.9512E-001	0.0000E+000	0.0000E+000	0.0000E+000
m = 0, n = 1	0.0000E+000	0.0000E+000	0.0000E+000	0.0000E+000
m = 0, n = 2	-1.8090E-001	2.7493E-001	0.0000E+000	0.0000E+000
m = 0, n = 3	0.0000E+000	0.0000E+000	0.0000E+000	0.0000E+000
m = 0, n = 4	3.2989E-003	1.7786E-002	0.0000E+000	0.0000E+000
m = 0, n = 5	0.0000E+000	0.0000E+000	0.0000E+000	0.0000E+000
m = 1, n = 0	0.0000E+000	0.0000E+000	0.0000E+000	0.0000E+000
m = 1, n = 1	-3.6179E-001	-5.4986E-001	0.0000E+000	0.0000E+000
m = 1, n = 2	0.0000E+000	0.0000E+000	0.0000E+000	0.0000E+000
m = 1, n = 3	-1.0606E-001	0.0000E+000	0.0000E+000	0.0000E+000
m = 1, n = 4	0.0000E+000	0.0000E+000	0.0000E+000	0.0000E+000
m = 1, n = 5	-3.6285E-003	4.6125E-003	0.0000E+000	0.0000E+000
m = 2, n = 0	-5.3032E-002	0.0000E+000	0.0000E+000	0.0000E+000
m = 2, n = 1	0.0000E+000	0.0000E+000	0.0000E+000	0.0000E+000
m = 2, n = 2	6.5979E-003	-3.5571E-002	0.0000E+000	0.0000E+000
m = 2, n = 3	0.0000E+000	0.0000E+000	0.0000E+000	0.0000E+000
m = 2, n = 4	-3.6285E-003	-4.6125E-003	0.0000E+000	0.0000E+000
m = 2, n = 5	0.0000E+000	0.0000E+000	0.0000E+000	0.0000E+000
m = 3, n = 0	0.0000E+000	0.0000E+000	0.0000E+000	0.0000E+000
m = 3, n = 1	-3.6285E-003	-4.6125E-003	0.0000E+000	0.0000E+000
m = 3, n = 2	0.0000E+000	0.0000E+000	0.0000E+000	0.0000E+000
m = 3, n = 3	6.2570E-004	-1.6590E-003	0.0000E+000	0.0000E+000
m = 3, n = 4	0.0000E+000	0.0000E+000	0.0000E+000	0.0000E+000
m = 3, n = 5	2.5413E-003	-1.2798E-003	0.0000E+000	0.0000E+000
m = 4, n = 0	1.3184E-003	0.0000E+000	0.0000E+000	0.0000E+000
m = 4, n = 1	0.0000E+000	0.0000E+000	0.0000E+000	0.0000E+000
m = 4, n = 2	2.5413E-003	-1.2798E-003	0.0000E+000	0.0000E+000
m = 4, n = 3	0.0000E+000	0.0000E+000	0.0000E+000	0.0000E+000
m = 4, n = 4	-8.1772E-004	-3.0160E-003	0.0000E+000	0.0000E+000
m = 4, n = 5	0.0000E+000	0.0000E+000	0.0000E+000	0.0000E+000
m = 5, n = 0	0.0000E+000	0.0000E+000	0.0000E+000	0.0000E+000
m = 5, n = 1	-1.9386E-003	-2.5507E-003	0.0000E+000	0.0000E+000
m = 5, n = 2	0.0000E+000	0.0000E+000	0.0000E+000	0.0000E+000
m = 5, n = 3	3.0392E-004	-1.3800E-004	0.0000E+000	0.0000E+000
m = 5, n = 4	0.0000E+000	0.0000E+000	0.0000E+000	0.0000E+000
m = 5, n = 5	6.7493E-004	-1.0205E-003	0.0000E+000	0.0000E+000

Table A-3. Fourier coefficients of the {111} slip plane γ-surface for Cu.

Cu	Slip Plane: {111}		Minshion's potential (2001)	
(J/m^2)	a_{mn}	b_{mn}	c_{mn}	d_{mn}
m = 0, n = 0	3.5809E-001	0.0000E+000	0.0000E+000	0.0000E+000
m = 0, n = 1	0.0000E+000	0.0000E+000	0.0000E+000	0.0000E+000
m = 0, n = 2	-9.7408E-002	1.5232E-001	0.0000E+000	0.0000E+000
m = 0, n = 3	0.0000E+000	0.0000E+000	0.0000E+000	0.0000E+000
m = 0, n = 4	4.4898E-003	9.7672E-003	0.0000E+000	0.0000E+000
m = 0, n = 5	0.0000E+000	0.0000E+000	0.0000E+000	0.0000E+000
m = 1, n = 0	0.0000E+000	0.0000E+000	0.0000E+000	0.0000E+000
m = 1, n = 1	-1.9482E-001	-3.0463E-001	0.0000E+000	0.0000E+000
m = 1, n = 2	0.0000E+000	0.0000E+000	0.0000E+000	0.0000E+000
m = 1, n = 3	-4.8430E-002	0.0000E+000	0.0000E+000	0.0000E+000
m = 1, n = 4	0.0000E+000	0.0000E+000	0.0000E+000	0.0000E+000
m = 1, n = 5	-3.0702E-003	5.6678E-003	0.0000E+000	0.0000E+000
m = 2, n = 0	-2.4215E-002	0.0000E+000	0.0000E+000	0.0000E+000
m = 2, n = 1	0.0000E+000	0.0000E+000	0.0000E+000	0.0000E+000
m = 2, n = 2	8.9795E-003	-1.9534E-002	0.0000E+000	0.0000E+000
m = 2, n = 3	0.0000E+000	0.0000E+000	0.0000E+000	0.0000E+000
m = 2, n = 4	-3.0702E-003	-5.6678E-003	0.0000E+000	0.0000E+000
m = 2, n = 5	0.0000E+000	0.0000E+000	0.0000E+000	0.0000E+000
m = 3, n = 0	0.0000E+000	0.0000E+000	0.0000E+000	0.0000E+000
m = 3, n = 1	-3.0702E-003	-5.6678E-003	0.0000E+000	0.0000E+000
m = 3, n = 2	0.0000E+000	0.0000E+000	0.0000E+000	0.0000E+000
m = 3, n = 3	1.3573E-003	5.1707E-004	0.0000E+000	0.0000E+000
m = 3, n = 4	0.0000E+000	0.0000E+000	0.0000E+000	0.0000E+000
m = 3, n = 5	3.7411E-004	-1.3598E-004	0.0000E+000	0.0000E+000
m = 4, n = 0	-2.2766E-004	0.0000E+000	0.0000E+000	0.0000E+000
m = 4, n = 1	0.0000E+000	0.0000E+000	0.0000E+000	0.0000E+000
m = 4, n = 2	3.7411E-004	-1.3598E-004	0.0000E+000	0.0000E+000
m = 4, n = 3	0.0000E+000	0.0000E+000	0.0000E+000	0.0000E+000
m = 4, n = 4	-1.2366E-004	-4.9043E-004	0.0000E+000	0.0000E+000
m = 4, n = 5	0.0000E+000	0.0000E+000	0.0000E+000	0.0000E+000
m = 5, n = 0	0.0000E+000	0.0000E+000	0.0000E+000	0.0000E+000
m = 5, n = 1	3.0280E-005	-1.9430E-004	0.0000E+000	0.0000E+000
m = 5, n = 2	0.0000E+000	0.0000E+000	0.0000E+000	0.0000E+000
m = 5, n = 3	7.3620E-005	7.3800E-005	0.0000E+000	0.0000E+000
m = 5, n = 4	0.0000E+000	0.0000E+000	0.0000E+000	0.0000E+000
m = 5, n = 5	-3.7800E-005	1.2863E-004	0.0000E+000	0.0000E+000

Table A-4. Fourier coefficients of the {110} slip plane γ-surface for Fe.

Fe	Slip Plane: {110}		Chantasiriwan's potential (1998)	
(J/m^2)	a_{mn}	b_{mn}	c_{mn}	d_{mn}
m = 0, n = 0	1.1368E+000	0.0000E+000	0.0000E+000	0.0000E+000
m = 0, n = 1	0.0000E+000	0.0000E+000	0.0000E+000	0.0000E+000
m = 0, n = 2	0.0000E+000	0.0000E+000	0.0000E+000	0.0000E+000
m = 0, n = 3	-6.1309E-001	0.0000E+000	0.0000E+000	0.0000E+000
m = 0, n = 4	0.0000E+000	0.0000E+000	0.0000E+000	0.0000E+000
m = 0, n = 5	0.0000E+000	0.0000E+000	0.0000E+000	0.0000E+000
m = 1, n = 0	0.0000E+000	0.0000E+000	0.0000E+000	0.0000E+000
m = 1, n = 1	-6.1309E-001	0.0000E+000	0.0000E+000	6.1309E-001
m = 1, n = 2	1.9028E-001	0.0000E+000	0.0000E+000	1.9028E-001
m = 1, n = 3	0.0000E+000	0.0000E+000	0.0000E+000	0.0000E+000
m = 1, n = 4	-5.6625E-002	0.0000E+000	0.0000E+000	5.6625E-002
m = 1, n = 5	-4.5047E-002	0.0000E+000	0.0000E+000	-4.5047E-002
m = 2, n = 0	0.0000E+000	0.0000E+000	0.0000E+000	0.0000E+000
m = 2, n = 1	-4.5047E-002	0.0000E+000	0.0000E+000	-4.5047E-002
m = 2, n = 2	1.6443E-002	0.0000E+000	0.0000E+000	-1.6443E-002
m = 2, n = 3	0.0000E+000	0.0000E+000	0.0000E+000	0.0000E+000
m = 2, n = 4	-1.8669E-002	0.0000E+000	0.0000E+000	-1.8669E-002
m = 2, n = 5	1.1277E-002	0.0000E+000	0.0000E+000	-1.1276E-002
m = 3, n = 0	8.2322E-003	0.0000E+000	0.0000E+000	0.0000E+000
m = 3, n = 1	0.0000E+000	0.0000E+000	0.0000E+000	0.0000E+000
m = 3, n = 2	0.0000E+000	0.0000E+000	0.0000E+000	0.0000E+000
m = 3, n = 3	-2.0598E-004	0.0000E+000	0.0000E+000	-1.4763E-003
m = 3, n = 4	0.0000E+000	0.0000E+000	0.0000E+000	0.0000E+000
m = 3, n = 5	0.0000E+000	0.0000E+000	0.0000E+000	0.0000E+000
m = 4, n = 0	0.0000E+000	0.0000E+000	0.0000E+000	0.0000E+000
m = 4, n = 1	-1.3635E-003	0.0000E+000	0.0000E+000	1.3640E-003
m = 4, n = 2	1.1908E-003	0.0000E+000	0.0000E+000	1.1907E-003
m = 4, n = 3	0.0000E+000	0.0000E+000	0.0000E+000	0.0000E+000
m = 4, n = 4	-7.7470E-004	0.0000E+000	0.0000E+000	7.7418E-004
m = 4, n = 5	1.1850E-003	0.0000E+000	0.0000E+000	1.1852E-003
m = 5, n = 0	0.0000E+000	0.0000E+000	0.0000E+000	0.0000E+000
m = 5, n = 1	4.4060E-005	0.0000E+000	0.0000E+000	4.2880E-005
m = 5, n = 2	4.9760E-005	0.0000E+000	0.0000E+000	-5.0090E-005
m = 5, n = 3	0.0000E+000	0.0000E+000	0.0000E+000	0.0000E+000
m = 5, n = 4	-4.7466E-004	0.0000E+000	0.0000E+000	-4.7406E-004
m = 5, n = 5	-1.0325E-004	0.0000E+000	0.0000E+000	1.0268E-004

Table A-5. Fourier coefficients of the {112} slip plane γ-surface for Fe.

Fe	Slip Plane: {112}		Chantasiriwan's potential (1998)	
(J/m^2)	a_{mn}	b_{mn}	c_{mn}	d_{mn}
m = 0, n = 0	2.3451E+000	0.0000E+000	0.0000E+000	0.0000E+000
m = 0, n = 1	-1.4806E+000	0.0000E+000	0.0000E+000	0.0000E+000
m = 0, n = 2	-3.6122E-001	0.0000E+000	0.0000E+000	0.0000E+000
m = 0, n = 3	-7.2823E-002	0.0000E+000	0.0000E+000	0.0000E+000
m = 0, n = 4	-6.1414E-003	0.0000E+000	0.0000E+000	0.0000E+000
m = 0, n = 5	6.6990E-005	0.0000E+000	0.0000E+000	0.0000E+000
m = 1, n = 0	-2.7857E-001	0.0000E+000	3.2260E-001	0.0000E+000
m = 1, n = 1	-1.1595E-001	0.0000E+000	-1.3632E-001	0.0000E+000
m = 1, n = 2	-2.4762E-002	0.0000E+000	-1.1906E-001	0.0000E+000
m = 1, n = 3	1.1994E-002	0.0000E+000	-2.2278E-002	0.0000E+000
m = 1, n = 4	2.9049E-003	0.0000E+000	-1.2938E-002	0.0000E+000
m = 1, n = 5	3.4651E-003	0.0000E+000	-5.6858E-003	0.0000E+000
m = 2, n = 0	5.3525E-003	0.0000E+000	2.9282E-002	0.0000E+000
m = 2, n = 1	-2.3104E-002	0.0000E+000	-7.9734E-003	0.0000E+000
m = 2, n = 2	-2.4613E-003	0.0000E+000	-1.8195E-002	0.0000E+000
m = 2, n = 3	2.6067E-003	0.0000E+000	-1.3406E-002	0.0000E+000
m = 2, n = 4	2.2542E-003	0.0000E+000	-3.0939E-003	0.0000E+000
m = 2, n = 5	5.2386E-004	0.0000E+000	3.7982E-003	0.0000E+000
m = 3, n = 0	5.4869E-003	0.0000E+000	1.6417E-003	0.0000E+000
m = 3, n = 1	-6.4357E-003	0.0000E+000	1.7773E-003	0.0000E+000
m = 3, n = 2	-7.6737E-003	0.0000E+000	-3.7138E-003	0.0000E+000
m = 3, n = 3	-5.0569E-003	0.0000E+000	-1.2933E-003	0.0000E+000
m = 3, n = 4	-2.8787E-004	0.0000E+000	1.5823E-003	0.0000E+000
m = 3, n = 5	5.4222E-004	0.0000E+000	3.9132E-004	0.0000E+000
m = 4, n = 0	2.5693E-003	0.0000E+000	-3.2845E-003	0.0000E+000
m = 4, n = 1	-9.0204E-004	0.0000E+000	2.4539E-003	0.0000E+000
m = 4, n = 2	-2.8664E-003	0.0000E+000	1.8658E-003	0.0000E+000
m = 4, n = 3	-8.1174E-004	0.0000E+000	6.8693E-004	0.0000E+000
m = 4, n = 4	6.1213E-004	0.0000E+000	-8.0827E-004	0.0000E+000
m = 4, n = 5	-1.7943E-004	0.0000E+000	-8.0842E-004	0.0000E+000
m = 5, n = 0	-8.6184E-004	0.0000E+000	-1.9673E-003	0.0000E+000
m = 5, n = 1	7.0724E-004	0.0000E+000	8.9862E-004	0.0000E+000
m = 5, n = 2	-6.7880E-005	0.0000E+000	1.3691E-003	0.0000E+000
m = 5, n = 3	-2.2550E-005	0.0000E+000	2.2512E-004	0.0000E+000
m = 5, n = 4	-2.0678E-004	0.0000E+000	-3.7068E-004	0.0000E+000
m = 5, n = 5	-7.0380E-005	0.0000E+000	3.3180E-005	0.0000E+000

Table A-6. Fourier coefficients of the {110} slip plane γ-surface for Ta.

Ta	Slip Plane: {110}		Finnis-Sinclair potential (1984)	
(J/m^2)	a_{mn}	b_{mn}	c_{mn}	d_{mn}
m = 0, n = 0	1.2444E+000	0.0000E+000	0.0000E+000	0.0000E+000
m = 0, n = 1	-2.5230E-005	-1.4580E-005	0.0000E+000	0.0000E+000
m = 0, n = 2	1.3880E-005	-1.0320E-005	0.0000E+000	0.0000E+000
m = 0, n = 3	-6.6165E-001	-1.6910E-005	0.0000E+000	0.0000E+000
m = 0, n = 4	3.7140E-005	-9.1300E-006	0.0000E+000	0.0000E+000
m = 0, n = 5	-1.5200E-005	1.2850E-005	0.0000E+000	0.0000E+000
m = 1, n = 0	-8.7400E-006	0.0000E+000	0.0000E+000	0.0000E+000
m = 1, n = 1	-6.6169E-001	-2.9710E-005	0.0000E+000	6.6164E-001
m = 1, n = 2	2.1866E-001	-1.9670E-005	0.0000E+000	2.1864E-001
m = 1, n = 3	-3.0040E-005	-3.1110E-005	0.0000E+000	0.0000E+000
m = 1, n = 4	-4.6152E-002	-1.8560E-005	0.0000E+000	4.6224E-002
m = 1, n = 5	-4.5416E-002	2.6550E-005	0.0000E+000	-4.5388E-002
m = 2, n = 0	-7.5100E-006	0.0000E+000	0.0000E+000	0.0000E+000
m = 2, n = 1	-4.5439E-002	-2.8740E-005	0.0000E+000	-4.5386E-002
m = 2, n = 2	-1.3437E-002	-2.0250E-005	0.0000E+000	1.3466E-002
m = 2, n = 3	-3.1690E-005	-3.1470E-005	0.0000E+000	0.0000E+000
m = 2, n = 4	-2.1688E-002	-1.8560E-005	0.0000E+000	-2.1765E-002
m = 2, n = 5	1.2754E-002	2.6220E-005	0.0000E+000	-1.2785E-002
m = 3, n = 0	1.2574E-002	0.0000E+000	0.0000E+000	0.0000E+000
m = 3, n = 1	-4.7310E-005	-2.8760E-005	0.0000E+000	0.0000E+000
m = 3, n = 2	2.4120E-005	-2.0490E-005	0.0000E+000	0.0000E+000
m = 3, n = 3	-1.6502E-003	-3.0970E-005	0.0000E+000	8.6584E-003
m = 3, n = 4	7.3760E-005	-1.8590E-005	0.0000E+000	0.0000E+000
m = 3, n = 5	-3.0080E-005	2.5800E-005	0.0000E+000	0.0000E+000
m = 4, n = 0	-6.8500E-006	0.0000E+000	0.0000E+000	0.0000E+000
m = 4, n = 1	-1.9250E-003	-2.8240E-005	0.0000E+000	1.8746E-003
m = 4, n = 2	1.5513E-003	-2.1890E-005	0.0000E+000	1.5228E-003
m = 4, n = 3	-3.4190E-005	-3.0820E-005	0.0000E+000	0.0000E+000
m = 4, n = 4	-3.2443E-003	-1.8440E-005	0.0000E+000	3.3196E-003
m = 4, n = 5	2.9838E-004	2.5690E-005	0.0000E+000	3.3146E-004
m = 5, n = 0	-6.7700E-006	0.0000E+000	0.0000E+000	0.0000E+000
m = 5, n = 1	-7.0871E-004	-2.7860E-005	0.0000E+000	-6.6557E-004
m = 5, n = 2	6.2264E-004	-2.2180E-005	0.0000E+000	-6.0093E-004
m = 5, n = 3	-3.2770E-005	-3.1160E-005	0.0000E+000	0.0000E+000
m = 5, n = 4	-3.7606E-004	-1.8620E-005	0.0000E+000	-4.4668E-004
m = 5, n = 5	-1.3816E-003	2.5480E-005	0.0000E+000	1.3509E-003

Table A-7. Fourier coefficients of the {112} slip plane γ-surface for Ta.

Ta	Slip Plane: {112}		Finnis-Sinclair potential (1984)	
(J/m^2)	a_{mn}	b_{mn}	c_{mn}	d_{mn}
m = 0, n = 0	3.1148E+000	0.0000E+000	0.0000E+000	0.0000E+000
m = 0, n = 1	-1.7588E+000	1.7011E-004	0.0000E+000	0.0000E+000
m = 0, n = 2	-5.4157E-001	-3.7849E-004	0.0000E+000	0.0000E+000
m = 0, n = 3	-1.4161E-001	3.3403E-004	0.0000E+000	0.0000E+000
m = 0, n = 4	-2.5653E-002	-3.8990E-004	0.0000E+000	0.0000E+000
m = 0, n = 5	4.4111E-003	4.2709E-004	0.0000E+000	0.0000E+000
m = 1, n = 0	-3.6802E-001	0.0000E+000	4.7185E-001	0.0000E+000
m = 1, n = 1	-1.7577E-001	2.9566E-004	-1.1650E-001	1.3635E-004
m = 1, n = 2	-7.7777E-002	-5.9017E-004	-2.0678E-001	-2.5782E-004
m = 1, n = 3	-1.0227E-002	4.8167E-004	-6.4423E-002	3.6501E-004
m = 1, n = 4	2.2125E-002	-5.4806E-004	1.2060E-003	-4.2229E-004
m = 1, n = 5	1.2530E-002	6.0749E-004	-2.1925E-002	4.4234E-004
m = 2, n = 0	-8.9013E-003	0.0000E+000	2.1242E-002	0.0000E+000
m = 2, n = 1	-3.5200E-002	1.6737E-004	8.2406E-003	1.5027E-004
m = 2, n = 2	-2.5571E-002	-3.6557E-004	-1.4651E-002	-2.9031E-004
m = 2, n = 3	4.7687E-003	1.5700E-004	-4.5162E-004	3.7993E-004
m = 2, n = 4	-9.0031E-003	-1.6484E-004	-7.1311E-003	-4.5647E-004
m = 2, n = 5	-6.8672E-003	2.1296E-004	-1.6977E-002	4.7401E-004
m = 3, n = 0	2.0430E-002	0.0000E+000	5.2873E-003	0.0000E+000
m = 3, n = 1	5.4748E-004	1.1760E-004	7.5363E-003	9.8420E-005
m = 3, n = 2	-6.4461E-003	-2.7321E-004	2.8497E-004	-1.8332E-004
m = 3, n = 3	1.5654E-003	2.5780E-005	-6.1093E-003	2.4887E-004
m = 3, n = 4	-2.4247E-003	-2.9180E-005	-4.2392E-003	-2.7770E-004
m = 3, n = 5	4.0610E-004	5.9700E-005	-4.0317E-003	2.8594E-004
m = 4, n = 0	4.3154E-003	0.0000E+000	-4.2357E-003	0.0000E+000
m = 4, n = 1	1.6171E-003	1.1433E-004	-5.0280E-004	7.3970E-005
m = 4, n = 2	-3.9486E-003	-2.7060E-004	3.4992E-003	-1.2691E-004
m = 4, n = 3	-3.6397E-003	2.7640E-005	-1.5389E-003	1.7903E-004
m = 4, n = 4	-3.9928E-003	-2.5380E-005	2.1218E-003	-1.9799E-004
m = 4, n = 5	-1.4276E-003	8.0360E-005	-5.6990E-005	2.0176E-004
m = 5, n = 0	-1.1284E-003	0.0000E+000	-2.8747E-003	0.0000E+000
m = 5, n = 1	1.0432E-004	1.1044E-004	-1.0263E-003	5.8290E-005
m = 5, n = 2	1.2398E-004	-2.6142E-004	3.2263E-003	-1.1431E-004
m = 5, n = 3	-8.6474E-004	1.3580E-005	1.7013E-003	1.4725E-004
m = 5, n = 4	2.6337E-004	-1.3120E-005	2.4341E-003	-1.7835E-004
m = 5, n = 5	5.1515E-004	6.4650E-005	2.3826E-004	1.7526E-004

Table A-8. Fourier coefficients of the {110} slip plane γ-surface for Li.

Li	Slip Plane: {110}		Chantasiriwan's potential (1998)	
(J/m^2)	a_{mn}	b_{mn}	c_{mn}	d_{mn}
m = 0, n = 0	8.9360E-002	0.0000E+000	0.0000E+000	0.0000E+000
m = 0, n = 1	0.0000E+000	0.0000E+000	0.0000E+000	0.0000E+000
m = 0, n = 2	0.0000E+000	0.0000E+000	0.0000E+000	0.0000E+000
m = 0, n = 3	-6.4839E-004	0.0000E+000	0.0000E+000	0.0000E+000
m = 0, n = 4	0.0000E+000	0.0000E+000	0.0000E+000	0.0000E+000
m = 0, n = 5	0.0000E+000	0.0000E+000	0.0000E+000	0.0000E+000
m = 1, n = 0	0.0000E+000	0.0000E+000	0.0000E+000	0.0000E+000
m = 1, n = 1	-4.9090E-002	0.0000E+000	0.0000E+000	-4.9090E-002
m = 1, n = 2	3.4090E-003	0.0000E+000	0.0000E+000	-3.4090E-003
m = 1, n = 3	0.0000E+000	0.0000E+000	0.0000E+000	0.0000E+000
m = 1, n = 4	-3.5030E-005	0.0000E+000	0.0000E+000	-3.5030E-005
m = 1, n = 5	-1.2720E-005	0.0000E+000	0.0000E+000	1.2720E-005
m = 2, n = 0	0.0000E+000	0.0000E+000	0.0000E+000	0.0000E+000
m = 2, n = 1	1.7248E-002	0.0000E+000	0.0000E+000	-1.7248E-002
m = 2, n = 2	-2.9017E-003	0.0000E+000	0.0000E+000	-2.9017E-003
m = 2, n = 3	0.0000E+000	0.0000E+000	0.0000E+000	0.0000E+000
m = 2, n = 4	-9.3800E-006	0.0000E+000	0.0000E+000	9.3800E-006
m = 2, n = 5	8.6000E-006	0.0000E+000	0.0000E+000	8.6000E-006
m = 3, n = 0	-4.9090E-002	0.0000E+000	0.0000E+000	0.0000E+000
m = 3, n = 1	0.0000E+000	0.0000E+000	0.0000E+000	0.0000E+000
m = 3, n = 2	0.0000E+000	0.0000E+000	0.0000E+000	0.0000E+000
m = 3, n = 3	-3.6918E-004	0.0000E+000	0.0000E+000	2.0050E-004
m = 3, n = 4	0.0000E+000	0.0000E+000	0.0000E+000	0.0000E+000
m = 3, n = 5	0.0000E+000	0.0000E+000	0.0000E+000	0.0000E+000
m = 4, n = 0	0.0000E+000	0.0000E+000	0.0000E+000	0.0000E+000
m = 4, n = 1	-8.2177E-003	0.0000E+000	0.0000E+000	-8.2177E-003
m = 4, n = 2	-2.0751E-004	0.0000E+000	0.0000E+000	2.0751E-004
m = 4, n = 3	0.0000E+000	0.0000E+000	0.0000E+000	0.0000E+000
m = 4, n = 4	-2.8320E-005	0.0000E+000	0.0000E+000	-2.8320E-005
m = 4, n = 5	6.9200E-006	0.0000E+000	0.0000E+000	-6.9200E-006
m = 5, n = 0	0.0000E+000	0.0000E+000	0.0000E+000	0.0000E+000
m = 5, n = 1	3.4090E-003	0.0000E+000	0.0000E+000	-3.4090E-003
m = 5, n = 2	1.7422E-004	0.0000E+000	0.0000E+000	1.7422E-004
m = 5, n = 3	0.0000E+000	0.0000E+000	0.0000E+000	0.0000E+000
m = 5, n = 4	3.4970E-005	0.0000E+000	0.0000E+000	-3.4970E-005
m = 5, n = 5	-2.8000E-006	0.0000E+000	0.0000E+000	-2.8000E-006

Table A-9. Fourier coefficients of the {110} slip plane γ-surface for Mo.

Mo	Slip Plane: {110}		Finnis-Sinclair potential (1984)	
(J/m^2)	a_{mn}	b_{mn}	c_{mn}	d_{mn}
m = 0, n = 0	1.1474E+000	0.0000E+000	0.0000E+000	0.0000E+000
m = 0, n = 1	-6.2100E-006	3.4950E-005	0.0000E+000	0.0000E+000
m = 0, n = 2	5.4660E-005	1.4640E-005	0.0000E+000	0.0000E+000
m = 0, n = 3	-5.8816E-001	5.6560E-005	0.0000E+000	0.0000E+000
m = 0, n = 4	6.1200E-006	-1.0020E-005	0.0000E+000	0.0000E+000
m = 0, n = 5	-2.0840E-005	2.8930E-005	0.0000E+000	0.0000E+000
m = 1, n = 0	8.5640E-005	0.0000E+000	0.0000E+000	0.0000E+000
m = 1, n = 1	-5.8813E-001	6.9840E-005	0.0000E+000	5.8814E-001
m = 1, n = 2	2.0387E-001	2.9350E-005	0.0000E+000	2.0378E-001
m = 1, n = 3	-4.9380E-005	1.1350E-004	0.0000E+000	0.0000E+000
m = 1, n = 4	-3.8302E-002	-2.0160E-005	0.0000E+000	3.8300E-002
m = 1, n = 5	-3.5751E-002	5.7900E-005	0.0000E+000	-3.5719E-002
m = 2, n = 0	8.8930E-005	0.0000E+000	0.0000E+000	0.0000E+000
m = 2, n = 1	-3.5722E-002	7.0040E-005	0.0000E+000	-3.5718E-002
m = 2, n = 2	-1.3628E-002	2.9190E-005	0.0000E+000	1.3728E-002
m = 2, n = 3	-5.6000E-005	1.1350E-004	0.0000E+000	0.0000E+000
m = 2, n = 4	-2.1844E-002	-1.9960E-005	0.0000E+000	-2.1846E-002
m = 2, n = 5	1.8215E-002	5.7790E-005	0.0000E+000	-1.8248E-002
m = 3, n = 0	-1.6550E-002	0.0000E+000	0.0000E+000	0.0000E+000
m = 3, n = 1	1.5700E-006	6.9960E-005	0.0000E+000	1.8900E-006
m = 3, n = 2	9.4570E-005	2.9240E-005	0.0000E+000	0.0000E+000
m = 3, n = 3	-1.5895E-002	1.1364E-004	0.0000E+000	7.0795E-003
m = 3, n = 4	0.0000E+000	-2.0030E-005	0.0000E+000	0.0000E+000
m = 3, n = 5	-3.2550E-005	5.7830E-005	0.0000E+000	2.1500E-006
m = 4, n = 0	9.3260E-005	0.0000E+000	0.0000E+000	0.0000E+000
m = 4, n = 1	1.1694E-002	7.0090E-005	0.0000E+000	-1.1707E-002
m = 4, n = 2	-9.8645E-003	2.9140E-005	0.0000E+000	-9.9714E-003
m = 4, n = 3	-6.4910E-005	1.1355E-004	0.0000E+000	0.0000E+000
m = 4, n = 4	-5.8711E-003	-1.9920E-005	0.0000E+000	5.8819E-003
m = 4, n = 5	-1.3571E-003	5.7720E-005	0.0000E+000	-1.3154E-003
m = 5, n = 0	8.3160E-005	0.0000E+000	0.0000E+000	0.0000E+000
m = 5, n = 1	-1.2651E-002	6.9850E-005	0.0000E+000	-1.2654E-002
m = 5, n = 2	9.1089E-003	2.9350E-005	0.0000E+000	-9.0128E-003
m = 5, n = 3	-4.7060E-005	1.1357E-004	0.0000E+000	0.0000E+000
m = 5, n = 4	-6.5799E-004	-2.0100E-005	0.0000E+000	-6.5383E-004
m = 5, n = 5	6.1343E-004	5.7890E-005	0.0000E+000	-6.3728E-004

Table A-10. Fourier coefficients of the {112} slip plane γ-surface for Mo.

Mo	Slip Plane: {112}		Finnis-Sinclair potential (1984)	
(J/m^2)	a_{mn}	b_{mn}	c_{mn}	d_{mn}
m = 0, n = 0	3.0762E+000	0.0000E+000	0.0000E+000	0.0000E+000
m = 0, n = 1	-1.6698E+000	2.9160E-004	0.0000E+000	0.0000E+000
m = 0, n = 2	-5.0122E-001	-3.0436E-004	0.0000E+000	0.0000E+000
m = 0, n = 3	-1.5789E-001	4.2494E-004	0.0000E+000	0.0000E+000
m = 0, n = 4	-4.1972E-002	-3.4552E-004	0.0000E+000	0.0000E+000
m = 0, n = 5	-1.2567E-002	5.0315E-004	0.0000E+000	0.0000E+000
m = 1, n = 0	-3.3852E-001	0.0000E+000	4.9006E-001	0.0000E+000
m = 1, n = 1	-1.2739E-001	5.0947E-004	-7.4200E-002	1.4142E-004
m = 1, n = 2	-6.2326E-002	-4.5883E-004	-1.6116E-001	-2.6581E-004
m = 1, n = 3	-2.2893E-002	6.5082E-004	-8.2265E-002	3.6652E-004
m = 1, n = 4	-5.0904E-003	-4.5180E-004	-3.1466E-002	-4.2789E-004
m = 1, n = 5	-4.1333E-003	7.5531E-004	-1.3440E-002	4.4938E-004
m = 2, n = 0	3.3261E-003	0.0000E+000	3.1938E-002	0.0000E+000
m = 2, n = 1	-2.9689E-002	3.8739E-004	-1.0749E-003	1.5042E-004
m = 2, n = 2	-2.5222E-002	-2.2881E-004	-2.5571E-002	-2.8653E-004
m = 2, n = 3	-1.7306E-003	3.3315E-004	-1.7788E-002	3.8828E-004
m = 2, n = 4	2.3037E-003	-7.8250E-005	-1.4926E-002	-4.5194E-004
m = 2, n = 5	5.0125E-003	3.6038E-004	-1.1664E-002	4.6854E-004
m = 3, n = 0	1.9425E-002	0.0000E+000	4.9442E-003	0.0000E+000
m = 3, n = 1	-1.0825E-002	3.4476E-004	7.3008E-003	1.0129E-004
m = 3, n = 2	-1.3878E-002	-1.4904E-004	2.4968E-003	-1.9040E-004
m = 3, n = 3	-7.8716E-003	2.2318E-004	-2.6411E-003	2.5616E-004
m = 3, n = 4	-3.8909E-003	4.6390E-005	-7.7960E-005	-2.9079E-004
m = 3, n = 5	-4.8573E-003	2.3268E-004	3.5871E-003	2.9301E-004
m = 4, n = 0	1.3133E-002	0.0000E+000	-1.9019E-002	0.0000E+000
m = 4, n = 1	-2.5526E-003	3.4566E-004	6.3363E-003	8.7300E-005
m = 4, n = 2	-6.6483E-003	-1.5227E-004	1.1031E-002	-1.6290E-004
m = 4, n = 3	-5.9335E-003	2.3074E-004	4.6691E-003	2.1759E-004
m = 4, n = 4	-4.2734E-003	3.4800E-005	5.9935E-003	-2.4510E-004
m = 4, n = 5	-2.8312E-003	2.5084E-004	4.8247E-003	2.4126E-004
m = 5, n = 0	-5.4662E-003	0.0000E+000	-1.0305E-002	0.0000E+000
m = 5, n = 1	-3.9385E-004	3.2887E-004	-1.5655E-003	9.1940E-005
m = 5, n = 2	1.6274E-003	-1.2028E-004	5.4372E-003	-1.7093E-004
m = 5, n = 3	3.6404E-004	1.8799E-004	3.3450E-003	2.2905E-004
m = 5, n = 4	5.6000E-004	8.1400E-005	3.0670E-003	-2.5734E-004
m = 5, n = 5	5.7218E-004	2.0333E-004	1.6727E-003	2.5627E-004